TOPOLOGICAL STRUCTURAL VORTICES IN MULTIFERROIC HEXAGONAL MANGANITES

By

XUEYUN WANG

A dissertation submitted to the

Graduate School—New Brunswick

Rutgers, The State University of New Jersey

in partial fulfillment of the requirements

for the degree of

Doctor of Philosophy

Graduate Program in Physics and Astronomy

written under the direction of

Sang-Wook Cheong

and approved by

_____

_____

_____

_____

_____

New Brunswick, New Jersey

MAY, 2015

ABSTRACT OF THE DISSERTATION

TOPOLOGICAL STRUCTURAL VORTICES IN MULTIFERROIC HEXAGONAL MANGANITES

By XUEYUN WANG

Dissertation Director:

Sang-Wook Cheong

This dissertation seeks to understand ferroelectric domains, which can be viewed as networks of topological structural vortices, in a new class of materials called multiferroic hexagonal manganites $RMnO_3$ (h-$RMnO_3$) with R = rare earths, Y, In and Sc. From an experimental standpoint with solid theoretical background, we will briefly introduce improper ferroelectricity and topological defects in general in chapter 1. Then we start our discussion by reviewing the origin of the topological defect (vortex) in multiferroic material (h-$RMnO_3$) and its self-organized domain network, which will act to motivate the work. We will also discuss the origin of self electric poling effect, self-organized criticality (SOC), and a rare phenomenon - vortex core fragmentation in chapter 2. This will be followed by chapter 3 which mainly discusses the manipulation of topological vortex by applying an external shear strain. The force on vortices in h-$RMnO_3$ generated by shear strain is analogous to the Magnus force that moves superfluid vortices in the direction transverse to the superfluid current. Chapter 4 starts with a brief introduction to the Kibble-Zurek Mechanism (KZM), which is the theoretical background of the connection between cosmology and condensed

matter physics. It turns out that multiferroic h-$RMnO_3$ is an excellent test bed for KZM through the study of defect formation, emergent continuous symmetry, and Higgs condensation of the disorder field. In the remaining chapter, we extend our scope from the standard vortex to its "dual description" –partially undistorted antipolar (PUA) vortex. Then we will end this dissertation with a summary of the results and future research directions, which actually open a new path to understand the fundamental properties of this new class of materials.

Acknowledgments

First and foremost I want to thank my advisor Professor Sang-Wook Cheong. It has been a great honor to be his Ph.D. student. He has taught me, both consciously and un-consciously, how physics can be explained in preliminary mathematics, how to write a research paper from A to Z, and how to tell a joke in a research conference. I appreciate all his contributions of time, ideas, and funding support to make my Ph.D. experience productive, joyful, and stimulating. The enthusiasm and persistence he has for his research was contagious and motivational for me, even during tough and painful times in the Ph.D. pursuit. I still remember my Ph.D. life started with a conversation with him; he said to me: "there are thousands of ways of living a life, and you don't have to be a physicist if you don't like it," which actually motivated me to try to be a physicist.

I also would like to express my deepest appreciation to my committee members, Professor Valery Kiryukhin, Professor Emil Yuzbashyan, Professor Andrew Baker and Professor Andrei Sirenko, for their advice during the annual review meetings for my research. My appreciation also goes to Professor Weida Wu for sharing academic skills, scientific thinking, discipline, and suggestions for my future career.

I express my gratitude to former and current group members: Yoichi Horibe, Namjung Hur, Young Jae Choi, Hee Taek Yi, Qin Zhen, Taekjib Choi, Seung Chul Chae, Nara Lee, Andrew Hogan, Steven Roden, Daniel Kwok, Sean Fackler, Bing Li, Yoon Seok Oh, Bin Gao, Yazhong Wang, Fei-Ting Huang, Rongwei Hu, Wei Cai, Jae Wook Kim, Seong Joon Lim, Xiaochen Fang, Fei Fan, Yue Liu, Younghun Jo, David Fan, Brian Wesley Casas, Natasha Parikh, and Joe Matheussen. Each one of them has assisted in making my research possible and has made me enjoy my lab life. I would also like to thank my colleagues and friends

from neighboring labs, Nikesh Koirala, Matthew Brahlek, Sergey Artyukhin, Sebastian Reyes Lillo, Yanan Geng, Jixia Dai, Wenbo Wang, Yuanjun Zhou, Wenhu Xu, Can Xu, and Wei Dai, for the joyful moments. My special thanks go to Yuanjun Zhou and Jie Liu for renting their spare bedroom to me in the last days at Rutgers.

I would also like to thank my cyber mates: Ye $< Jungle >$ Yang, Chen $< pts >$ Zheng, Haozhe $< lys >$ Wang, and Yukun $< XiaoMing >$ Zhu, whose generosity and friendship has always been a joy to me. I cherished the game and entertainment during my hard time with the thesis.

Finally, I sincerely express my loving thanks to my family for their patience, support, love, and understanding. Without their encouragement, it would have been impossible for me to finish this work.

Dedication

Without my family, I would not have had the focus and vigor to complete this work.

This thesis is also dedicated to my grandfather, who is a real scientist and enlightened me about science when I was young

Therefore this work is entirety dedicated to them.

Table of Contents

List of Tables

List of Figures

Chapter 1

Prologue

In condensed matter physics, physicists are concerned about the collective behavior of a large number of particles that organize themselves into an ordered state. However, one step further, physicists are even more concerned about how one ordered state transforms to another state, for example, liquid freezing into solid or a paramagnet going over into a ferromagnet, which is termed phase transition. The traditional way in condensed matter physics is achieving a more ordered state from a less ordered state. This is accompanied with symmetry breaking, which leads to the birth of our Universe as well as a variety of condensed matter phenomenon.

Symmetries determine nature ubiquitously from the beauty of human faces[1], to biology, chemistry, and even art. The concept of symmetry breaking also plays an important role throughout all fields of physics: for example chiral(simply known as handedness) [2, 3] symmetry breaking in the context of strong interactions [4], explicit Charge Parity (CP) symmetry breaking in the weak interactions [5, 6], the local gauge invariance of quantum field theory [7], the breaking of gauge symmetries to explain the origin of particle mass in the standard model [8–10], and the formation of cosmic strings in the early Universe [11, 12] or electronically ordered phases in superconductors.

The most fundamental symmetry operations are spatial inversion ($r \to -r$), time reversal ($t \to -t$) and charge conjugation ($+q \to -q$) and so on. The spontaneous breaking of symmetry with various parameters such as temperature is associated with a phase transition, and such a symmetry breaking is characterized by an order parameter. In condensed matter physics, spatial inversion and time reversal are responsible for ferric order

and magnetic order, which are simply known as electricity and magnetism in our daily life, respectively. If a system exhibits both broken spatial inversion symmetry as well as broken time reversal symmetry, a variety of interesting phenomena emerge, like multiferroicity, the magnetoelectric effect, *etc.*

Meanwhile, if symmetry is broken differently in two adjacent parts of a macroscopic sample, the boundary will contain a defect: e.g. a dislocation in a crystal or a domain wall in a ferromagnet. The defects can be considered as sources of disorder. More and more defects entering the system means putting more disorder into it, which also can be considered as a phase transition into a more disordered state. Topological defects, as we will discuss below, occur often during symmetry breaking, and are responsible for numerous phenomena such as, vortices in superconductors [13], domain and domain walls in ferroelectric [14, 15] and magnetic materials [16], and skyrmions [17].

This chapter will review two different kinds of ferroelectricity: proper (or traditional) ferroelectricity vs. improper ferroelectricity in term of symmetry breaking, which leads to a simple explanation of multiferroicity. Then it will be followed by a brief introduction of topological defect and typical examples, especially the vortices in xy-model and skyrmions.

1.1 Ferroelectricity and multiferroicity

It has been more than a century since Pockels reported the anomalously large piezoelectric constants of Rochelle salt in year 1893. Around 30 years later, J. Valasek discovered the basic ferroelectric effect - ferroelectric hysteresis loop of this special acentric compound [18]. He realized that ferroelectricity showing the dielectric properties of crystal were in many respects similar in nature to the ferromagnetic properties of iron in that there was a hysteresis effect in the field-polarization curve, see Fig. 1.1, as well as a Curie temperature T_c, an extremely large dielectric and piezoelectric response in and near the ferroelectric region. The hysteresis loops were unsymmetrical as was to be expected if the crystal had a natural polarization.

The definition of ferroelectricity then is followed: a ferroelectric (analogous to ferromagnetic) crystal is defined as a crystal showing a spontaneous electric polarization and whose direction of spontaneous polarization can be reversed by an electric field. An antiferroelectric (analogous to ferrimagnetic) crystal is defined as a crystal whose structure can be considered as being composed of two sublattices polarized spontaneously in antiparallel directions. After the discovery of ferroelectricity, there has been an ever-increasing amount of research and development, ranging from the most fundamental studies of the phenomenon to a wide variety of devices and system applications [19–23]. Fig. 1.2 [24] demonstrates the development of the oxide ferroelectric materials, which indicates the number of oxide ferroelectrics discovered each year. Until now, many typical ferroelectric materials, such as $BaTiO_3$, $LiNbO_3$ and so on, are still hot topic in condensed matter physics.

The development in the application of ferroelectric materials brought big progress to our life, such as ferroelectric memories [19] and ferroelectric field-effect transistors [25–28]. Especially the application considerations for memory devices, both as switching memory elements for ferroelectric nonvolatile random access memories (FRAMs), and as passive capacitors for volatile dynamic random access memories (DRAMs), both of them will be the main commercial application in the future. Moreover, a large number of applications

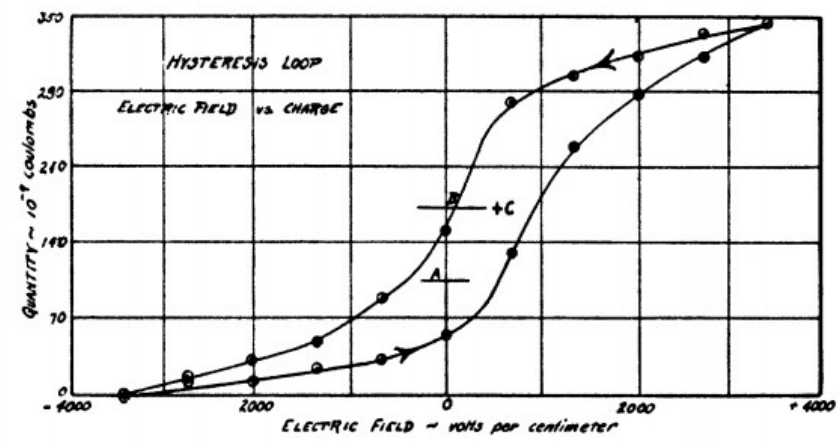

Figure 1.1: **First ferroelectric hysteresis loop of rochelle salt.** Hysteresis loops of rochelle salt at 0 °C, which is taken from reference [24]

of ferroelectric materials also develop properties that are an indirect consequence of ferroelectricity, such as dielectric, piezoelectric, pyroelectric and photovoltaic effect properties.

In ferroelectric materials, the functionalities of the material are usually determined by symmetry breaking distortions which result in order parameter fields. The regions with dissimilar order parameters are separated by domain and domain walls, which also can be viewed as defects. Theoretical predictions and experimental discoveries of novel functionalities emerging at domain walls in ferroelectrics and ferroelastic materials become more and more important, since there size and as the fact that they can be controlled [29–33]. These are associated with either intrinsic symmetry-related effects on electronic and phonon structure, or interactions between ferroic system and other materials functionalities, including coupling to other order parameters, like multiferroic properties.

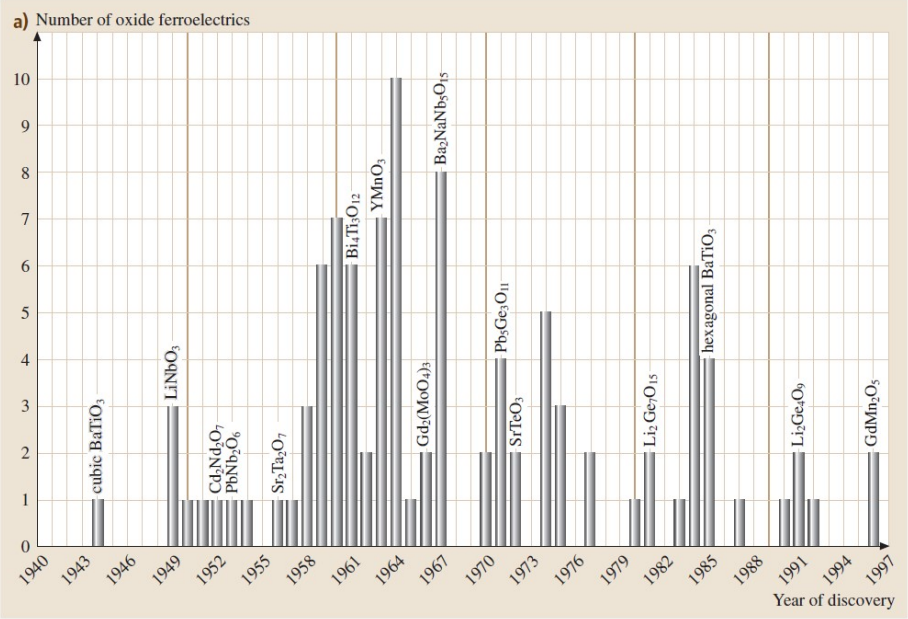

Figure 1.2: **Number of oxide ferroelectric substances discovered in each year.** Only pure compounds are taken into account in this plot, which is from reference [24]

.

1.1.1 Proper and improper ferroelectricity

Depending on the mechanism of inversion symmetry breaking, there are 2 types of ferroelectrics: proper and improper ferroelectrics.

In typical ferroelectric materials, the primary order parameter is polarization resulting from centrosymmetry breaking of chemical bond. The main driving force is the polar instability. A typical ferroelectric of this type can be understood in which, if an ion is displaced from equilibrium slightly, the force from the local electric fields due to the ions in the crystal increases faster than the elastic-restoring forces which leads to an asymmetrical shift in the equilibrium ion positions and hence to a permanent dipole moment.

A famous textbook example is barium titanate ($BaTiO_3$), the ionic displacement in $BaTiO_3$ concerns the relative position of the titanium ion within the oxygen octahedral cage in the perovskite structure, see Fig. 1.3. There are several phase transitions induced structural distortions in $BaTiO_3$, which can be briefly described from high-temperature paraelectric cubic to the ferroelectric tetragonal, orthorhombic, and then rhombohedral phase. The paraelectric cubic phase above its Curie point is about 100 °C. Below this critical temperature, the spontaneous polarization is induced along one of the [001] directions in the original cubic structure, as shown in Fig. 1.3. Note that this process has broke the symmetric state into a lower symmetry, which gives rise in the formation of different domain

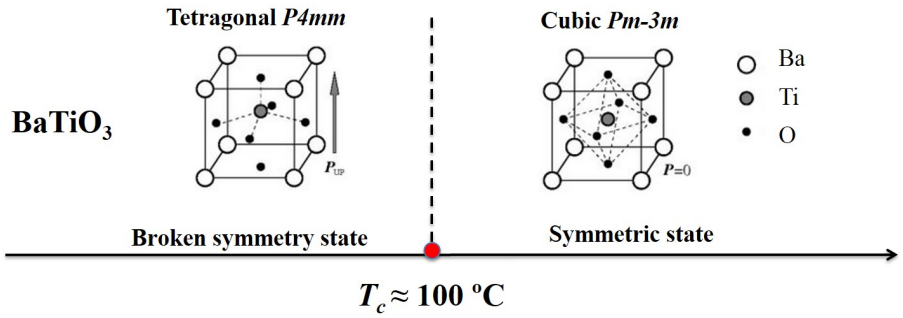

Figure 1.3: **Proper ferroelectric: paraelectric to ferroelectric phase transition in $BaTiO_3$.** The structural transition from symmetric state cubic to broken symmetry state tetragonal. The spontaneous polarization is along one of the [001] directions in the original cubic structure.

and domain walls as defects in $BaTiO_3$ [34]. These domain walls are experimentally proved as charged domain walls with steady metallic-type conductivity [35].

In contrast, the origin of so-called improper ferroelectrics [36] is: the order parameter of the phase transition is not the polarization but another physical quantity whose transformation properties are different from those of the polarization, such as magnetic orders, charge orders or structural transitions owing to zone-boundary instability. Spontaneous polarization arises in the phase transition as a secondary effect, For example, when a magnetic lattice formed through a magnetic transition does not have space-inversion symmetry, the crystallographic lattice coupled with the magnetic lattice also loses the space-inversion symmetry, often leading to ferroelectricity. This magnetism-driven ferroelectricity in, for example, $TbMnO_3$ and $TbMn_2O_5$, clearly correlates with the appearance of spiral magnetic ordering [20, 37, 38].

One hot topic is hybrid improper ferroelectricity in system $A_3B_2O_7$, which breaks the translational symmetry in ABO_3 perovskite by the interposing AO rock salt layer to form the $(AO)(ABO_3)_n$ structure, without requiring classical zone-center displacements. Note that the structure is an improper ferroelectric, since the primary order parameter is the zone boundary octahedral tilting. The prediction of the ferroelectricity was done by Nicole Benedek and Craig Fennie [39, 40], who offer a fresh approach for introducing magnetoelectrically coupled multiferroic order in layered perovskite mineral through multiple lattice distortions. They state that the magnetoelectric coupling, weak ferromagnetism, and ferroelectricity can develop from the combination of two lattice rotations, neither of which produces ferroelectric order individually. Up to date, there are four know systems, $Ca_3Ti_2O_7$ [41], which has switchable polarization, low-temperature magnetically ordered phase $Ca_3Mn_2O_7$ [42, 43], $Ca_3Ru_2O_7$ as well as $(A,B)_3Fe_2O_7$ [44].

Fig. 1.4 is from reference [39], which uses the layered perovskite $Ca_3Mn_2O_7$ as a model system to illustrate this mechanism for producing ferroelectric order coupled to magnetic properties. The crystal structure of $Ca_3Mn_2O_7$ consists of layers of corner-sharing MnO_6

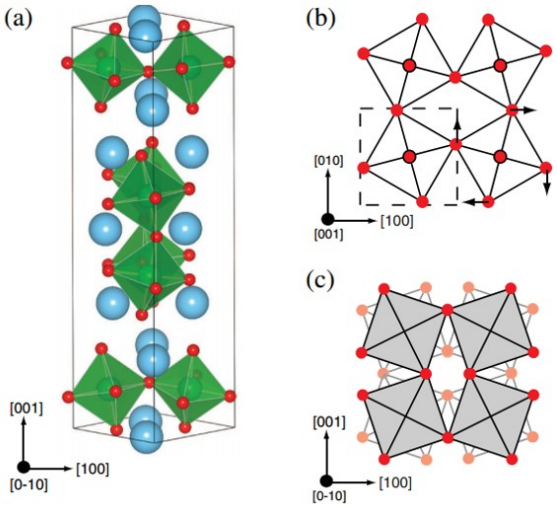

Figure 1.4: **Improper ferroelectric of $Ca_3Mn_2O_7$: structure and rotation distortions, which is taken from reference [39]** (a) shows $Ca_3Mn_2O_7$ structure in its distorted ferroelectric state. (b) and (c) show the octahedral rotation and octahedral tilt, respectively.

octahedra, with two layers of $CaMnO_3$ for every sheet of CaO as shown in Fig. 1.4(a) where Mn ions (green) are surrounded by oxygen octahedra (green with red O ions) with Ca ions (blue) interspersed. The ferroelectric state is induced through the combination of a rotation distortion in Fig. 1.4(b) and a tilt distortion shown in Fig. 1.4(c) of the oxygen octahedra. The distortions can occur at the same temperatures or different temperatures, and while neither of these distortions breaks spatial inversion independently, the combination can produce a ferroelectric polarization along [001] direction.

1.1.2 Multiferroicity

Ferroelectric and magnetic materials have influenced our life since the ancient time, which, up to our modern day, have led to some of the most important technological advances. As described by the Maxwell's equations,the changing electric field generates magnetic field, and vice versa. Magnetism and ferroelectricity are involved with local spins and off-centered structural distortions in material research, respectively. The coexistence of these 2 phenomena is termed as multiferroics, however, the coupling between them are rare as these two order parameters turned out to be mutually exclusively. It's mainly due to most

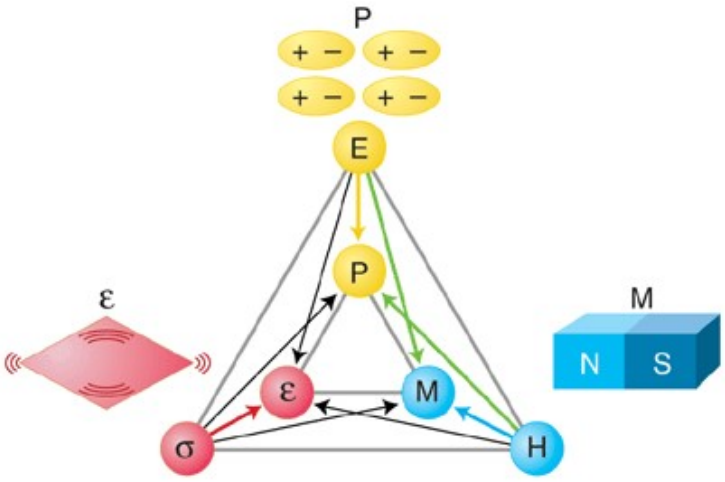

Figure 1.5: **Phase control in multiferroics, which is taken from reference [45]** The electric polarization P, magnetization M, and strain ε are controlled by their conjugate fields: electric field E, magnetic field H, and stress σ, respectively. In multiferroics, cross coupling may be presented like P (M) can be controlled by H (E).

ferroelectricity prefers empty d-orbital, while ferromagnetism requires partially-filled d shell.

The concept of multiferroicity, can be extended to multi ferroic orders, as described in Fig. 1.5, containing the couple of the electric field E, magnetic field H, and stress σ control the electric polarization P, magnetization M, and strain ε, respectively. In a ferroic material, P, M, or ε are spontaneously formed to produce ferromagnetism, ferroelectricity, or ferroelasticity, respectively. In a multiferroic, the coexistence of at least two ferroic forms of ordering leads to additional interactions. In a magnetoelectric multiferroic, a magnetic field may control P or an electric field may control M (green arrows). These couplings provide a new path for potential material design and spintronics industry in the future [45–47].

For the last twenty years, there has been a resurgence of interest in this field, which is driven by the development of advanced theoretical and experimental techniques. In those magnetism-driven ferroelectrics, magnetic order accompanied by the loss of inversion symmetry loses the lattice inversion symmetry through exchange striction, thus inducing ferroelectricity. Moreover, external magnetic field which influences the spin configurations

of magnetic order naturally results in changes in ferroelectric or dielectric properties. Highly tunable electric properties by applied magnetic fields have been observed in many materials categorized as this class. The representative examples can be listed as $RMnO_3$ (R=rare earths) [48], RMn_2O_5 [20], orthorhombic $RMnO_3$ [49], hexagonal $RFeO_3$ [50–52], langasite $Ba_3NbFe_3Si_2O_14$ [53–55], $LiCu_2O_2$ [56], Ca_3CoMnO_6 [57], delafossite $CuFeO_2$ [58], $ACrO_2$ (A=Cu, Ag), and $CaMn_7O_{12}$ [59, 60].

1.2 Topological defects

The terminology "Topological defects" was commonly used in the study of the early universe and cosmology [61], and they are inevitably created during continuous phase transition [11]. According to the "Big Bang" theory, the universe expanded and then cooled, it possibly has undergone a series of phase transitions. At lower energies it is being hidden by the process usually described as spontaneous symmetry breaking: symmetries began breaking down in regions that spread at the speed of light; topological defects occur where different regions came into contact with each other. The matter in these defects is in the original symmetric phase, which persists after a phase transition to the new asymmetric phase is completed.

Symmetry breaking is thought to be responsible for emergence of the familiar fundamental interactions from the unified field theory at GUT temperatures of $\sim 10^{15}$ GeV in the Universe cooling after Big Bang. As Kibble [11] noted, relativistic causality limits the size of domains that can coordinate the choice of broken symmetry in the nascent Universe. This results in a random selection of local broken symmetry, depending on the nature of the symmetry breakdown, various topological defects are believed to have formed in the early universe according to the Kibble-Zurek mechanism (KZM). There are a number of possible types of defects, such as domain walls, cosmic strings, monopoles, textures and other "hybrid" creatures, which influence evolution of the Universe.

Topological defects play an important role in determining properties of real materials, mainly by the symmetry properties of the matter and the nature of the phase transition. For

example, they are responsible to a large degree for the mechanical properties of metals like steel. Topological defects have different names depending on the symmetry that is broken and the particular system, in superfluid helium and XY-models, they are called vortices; in periodic crystals, they are called dislocations; and in nematic liquid crystals, they are named as disclinations.

1.2.1 Examples of topological defects

A simple example of topological defects is the dislocation in a crystal, as shown in Fig. 1.6(a), which is a 2D crystal lattice [62]. The extra row can be called dislocation in this crystal lattice. If we draw a loop surrounding the dislocation, then count the net number of rows crossed by the loop, we will find, no matter how large we draw the loop, there will always be an extra row on the right side, as displayed in Fig. 1.6(b). This approach: consider a closed loop around the defects mapped onto order parameter space, the order parameter field changes as we move around the loop. Note that topology is the study of curves and surfaces where bending and twisting is ignored. If along any loop, the order parameter winds either around the hole or through it a net number of times, then enclosed in that loop is a defect which cannot be bent or twisted flat, this can be considered as a simplified view of topological defects.

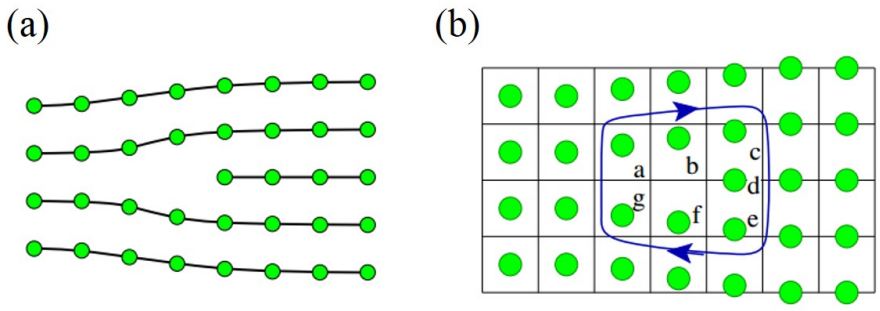

Figure 1.6: **Topological defect: dislocation in a crystal.** figures are taken from Chapter 9 of reference [61].

There are lots of other examples for topological defects [63]: [1] Monopoles are 0-dimensional (0D) (point-like) objects which form when a spherical symmetry is broken. Monopoles are predicted to be supermassive and carry magnetic charge. [2] Cosmic strings which are 1-dimensional (1D) (line-like) objects may have formed during a symmetry breaking phase transition in the early universe when the topology of the vacuum manifold associated to this symmetry breaking was not simply connected, or simply speaking, when an axial or cylindrical symmetry is broken. [3] Textures are formed when larger, more complicated symmetry groups are completely broken. Textures are delocalized topological defects which are unstable to collapse. Besides these topological defects in the study of universe, in condensed matter physics, there are a lot of examples like described below:

1.2.2 Vortices from XY-model

Spin systems on a lattice have two independent degrees of freedom, one being the dimensionality of the spin space (or the spin-degrees of freedom) and the other, the dimensionality of the underlying lattice. The former is usually denoted by n and the latter by d. In general, spin systems on a d-dimensional lattice are called n-vector models [64]. For various values of n, see table 1.1, we have different models which are widely used in not only condensed matter physics, also high energy physics.

XY-model is given to the n = 2; d = 2 model, which is a regular arrangement of a set of continuous valued (or classical) spins (spins which can be oriented along any direction on a 2-dimensional(2D) plane) on a d-dimensional lattice. Spin of each particle can be described as a vector in the 2D-plane: $\overrightarrow{\mathbf{S}} = (cos\theta, sin\theta)$. The spin can point along any direction,

n = 0	The Self-Avoiding Walks (SAW)
n = 1	The Ising model
n = 2	The XY model
n = 3	The Heisenberg model
n = 4	Toy model for the Higgs sector of the Standard Model

Table 1.1: **n-vector model for various value of n.**

corresponding to some value of θ between 0 and 2π. Notice that the Hamiltonian of this model is a function of θ only.

$$\mathcal{H} = -J \sum_{\langle j,l \rangle} \overrightarrow{\mathbf{S}}_i \cdot \overrightarrow{\mathbf{S}}_j \Rightarrow -J \sum_{\langle j,l \rangle} \cos(\theta_j - \theta_l), \tag{1.1}$$

$\mathcal{H}$ is invariant under global continuous rotations of all spins, and hence has a $U(1)$ gauge symmetry. The ordered state of this model would correspond to the case where all the spins are aligned parallel. Unlike the Ising model, the magnetization can take any value between 1 and -1, corresponding to the angular orientation of the spins. Different states of the system can have the same energy, with all of them related to each other by a global rotation of all spins and hence with different values of magnetization. Energy of spin interaction is minimal in ordered state, when all spins are aligned. On a 2D lattice aligned spins are unstable with respect to long-wave fluctuations, which means small fluctuations are accumulated on infinite lattice and destroy long order at any finite temperature. It was Berezinskii and later Kosterlitz and Thouless who suggested that the mechanism of disordering involved discontinuous deformation in spin orientations. Such a defect is called a topological defect for the case of the XY-model, which are called vortices, as shown in Fig. 1.7

In h-$RMnO_3$ which can be described by a 2D six-state clock model [65] which has similar

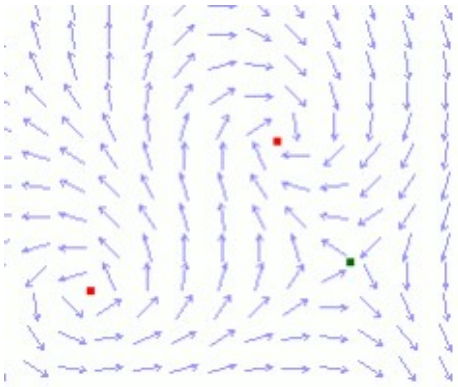

Figure 1.7: **Vortices in the XY-model.** Excitations with nontrivial topology in XY model termed as vortices and anti-vortices (marked by red and green squares). Figure is taken from http://www.ibiblio.org/e-notes/Perc/xy.htm.

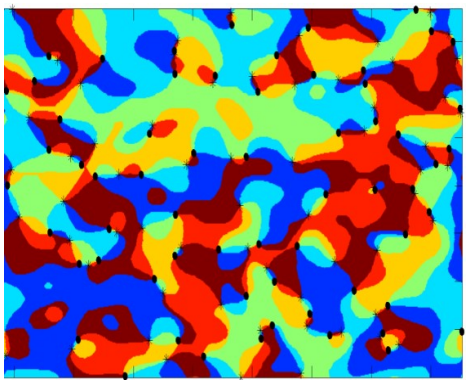

Figure 1.8: **Vortices in the 6-clock model.** The simulation is based on local update Metropolis algorithm of Monte-Carlo simulation

Hamiltonian:

$$\mathcal{H} = -J \sum_{\langle j,l \rangle} \cos\left(\theta_j - \theta_l\right) \tag{1.2}$$

however, with discrete order parameter, where $\theta_i = n_i\pi/3$ with $n_i = 1, ..., 6$. By using Monte-Carlo simulation [66], vortex in h-$RMnO_3$ can be obtained as Fig. 1.8 shows. The detail of Monte-Carlo simulation is discussed in Chapter 4.

1.2.3 Skyrmions

Water swirls and hurricanes happen in our daily life, which can be characterized by spiralling around the eye of swirl. If we consider magnetic spins formed swirls in condensed matter physics, it's termed as skyrmion. Magnetic skyrmions are particle-like nanometre-sized spin textures and its configuration cannot be deformed into the magnetic ground state, in which all spins are aligned, by a smooth or continuous process. It was firstly predicted by Skyrme [17], in which the skyrmion is studied as model for hadrons. The topologically protected particles can be stabilized in chiral magnets, in the form of stable spin textures, which has been found in several magnetic materials, such as MnSi [67], $Fe_{1-x}Co_xSi$ [68, 69] and FeGe [70], by means of neutron scattering in momentum space and Lorentz transmission electron microscopy (LTEM) techniques in real space. Interestingly, however, it has also turned out

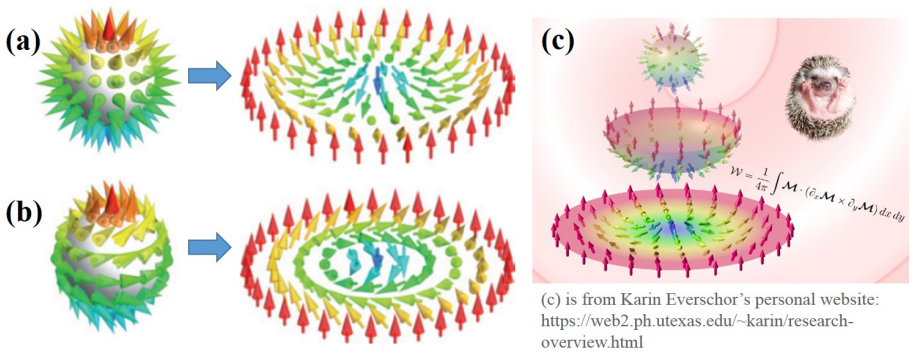

Figure 1.9: **Schematics of hedgehog skyrmion and spiral skyrmion. Figures are taken from references [74] and [75]** (a) and (b) are schematics of the spin configurations of 2 different type of skyrmions. (c) shows the topological equivalence: after performing a stereographic projection onto the plane results in a skyrmion.

to be relevant in condensed-matter systems such as the quantum Hall system [71], liquid crystals [72] and Bose condensate [73].

Simple schematics of skyrmion are drawn in 1.9, (a) and (b) [74, 75] shows the vector field of two different 2D magnetic skyrmions, (a) is a hedgehog skyrmion and (b) a spiral skyrmion. The arrows indicate the direction of the spins, and their colours represent the normal component to the plane, that is, from up direction (red) to the down direction (blue). The unfolding process from a hedgehog to a hedgehog skyrmion is displayed in (c), which is adopted form Karin Everschor's personal website. These properties can be understood from a unified viewpoint, namely the emergent electromagnetism associated with the non-coplanar spin structure of skyrmions.

From this description, potential applications of skyrmions as information carriers in magnetic information storage and processing devices are envisaged. Skyrmions have been observed mostly in metallic materials, where they are controllable by electric currents [76], and probably by temperature gradient [77, 78]. Because of their topology, they cannot be created or destroyed by smooth rearrangements of the direction of the local magnetization [79].

Chapter 2

Vortex and network of vortices in hexagonal Manganites

Hexagonal manganites $RMnO_3$ (R = Sc, Y, Ho, ... Lu) are multiferroics with coexistence of ferroelectricity ($T_c \sim 950$ -1400 °C)and antiferromagnetism ($T_N \sim 70$ -120 K). Note that we exclude $InMnO_3$, which will be discussed in Chapter 5. The ferroelectricity was firstly reported by Bertaut *et al.* in 1963 on $YMnO_3$. The origin of ferroelectricity will be discussed later. Simply speaking, the structure comprises triangular lattice layers of MnO_5 polyhedra which are tilted to form the trimerization of Mn ions in each layer. The origin of trimerization is caused by the size mismatch between R and Mn-O layers, which leads to three trimerization antiphases (α, β, γ). Due to a subsequent ionic displacement with a net electric dipole moment, each trimerization phase can supply two different ferroelectric polarizations (+, -, meaning upward or downward along the c axis). These six trimerization antiphase and ferroelectric domains cycle around a merging point with alternating ferroelectric polarization and trimerization antiphases in two different domain configurations: (α+, β-, γ+, α-, β+, γ-) or (α+, γ-, β+, α-, γ+ , β-,), which can be viewed as a vortex and an anti-vortex. vortex(antivortex) in $RMnO_3$ can be observed by using transmission electron microscopy (TEM), piezoresponse force microscopy (PFM) and optical microscopy (OM) at room temperature, as shown in. Fig. 2.1. (b) is from ref. [80]

The methods on visualization of ferroelectric domains in hexagonal manganites are list below: In Fig. 2.1(a), the bright and dark contrasts in dark field (DF)-TEM image alternating around the centre result from the unequal diffraction intensity associate with antiparallel polarization of the neighboring domains along the [001] direction due to the Friedel's pair breaking[81, 82]. Fig. 2.1(b) shows the PFM which indicates the piezo-response along

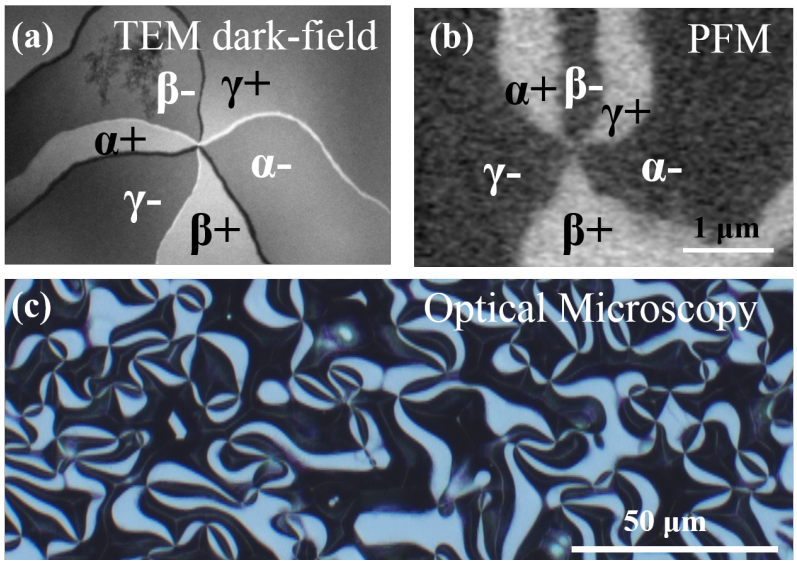

Figure 2.1: **Visualization of vortex and network of vortices.** (a)DF-TEM imaging of vortex. (b) PFM imaging of vortex, which is taken from reference [84] (c) OM imaging of vortex network after chemical etching. Corresponding trimerization and polarization phases are assigned in (a) and (b)

[001] direction when applying alternating excitation voltage[83, 84], so the bright and dark contrasts label the ferroelectric domains on *ab*-plane. OM imaging of ferroelectric is the easiest way to observe the ferroelectric domains in hexagonal manganites, the specimen has to be chemically etched in phosphoric acid for at least 20 mins at 150 °C. Chemical etching enable us to visualize the ferroelectric domain since different ferroelectric polarization has preferential etching speed, the topography are observable under OM, as shown in Fig. 2.1(c).

Below T_N, the neighboring Mn^{3+} spins arrange antiferromagnetically with a relative angle of 120° in a triangular lattice in the *ab* plane. Combining the ferroelectric and antiferromagnetic properties, hexagonal manganites provide a fruitful playground for the interplays among lattice, charges, and spins, and tremendous studies have been focused on this topic due to its profound and complex magnetic interactions. Besides the TEM, PFM, and OM visualization methods, vortices(antivortices) can be unveiled by using magnetic force microscope (MFM), conductive-atomic force microscope and magnetoelectric force microscope techniques[85], which suggest vortices(antivortices) are associated with intriguing collective

magnetism[86], electric conductance[87], at domain walls, as well as large magnetoelectric coupling of domains[88].

In this chapter, we will briefly discuss how we grow the single crystals and the origin of the ferroelectricity in $RMnO_3$. Then we will also give a detailed explanation of the most interesting phenomena: various configurations of vortices and antivortices result in a large-scale domain pattern in a way to form a self-organized network, which is displayed in Fig.2.1(c). Moreover, the network formation can be analyzed in terms of graph theory and can be properly colored, which will be discussed in section 'Type I and Type II domain networks'. In addition, we believe the organizing behavior of vortices/antivortices are reflecting the nature of self-organized criticality (SOC), which is highly under debate. In this chapter we will also explain the origin of type-I or type-II domain networks, which are induced by the oxygen-off stoichiometry in the specimens.

2.1 Sample growth

Hexagonal phases of $RMnO_3$ can be easily stabilized for R = Y, Ho, Tm, Er, Yb, and Lu. Standard flux method and floating zone method are used for high quality single crystal growth.

Polycrystalline powders of these compounds are grown by standard solid state reaction method: stoichiometric ratio of R_2O_3 powders and MnO_2 powder are grind together then pelletized for sintering. Standard sintering temperature is 1200 °C, 1300 °C for first and sencond sintering, respectively.

The growth of single crystals by flux method is following: 10 mol% $RMnO_3$ polycrystalline powders with 90 mol% Bi_2O_3 powders as flux were heated to 1250 °C and then cooled slowly to 950 °C in a platinum crucible. Tilting of crucible at 800 °C is recommended in order to extract single crystals from flux matrix easily, as seen in Fig.2.2(a). Plates-like crystals can be found with a centimeter size in the *ab* plane and hundreds microns thickness along the *c* axis, as shown in Fig.2.2(b). Advantage of flux method is that the sample came

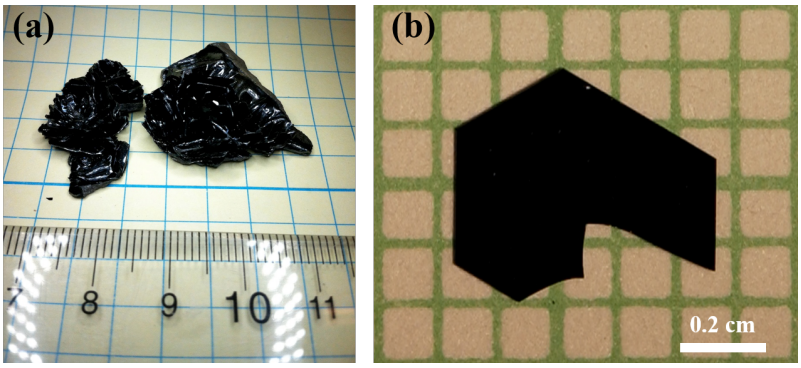

Figure 2.2: **Hexagonal manganites crystal growth.** (a)shows the image of original $ErMnO_3$ crystal chunk which was taken under LED light. (b) show one crystal with centimeter size and nice hexagonal edges (courtesy of Prof. Sang-Wook Cheong).

out with atomically clean and flat surface which is best candidate for any surface scanning experiment. Floating zone growth method can be found in the references [89], and pressured floating zone growth is reported to give better sample quality [90].

One special group is $InMnO_3$ and its relative compounds like B-site Ga-doped $InMnO_3$, in which the smaller A site ionic radius of indium results in more structural distortion. It turns out that standard solid state reaction method does not work for $InMnO_3$ system. A special sample growth method was used for it, named grain growth, which will be discuss in Chapter 5.

2.1.1 Stripes and vortices

Two distinct domain patterns of as-grown $RMnO_3$ crystals has been found: stripe vs. vortex patterns, which are directly related with the single crystal growth temperature.

To be more specific, as grown $YMnO_3$ shows vortex-antivortex domain pattern [91] (see Fig.2.3 (a)), however, stripe domain patterns are observed in as grown $HoMnO_3$, $ErMnO_3$, $TmMnO_3$, $YbMnO_3$, $LuMnO_3$ crystals, as showin in Fig. 2.3, which is a re-arrangement of the figures in references [91] . Note that the entire surfaces of all as-grown crystals $RMnO_3$ (R=Ho, Er, Tm, Yb, Lu) from Fig.2.3 (b) to (f) exhibit no hint of the presence of any vortices or antivortices. These stripe lines tend to be along the [110] direction (the

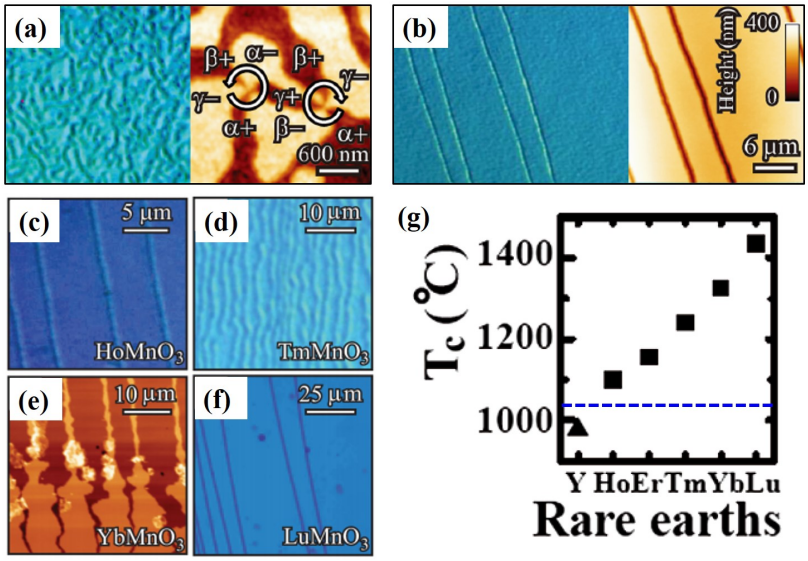

Figure 2.3: **Vortices, stripes, and T_c of $RMnO_3$, which is from rearrangement of figures in reference [91]** (a) and (b) are OM images of a chemically-etched $YMnO_3$ and $ErMnO_3$ as grown crystal surface. The left panels shows the AFM image after chemical etching, showing vortex-antivortex domain pattern and stripe domain pattern, respectively. (c)-(f) are OM images (AFM image for $YbMnO_3$ case) of $HoMnO_3$, $TmMnO_3$, $YbMnO_3$ and $LuMnO_3$ (001) as grown surfaces, all showing stripe domains. (g) is plot of relation between T_c and different rare earth element

hexagonal $P6_3cm$ notation). Note that $RMnO_3$ crystals were grown by slow cooling of the materials with Bi_2O_3 flux in the temperature range of 1200 °C and 950 °C, but the real growth through nucleation occurs probably slightly above 950 °C. Thus, $YMnO_3$ crystals are likely grown above T_c, but other $RMnO_3$ crystals below T_c. Therefore, it appears that stripe domain patterns form when the crystal growth temperature is below T_c while vortex-antivortex domain patterns are realized when crystals are exposed to temperatures above T_c (T_c's of $YMnO_3$, $HoMnO_3$, $ErMnO_3$, $TmMnO_3$, $YbMnO_3$, $LuMnO_3 \approx$ 950, 1100, 1130, 1250, 1320, 1399 °C, respectively).

The stripe domain patterns are due to crystals are grown below T_c h-$RMnO_3$ (R=Ho, Er, Tm, Yb, Lu), which is consistent with the long-range-ordered ground state of the six-state clock model with a significant third dimensional coupling. When crystals cross T_c, domain patterns with topological vortices(antivortices) are realized. The reason for the stripes domain are yet not fully understood, it's likely to be induced by the depolarization

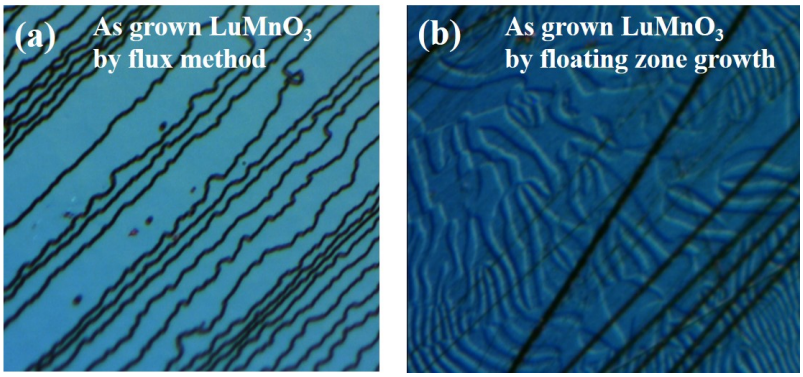

Figure 2.4: **Comparison of crystals grew by flux method and floating zone method.** (a) and (b) are OM images of crystals grew by flux method and floating zone method, showing stripe domains and vortices domains, respectively

field during the sample growth. On the other hand, as grown crystals by the floating zone method all show vortices(antivortices) since the growth temperature is much higher than the T_c, as shown in Fig. 2.4, which show the 2 distinct domain patterns of as grown $LuMnO_3$. Fig. 2.4(a) and (b) are OM images of crystals grew by flux method and floating zone method, showing stripe domain pattern and vortices domain pattern, respectively

2.2 Origin of ferroelectricity

2.2.1 Crystal structure: a simple view of ferroelectricity in $RMnO_3$

From the point view of crystal structure, the ferroelectric polarization emerging along the c axis originates from structural distortion of hexagonal lattice. A simple schematic structure of hexagonal $RMnO_3$ is shown in Fig. 2.5(a), the yellow, brown, and blue spheres denote the R, Mn, and oxygen atoms, respectively. Five oxygen atoms form a trigonal bipyramid cage, which contains the Mn ion at the center. The layer of MnO_5 polyhedra, forming close-packed planes, is separated by the layer of R ions. The ferroelectricity is characterized by the buckling of the MnO_5 polyhedra, resulting of the displacements of the R ions with non-equal portions, i.e., downward displacements of 2/3 R ions (outside R ions) and upward displacements of 1/3 R ions (center R ion) as showin in Fig.2.5(a) [48], the arrows show the directions of atomic displacements. The triangle with green bars corresponds to the

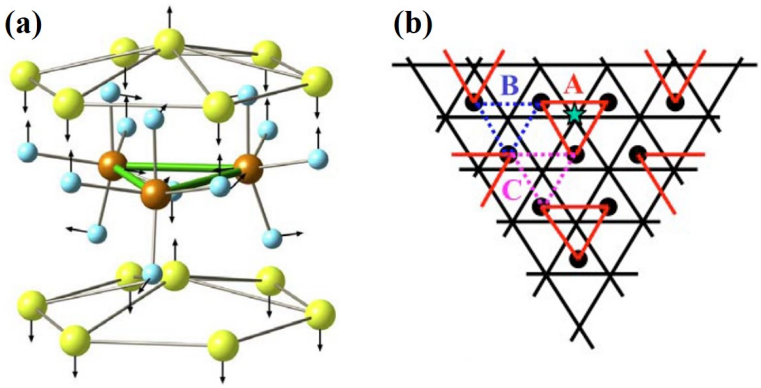

Figure 2.5: **Schematic structure of $RMnO_3$.** (a) is 3D schematic structure of hexagonal $RMnO_3$, which is from reference [48]. (b) shows three different trimerization options in Mn layer, the figure is from reference [92]

Mn trimer. Two thirds of the Y ions distort downward and one third of the Y ions distort upward, leading to ferroelectric polarization along the c axis.

The Y ion distortions and the trimerization of Mn ions in each Mn layer result from tilting of MnO_5 polyhedra. Within the Mn layers, there are 3 different options for Mn trimerization, as shown in Fig. 2.5(b) [92], the A, B, and C are label as α, β and γ. The structural distortion is induced by the sequence of the transition from high-temperature paraelectric phase $P6_3/mmc$ to low-temperature ferroelectric phases: $P6_3cm$ or $P\bar{3}c1$, the latter is the space group for Ga-doped hexagonal $InMnO_3$ or intermediate state, which will be discussed in the corresponding chapter. This sequence of transition has been the subject of debate [93–96].

2.2.2 First principle calculation of the ferroelectricity in $RMnO_3$

From the point view of first principle calculation, in the paraelectric $P6_3/mmc$ phase, all the ions are confined in the same ab plane, whereas this mirror plane symmetry is broken in ferroelectric $P6_3cm$ phase. First-principles density-functional calculations found that the K_3, zone-boundary mode at q = (1/3, 1/3, 0), has the largest amplitude. This mode is also called trimerization, i.e. the unit cell triples and forms a $\sqrt{3} \times \sqrt{3}$ superlattice structure. The zone-center polar mode (Γ_2^-), which is responsible for the ferroelecticity, is a by-product

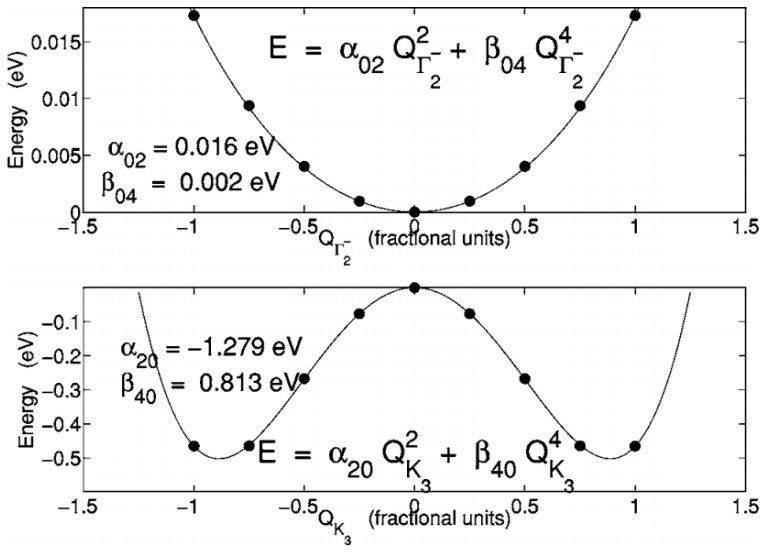

Figure 2.6: **The energy as a function of polar and trimerization modes.** upper panel is $Q_{\Gamma_2^-}$ mode and lower panel Q_{K_3} panel. The figure is from reference [97]

of the primary trimerization mode, stemming from the cross-coupling term between Q_{K_3} and $Q_{\Gamma_2^-}$ [97].

To be more specific, by expanding the free energy to the fourth order in Q_{K_3} and $Q_{\Gamma_2^-}$ including all symmetry-allowed terms, the free energy can be shown as:

$$F(Q_{K_3}, Q_{\Gamma_2^-}) = \alpha_{20}Q_{K_3}^2 + \alpha_{02}Q_{\Gamma_2^-}^2 + \beta_{40}Q_{K_3}^4 + \beta_{04}Q_{\Gamma_2^-}^4 + \beta_{31}Q_{K_3}^3Q_{\Gamma_2^-} + \beta_{22}Q_{K_3}^2Q_{\Gamma_2^-}^2 \quad (2.1)$$

As shown in Fig.2.6, the polar mode is stable due to the positive α_{02} coefficient, showing a single well potential. On the contrary, the negative α_{20} coefficient results in the double-well potential in terms of K_3 mode. Therefore, the primary ordering is the buckling of the MnO_5 polyhedra, and the polarization cannot emerge spontaneously with the $Q_{\Gamma_2^-}$ mode only. In the presence of the cross coupling terms, the equilibrium position of $Q_{\Gamma_2^-}$ starts to shift to a positive value with nonzero Q_{K_3}, resulting in a polarization, and it grows with increasing Q_{K_3}, the K_3 mode plays a role of kicking the polarization to nonzero equilibrium position, which is analogous to a crystal field [97]. This coupling mechanism suggests that hexagonal manganites are improper ferroelectrics. Note that for small magnitudes of the

K_3 mode, the polar mode appears only as a third-order term, so the magnitude of the polarization just below T_c is vanishingly small. This critical point indicates the emergence of the vortex domain pattern is not influenced by the systems attempts to minimize the depolarizing field from the ferroelectric polarization. A Strong evidence for this point is that large numbers head-to-head and tail-to-tail domain walls has been found in $RMnO_3$ [87, 98], which rarely happen in conventional ferroelectrics.

2.2.3 Landau theory: topological $\mathbf{Z}_2 \times \mathbf{Z}_3$ vortex

As we discussed above, we have found the vortex is assigned with configuration of (α+, β-, γ+, α-, β+, γ-) or (α+, γ-, β+, α-, γ+ , β-,), showing alternating ferroelectric and trimerization phases. The boundary between different domain is defined as antiphase boundary (APB). The high-resolution ($\sim$ 10 nm) TEM observation [48, 99, 100] has identified the presence of structural APBs which indicating the interlock of the ferroelectric domain walls and antiphase domain walls.

A theoretical study of vortices in hexagonal manganites based on Landau theory with parameters determined from first-principles calculations outlines the free energy landscape in terms of the trimerization amplitude Q and phase Φ by Artyukhin *et al.* [101]. The free-energy expansion in powers of Q; Φ; P, and their gradients

$$F(Q,\Phi,P) = \frac{a}{2}Q^2 + \frac{b}{4}Q^4 + \frac{Q^6}{6}(c + c'\cos(6\Phi)) - gQ^3P\cos(3\Phi) + \frac{g'}{2}Q^2P^2 + \frac{a_p}{2}P^2 + \frac{1}{2}\sum_{i=x,y,z}[s_Q^i(\partial_i Q\partial_i Q + Q^2\partial\Phi\partial\Phi) + s_P^i\partial_i P\partial_i P] \quad (2.2)$$

where P is polarization under the generators of the high-temperature space group. $\partial_i = (\partial/\partial x_i)$ where x and y are the Cartesian coordinates in the ab plane.

Note that the trimerization phase Φ is critical in the theory of topological defects. In particular, the form of the nonlinear coupling, $-gQ^3P\cos(3\Phi)$, giving rise to improper ferroelectricity, implies that for g >0 the electric polarization induced in the states with Φ

$= 0$, $+2\pi/3$ and $-2\pi/3$ is positive which are corresponding with the ($\alpha+$, $\beta+$, $\gamma+$) phases, whereas for $+\pi/3$, π and $-\pi/3$ it is negative which are corresponding with (γ-, α-, and β-) phases. In other words, neighbouring trimerization phases, separated by $\Delta\Phi = \pi/3$, have opposite electric polarizations. This is consistent with what we observed in the experiments, like what we found in the Fig. 2.1, with alternating trimerization and ferroelectric phases. Moreover, it reveals that the lowest energy domain wall configuration is the shortest path connecting two neighbouring states whose phase.

Moreover, the K_3 mode is independent of the angle of the tilt until the polar mode subsequently develops, which suggesting the potential energy below the T_c can be plotted by the continuous Mexican hat form. The contour plot shows a Mexican hat shape, indicating the six ground states at low energy, where is the brim of the hat, which are related with ($\alpha+$, β-, $\gamma+$, α-, $\beta+$, γ-) phases. This means from high energy to low energy, the symmetry has been reduced from $U(1)$ symmetry to the sixfold discrete symmetry, which can be described by Z_6. As shown in Fig. 2.7 which is re-arrangement of figures in references [101, 102] . Since the symmetry broken only happened when trimerization K_3 mode and polar mode

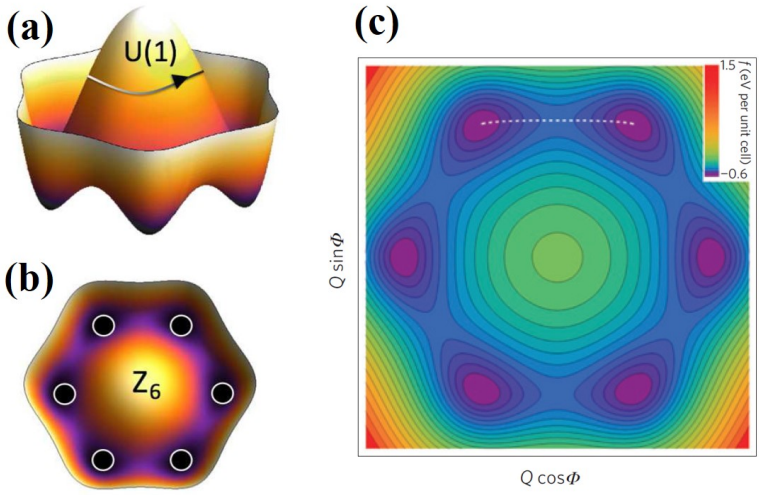

Figure 2.7: **Plot of potential energy in form of Mexican hat.** (a) and (b) are schematics of Mexican hat showing Z_6 nature of vortex, (c) is the Contour plot of the free energy of uniformly trimerized states as a function of Q and Φ. Figures are taken from references [101] and [102]

develop, so the emergent vortex structure can also be described as $Z_2 \times Z_3$ vortex.

2.3 Type-I and Type-II domain networks

A self-organized network of vortices and antivortices in h-$RMnO_3$ has been found as we shown in the Fig. 2.1 (c). It is intriguing, but seemingly irregular configurations of a zoo of topological defects, however, it has been proved that the domain network can be neatly analyzed in terms of graph theory which reflecting the nature of complex phenomena [103].

The networks of vortices are found to be in two different types: type-I domains with roughly equal fractions of upward and downward polarization domains as shown in top panel of Fig. 2.8 (a), and type-II domains with one dominant polarization displayed in Fig. 2.8 (b). Bottom panels are TEM images showing the difference between the type I and type II domain patterns.

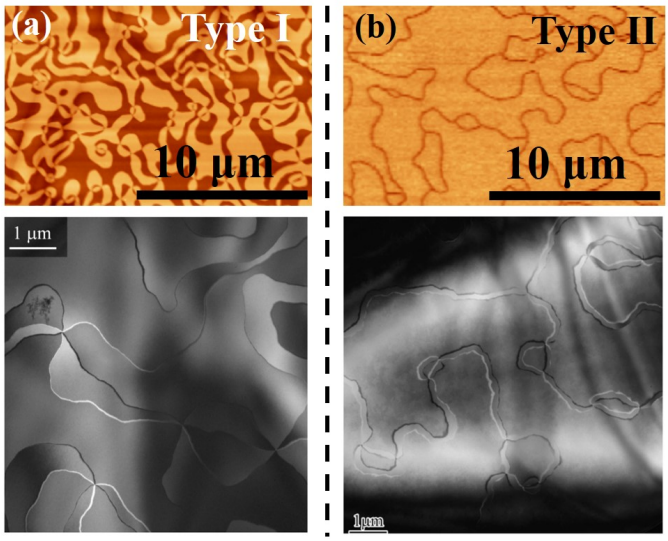

Figure 2.8: **Type-I and type-II vortex domain networks.** top panels of (a) and (b) are PFM scanning images showing type-I and type-II domain networks, respectively, the bottom panels are TEM images. (TEM imagse are courtesy of Prof. Yoichi Horibe and Prof. Sang-Wook Cheong)

2.3.1 Electric field poling

The main difference between Type-I and type-II domain networks is the dominance of one ferroelectric polarization domain, which suggesting that either up or down polarization is favored for type-II domain. An internal self-electric-poling effect was proposed to be responsible for the dominance of one polarization domains, which may be induced by oxygen off-stoichiometry near the surfaces [103]. Following this logic flow, applying a large external electric field should be able to result in switching type-I domains to type-II domains.

The result of electric field experiment is displayed in Fig. 2.9. External electric poling experiment was performed on an $YMnO_3$ crystal with two Ag electrodes on the top and bottom *ab* surfaces [104]. We applied an external electric field of 200 kV/cm, which is larger than the coercive field of $YMnO_3$. After electric field poling at 77 K, the Ag electrodes were removed mechanically. After chemical etching of the poled crystal, atomic force microscope (AFM) scanning experiment was performed across the boundary (white dashed

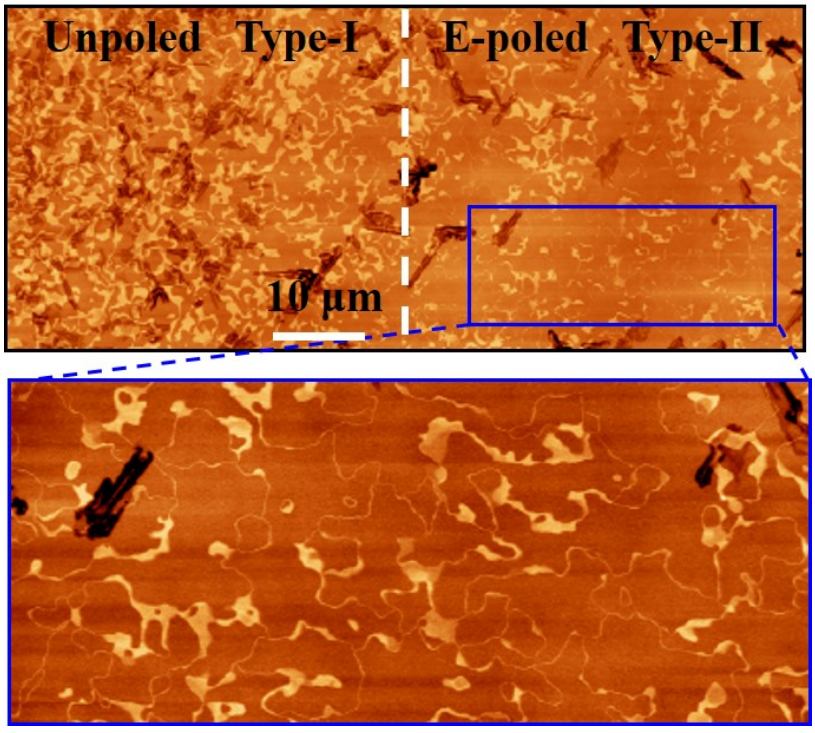

Figure 2.9: **AFM imaging of electric-poled $YMnO_3$.** Electric poling changes type-I domains to type-II domains

line) between the poled region and un-poled region.

The un-poled region (the left side of white dashed line) exhibits type-I domains with roughly half and half distribution of upward and downward polarization domains, but the negative electric poled region (the left side of white dashed line) shows more-or-less type-II domains (dominant dark domains with upward polarization and narrow bright domains with downward polarization). The blue boxed region in the top panel is enlarged in the bottom panel, where type-II domains seem evident in the electric poled region. We emphasize that compared with self-poling, a part of un-favored bright domains in type-II domains after poling are still somewhat broad, which demonstrates that electric poling is not very uniform unlike chemistry driven self-poling.

2.3.2 Oxygen off-stoichiometry induced self-poling

The oxygen vacancy formation for bulk crystal and films at different depths from the surface leads to compounds deviating from the ideal stoichiometry. The capability to control oxygen vacancies is critical to realize the full potential of different kinds of ferroelectric materials because that ions can provide surface charge compensation for electric polarization. For example, like perovskite $SrTiO_3$ [105, 106] and corundum structure $LiNbO_3$, note that Li defect gradient results in abundant charged ferroelectric domain walls in $LiNbO_3$ [107–109], and a ferroelectric mono-domain can be reversibly induced by varying oxygen stoichiometry [110]. Thus, controlling chemical composition can results in manipulation of domains and functionalities of ferroelectric and pyroelectric materials, including hexagonal manganites.

The mechanism of formation of oxygen vacancy in h-$RMnO_3$ is described as follow: when a h-$RMnO_3$ crystal is heated to high temperatures above, for example, 1000 °C, due to sufficient thermal energy and large ionic diffusion, the crystal tends to have rather uniform oxygen vacancies throughout the entire crystal. However, during cooling process in atmosphere with sufficient oxygen, around a 700 °C range, oxygen diffusion into the crystal occurs, but is limited in the surface area due to a limited diffusion length, unless the cooling

rate is unrealistically slow. Thus, it is natural to have an oxygen vacancy gradient from the surface to inside of a crystal; in other words, surface is more-or-less oxygen stoichiometric, but significant oxygen vacancies may exist inside of the crystal.

In order to explore the effect of oxygen off-stoichiometry on domain networks, we annealed two $HoMnO_3$ single crystals together above T_c in Ar atmosphere, and slowly cooled to 1000 °C in 2 hours. Afterwards, they were quickly cooled down to room temperature to avoid any surface oxidation at lower temperatures.

After this heat treatment, one crystal was chemically etched, and its OM image is shown in Fig. 2.10 (a). The crystals are expected to have uniform oxygen vacancies throughout the entire crystals whihc is shown in Fig. 2.10 with roughly half-half distribution of upward and downward polarization domains in the entire surface. In other words, there is no preference between upward and downward polarization domains after this heat treatment.

The second crystal was re-annealed in air at 700 °C for 5 hours, and then followed by

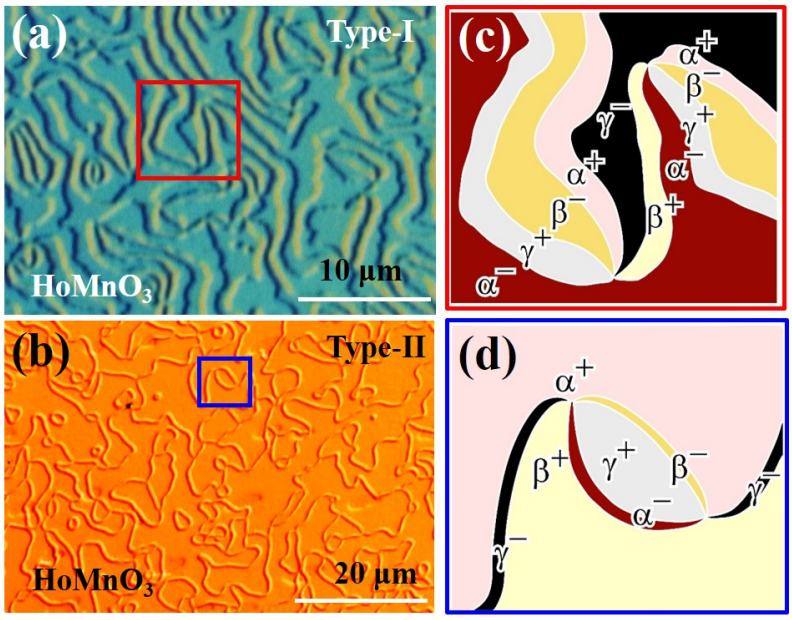

Figure 2.10: **OM images of $HoMnO_3$ after chemical etching.** (a) shows type-I vortex network. (b) displays the crystal re-annealed at 700 °C in air which showing type-II vortex network. The corresponding schematics for the boxed regions are displayed in (c) and (d), respectively.

furnace cooling. This re-annealing in air is expected to result in oxidation of only near surfaces of the crystal due to limited oxygen diffusion length. As shown in Fig. 2.10(b), the crystal surface after this re-annealing shows type-II domains with narrow downward polarization domains and broad upward polarization domains. The large gradient of oxygen vacancies with less oxygen vacancies near surfaces results in an effective upward internal electric field, which results in the energetic preference of upward polarization domains.

Furthermore, the Type-II domains near the surface induced by oxygen vacancy gradient change into type-I domains inside of the crystal which can be investigated with sequential etching. One $LuMnO_3$ crystal was heat-treated at 1450 °C in air, and then followed by furnace cooling to room temperature. The crystal was minimally etched for 10 mins to reveal the domain pattern on the crystal surface. Its OM image shown in Fig. 2.11(a) reveals clearly type-II domains on the crystal surface. However, the identical area after additional 30 minutes etching unveils type-I domains inside of the crystal as shown in

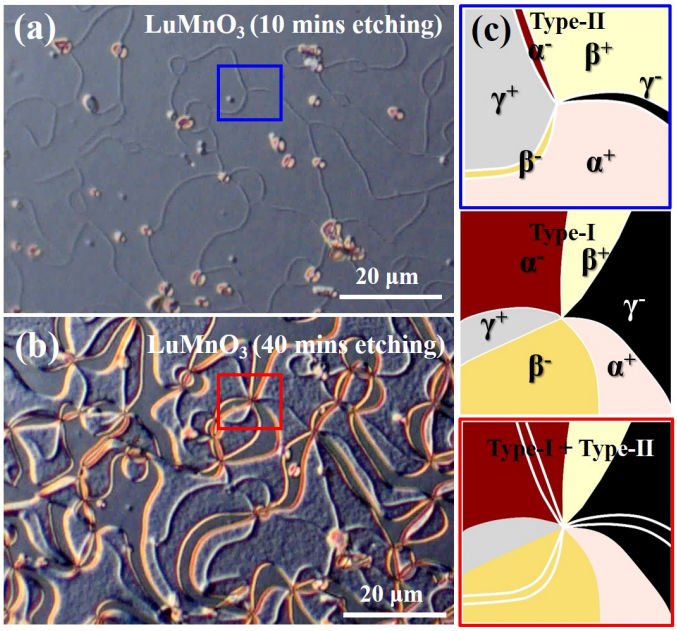

Figure 2.11: **Evolution from type-II to type-I domains with sequential etching of $LuMnO_3$.** (a) OM image of a $LuMnO_3$ crystal surface after 10 minutes chemical etching, showing type-II domains on the surface. (b) OM image on the identical region after additional 30 minutes etching. Type-I domains appear in addition to the original type-II domains. (c) Schematics for the boxed region and type-I domain

Fig. 2.11(b). The schematics in Fig. 2.11(c) for the boxed areas in Fig. 2.11(a) and (b) show type-II domains (top) at the surface and inside type-I domains (middle). In fact, the combined cartoon (bottom) with both type-I and type-II domains corresponds to the image in Fig. 2.11(b).

This chemistry driven self-poling was also demonstrated by AFM scanning in $YbMnO_3$ and $LuMnO_3$. Fig. 2.12 (a) displays the type-I domain network of a $YbMnO_3$ crystal (due to no self-poling effect), which is annealed at 1350 °C, followed by furnace cooling to 1180 °C, and then quenched to room temperature in Ar flow. In contrast, another $YbMnO_3$ crystal was annealed at 1350 °C, and then furnace cooled in air. Due to oxygen absorption only near surfaces during cooling process, an oxygen vacancy gradient from the crystal surface

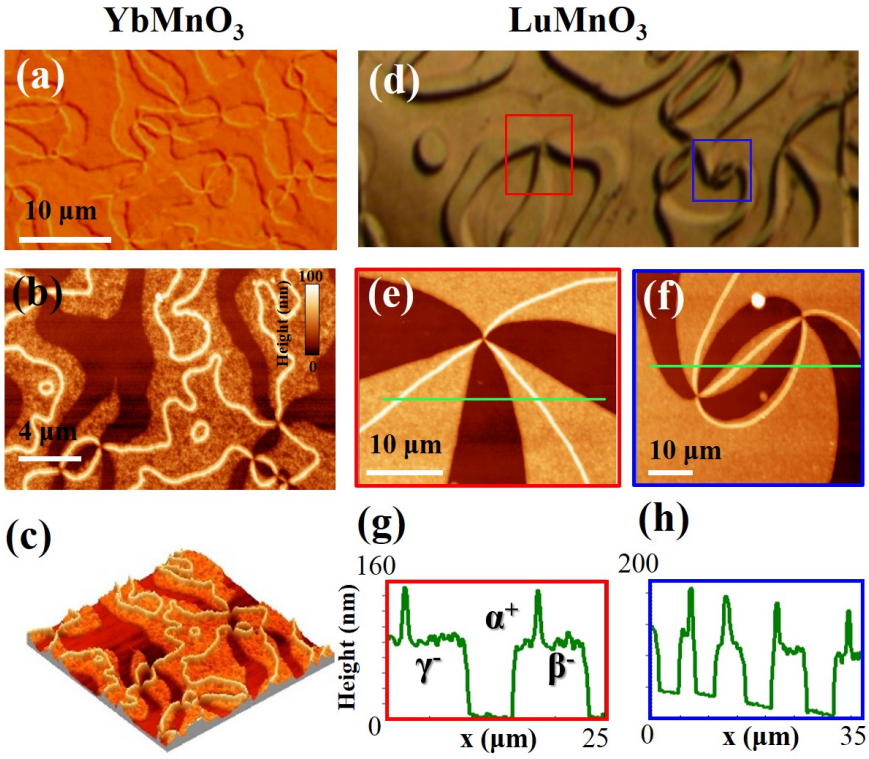

Figure 2.12: **Evolution from type-II to type-I domains in both $YbMnO_3$ and $LuMnO_3$.** (a) exhibits type-I domains, but that of another $YbMnO_3$ crystal annealed in air shown in (b) demonstrates a self-poling effect near the surface. (c) is the corresponding 3D image. (d)-(f) shows the similar behavior in $LuMnO_3$, (g) and (h) indicate the line scan of green lines.

to interior exists in the crystal. This leads to a self-poling effect and type-II domains near surface, which results in the bright narrow lines in the AFM scanning image in Fig. 2.12(b). However, inside of the crystal where oxidation during cooling did not occur due to oxygen diffusion limit, the evolution of domain configuration is better shown in Fig. 2.12(c), which is the 3D image of Fig. 2.12(b).

A similar behavior is in $LuMnO_3$ is displayed in Fig. 2.12(d)-(h). The specimen was heated to 1410 °C, and then furnace-cooled down to room temperature in air. After chemical etching, OM image was taken on the crystal surface, and is displayed in Fig. 2.12(d). AFM scanning experiments were performed on the red boxed and blue boxed regions, of which AFM images are displayed in Fig. Fig. 2.12(e) and (f), respectively. Line-scan profiles of both images ((g) and (h)) along the green lines clearly show the surface type-II domains with un-favored narrow domains and the deep-inside type-II domains. Note that the sharp change from type-II to type-I domains induces the plateaus of middle-contrast domains, which defines charged tail-to-tail domain walls with different trimerization antiphase domains, flat along the *ab* plane.

With even more complicated oxygen vacancy distribution, one can observe type-II to type-II change, like Fig. 2.13 which is one $YbMnO_3$ crystal embedded in polycrystalline powders, was annealed at 1350 °C, slowly cooled to 1320 °C with 30 °C/hour, and then fast cooled to room temperature in air. Due to oxygen trapped in powders and slow cooling across T_c. Wavy type-II domains on the crystal surface are due to fast cooling in the oxygen absorption temperature range such as 650-800 °C, but smooth type-II domains are found inside of the crystal, as shown in the AFM image of Fig. 2.13(a). These inside type-II domains are due to a non-uniform oxygen vacancy distribution inside of the crystal. The corresponding schematic for the oxygen vacancy distribution and line-scan profile along the green line are displayed in Fig. 2.13(b). Note that in the oxygen vacancy distribution cartoon in (b), the y axis is depth in nanometers and the x axis is oxygen vacancy concentration of $RMnO_{3-\delta}$. A semi-quantitatively calculation of δ is around 0.02. Schematics for

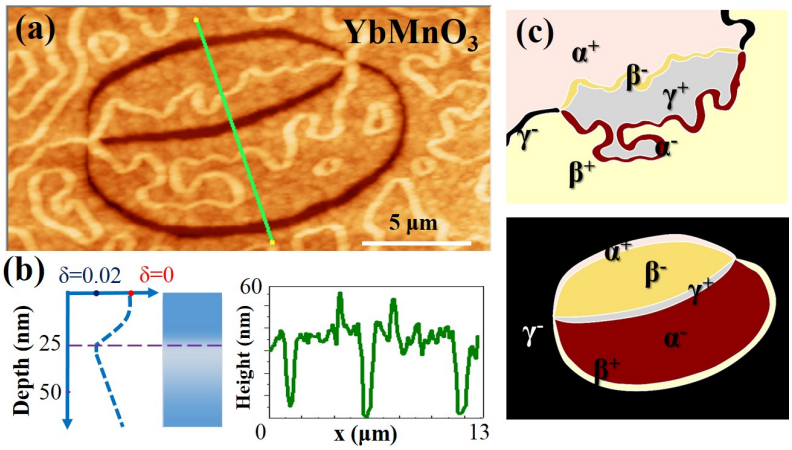

Figure 2.13: **Embedded-annealed $YbMnO_3$ after chemical etching.** AFM scanning image of one vortex-antivortex pair is displayed in (a). The corresponding schematic for the oxygen vacancy distribution and line-scan profile along the green line are displayed in Fig. 5(b). Schematics for domains near the surface and inside are displayed in the top and bottom of Fig. 5(c), respectively.

domains near the surface and inside of the crystal are shown in the top and bottom of Fig. 2.13(c) Note that the surface domains and the inside domains share identical vortex cores, consistent with the notion that the density of vortex cores mostly depends on the cooling rate cross T_c.

By assuming the effective electric field induced by oxygen vacancy gradient same with that in the electric poling experiment (200 kV/cm) and the oxygen content of the oxidized surface exactly 3, and using the dielectric constant of $ErMnO_3$ [111], we estimate the oxygen vacancy concentration of the bulk $RMnO_{3-\delta}$ crystal to be δ=0.02. Note that this bulk oxygen content is very close to 3, and the oxidized surface region is very thin (on the order of 100 nm), so it is impractical to measure the oxygen vacancy concentration experimentally.

2.4 Graph theory, N-gon analysis and Preferential attachment

2.4.1 Graph theory and N-gon analysis of vortices network

Graph theory, basically speaking, is trying to study graphs. As it developed over centuries, now it has been a powerful tool for mathematics, economics and computer science

to understand many real configurational problems in analyzing the nature of underlying connectivity. Graphs consist of two sets: a nonempty set of objects (vertices) and a set of the connections (edges) among the objects.

4 color theorem is a basic and simple example for analyzing graphs. It has been defined as: for any kind of 2D map, no more than four colors are required to color the regions of the map so that no two neighboring regions have the same color, note that two regions have to share a common boundary, not a corner. A simple example is shown in Fig. 2.14(a), which is well known as a checkerboard. For each smallest square (or we can define it as face or domain), it has 4 edges (4-valent) and 4 vertices (4-gons), hence it is called 4-valent graph with 4 gons. Since it has a well defined periodicity or underlying "constraint", only 2 colors (black and white) are needed for label this graph so that no neighboring domains has the same color. In graph theory language, we call this checkerboard graph as 2-proper-colorable graph.

Similarly, for the intriguing domain networks in h-$RMnO_3$, all the vortices have six edges (6 domain walls), and each domain is surrounded by N (even integer) nodes/edges which we called a 6-valent graph with N-gons. Due to the topologically protected vortices, only 3

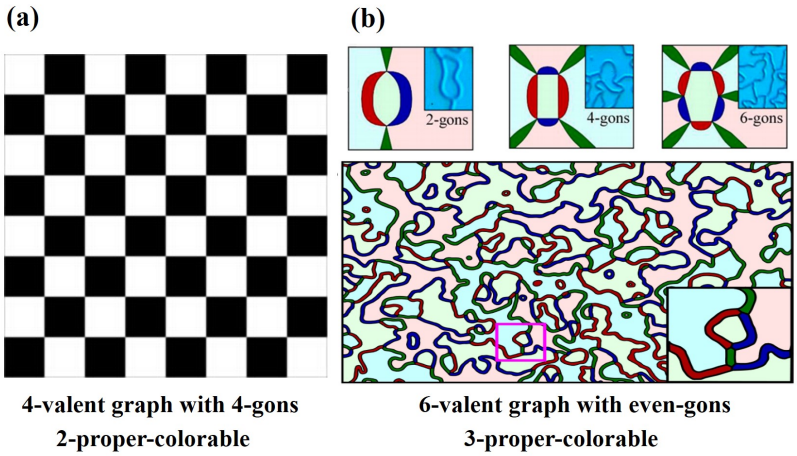

Figure 2.14: **Graph theory on checkerboard and network of vortices.** (a) shows checkerboard which is 4-valent graph with 4 gons and 2 proper colorable graph. Top panel of (b) shows the examples of 2-gons, 4-gons and 6-gons, bottom panel shows vortices domain network which is 6-valent graph with even-gons, and it is 3 proper-colorable network.

colors are needed for coloring the domain network, which gives 3-proper-colorable domain network, as shown in Fig. 2.14: examples for 2-gons, 4-gons and 6-gons are given in the top panel of Fig. 2.14 (b). Note that in bottom panel of Fig. 2.14 (b), light and dark blue, green and red are used for distinguishing upward and downward polarizations, so in total it's 6 different colors. But 3 colors are sufficient to label it. A complete mathematical proof of $Z_2 \times Z_3$ coloring for 6-valent graphs with even-gons is shown in the supplementary information of reference [104].

As we realized, domains with 2-gons are largely dominant, and domains with larger gons are rarer. The distribution of N-gons has not been fully studied except reference [103], in which the research only focus on type-II domain network and the analyzed region is rather small.

To reveal the underlying mechanisms for the different statistical distributions in the type-I and type-II networks, we performed N-gons analysis on 3 different samples: $YbMnO_3$ with type-I domains, $ErMnO_3$ with an intermediate state between Type-I and Type-II domains, and $YMnO_3$ with type-II. $YbMnO_3$ and $YMnO_3$ specimens were chemically etched with phosphoric acid at 150 °C for 30 minutes to reveal the domain pattern on surfaces, the $ErMnO_3$ specimen is over-etched. Large-range OM and AFM images were taken, showing in Fig. 2.15 [66]. For better visualization, only parts of analyzed images are shown. Fig. 2.16 shows an AFM image on $YbMnO_3$, and the blue-boxed region is magnified in the right panel. Green (blue) stars represent vortices (antivortices), and each domain was labeled with its N of N-gons. Similarly, $ErMnO_3$ is shown in Fig. 2.17, and $YMnO_3$ is shown in Fig. 2.18.

The detail of analysis method is illustrated by using $YMnO_3$ as an example: first step is defining a vortex arbitrarily, then the entire image can be labeled in a proper manner following 2 rules: (i) all domains are characterized as even integer N gons, and (ii) the domain network is 6-valent graph, which means each vortex-antivortex core has 6 domains merged at one point. All vortices (antivortices) were labeled with red circles (yellow circles).

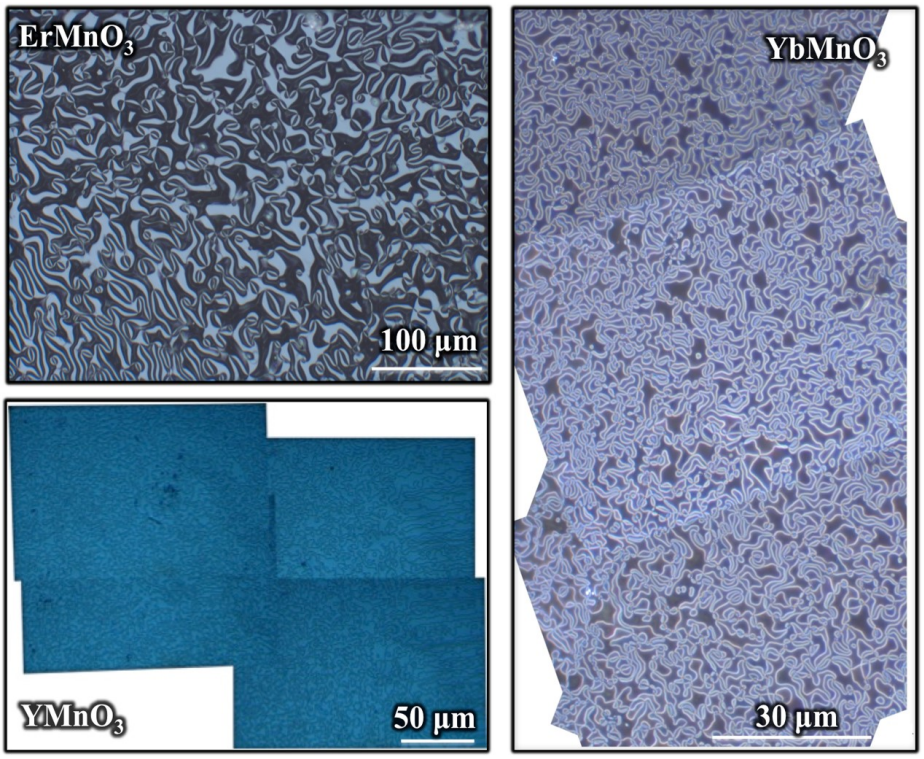

Figure 2.15: **Large-range Optical images of $ErMnO_3$, $YMnO_3$ and $YbMnO_3$.**

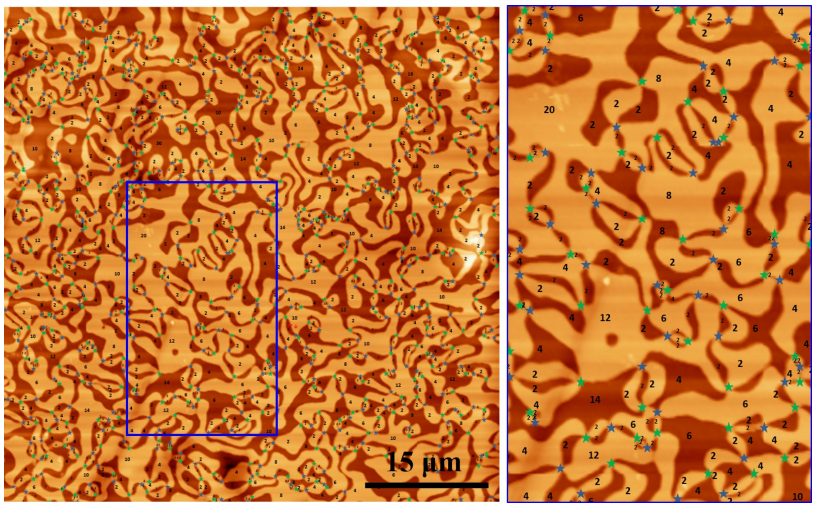

Figure 2.16: **AFM scanning image on a chemically etched $YbMnO_3$ crystal.** Details of N-gons analysis are labeled, in the blue boxed region, green (blue) stars represent vortices (antivortices), and each domain was labeled with its N of N-gons.

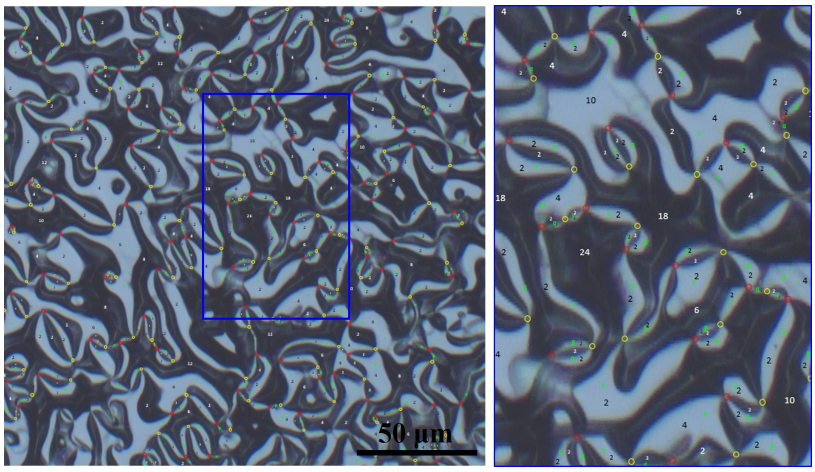

Figure 2.17: **OM image on a chemically etched $ErMnO_3$ crystal.** Details of N-gon analysis are labeled: red (yellow) circles show vortices (antivortices), each domain is labeled with its N of N-gons, and its trimerization phase is shown for each bright domain.

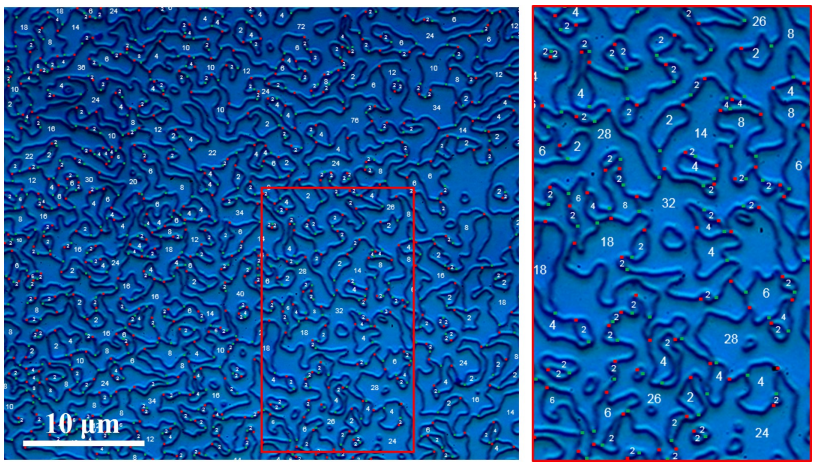

Figure 2.18: **OM image on a chemically etched $YMnO_3$ crystal** Details of N-gon analysis are labeled: green (red) dots shows vortices (antivortices), and each favored domain is labeled with its N of N-gons.

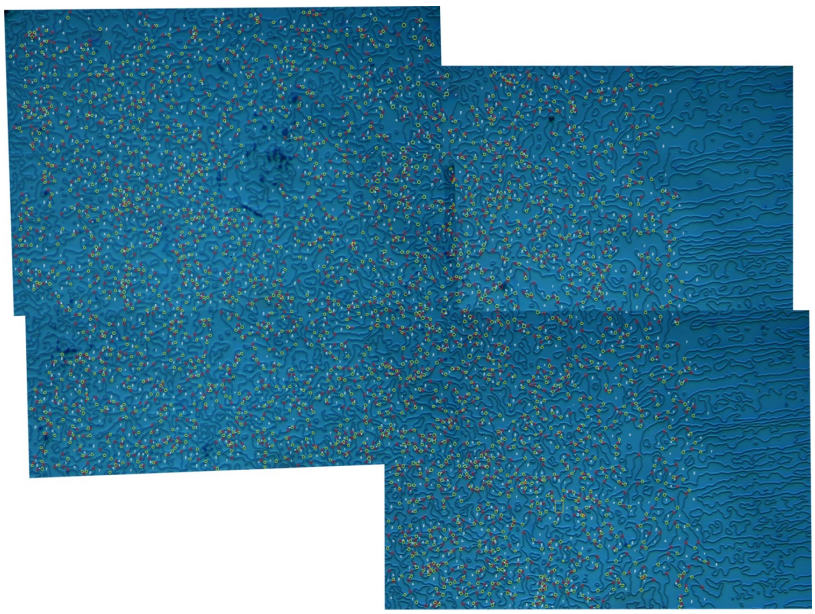

Figure 2.19: **$YMnO_3$ crystal after vortex-antivortex analysis.** All vortices (antivortices) were labeled with red circles (yellow circles).

To ensure accuracy, the number of vortices along every face were counted and matched with the characteristics of Type I and Type II patterns dictated by graph theory. See Fig. 2.19

Second step is: getting exact coordinates of the vortex and antivortex pairs by using Origin program. The size of the composite image was calculated to be $209\mu m \times 146\mu m$ for $YMnO_3$. The data points were then sorted by vorticity, plotted on a scatterplot and processed using statistical analysis. See Fig. 2.20. A overlap image of original OM image and coordinates image is shown in Fig. 2.21.

All three samples are analyzed by this method, which provides a fruitful playground for understanding the statistical behavior of different network of vortices. The data from three different samples are used in next section about scale free distribution and in Chapter 4 about the correlation function analysis.

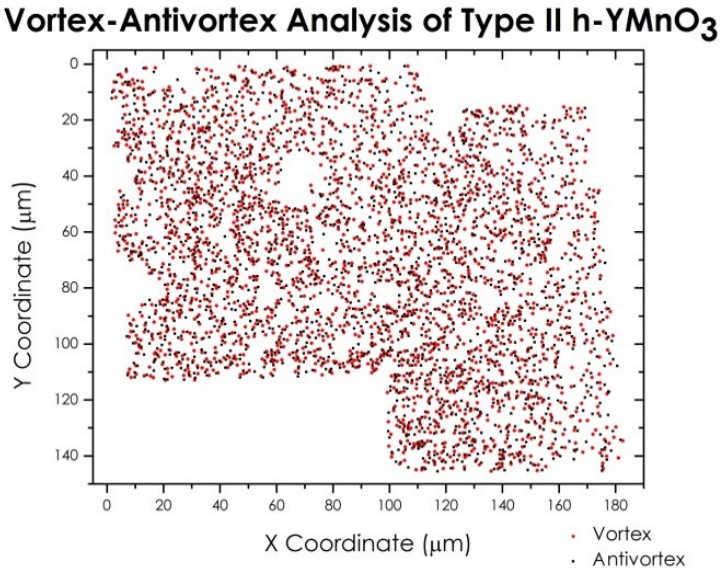

Figure 2.20: **Coordinates of $YMnO_3$ crystal after vortex-antivortex analysis.** All vortices (antivortices) were labeled with red dots (black dots).

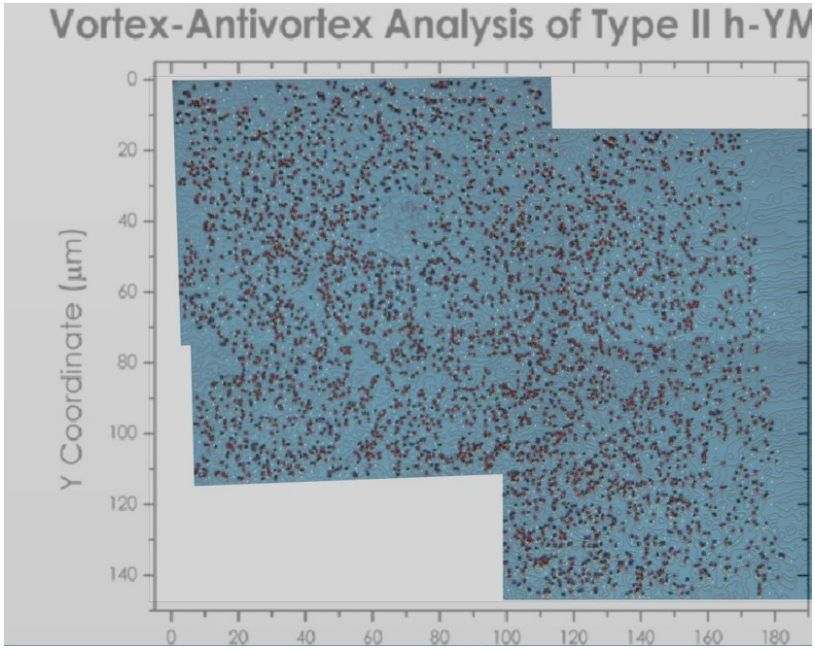

Figure 2.21: **Overlap of OM image and coordinates data**

2.4.2 Preferential attachment or Self-organized criticality?

Complex networks like neural networks, internet network and movie actor collaboration networks are a network with non-trivial topological features, which are absent in simple networks such as crystal lattice [112–117]. Some complex networks demonstrate scale-free power-law degree distributions, which attract enormous attention due to the notable characteristics such as relative commonness of vertices with a degree that largely exceed the average, and small average distance between two vertices.

There are, in general, two ways for scale-free power-law distribution, one is preferential attachment and another is SOC. Domain network of vortices in term of distribution of N-gon, as we realized [103], can be viewed as complex network, and potentially has direct relation with SOC. In order to figure out the physics lying behind the domain network, we plot out N-gon analysis for 3 samples analyzed as discussed above.

N-gon analysis of these 3 samples are shown in Fig. 2.22, from left to right, they are from $YbMnO_3$, $ErMnO_3$ and $YMnO_3$. The type-I network can be approximated by an exponential function with a sharp cutoff for large N. The exponential-law distribution of the N-gons in type-I networks indicates that the corresponding dual graph shows an exponential degree distribution, and an exponential degree distribution was also observed in other networks [117, 118].

On the other hand, a type-II network is better approximated by a power-law distribution $1/N^2$, as shown in Fig. 2.22 (c). A network with a power-law degree distribution is called a scale-free network, and it has been shown that the scale-free architecture has a strong effect on the SOC phenomenon [116, 119]. What's interesting here is: there is a tendency of slope tilting when the domain pattern changing from type-II to type-I: starting from Type-II the slope of bright domain (unfavored domain) tilts to a bigger number and eventually becomes one single point (star label in Fig. 2.22 (c)), which indicating all the 2 gons for the unfavored domains in type-II domain network.

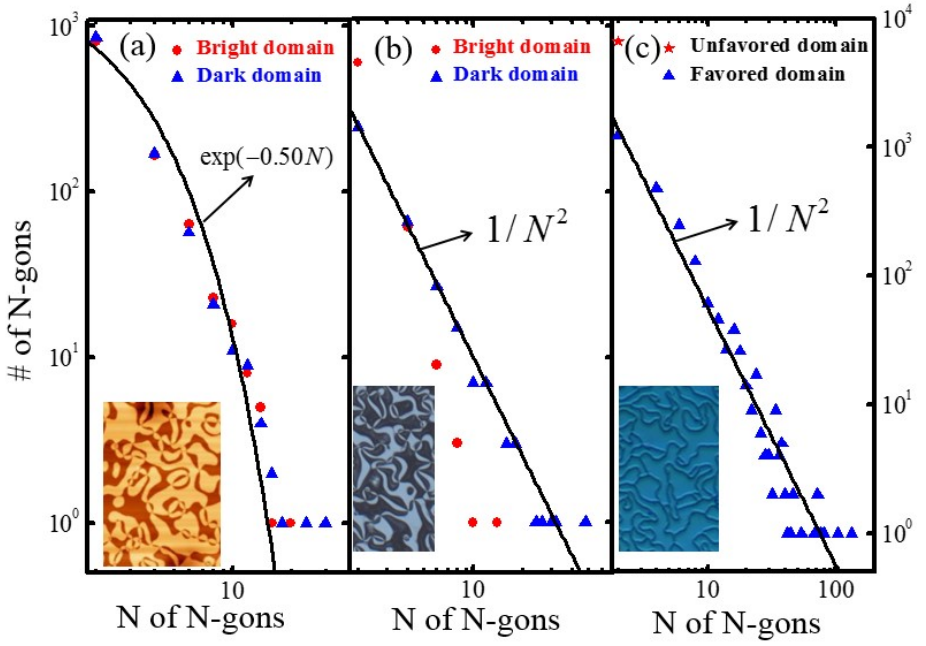

Figure 2.22: **N-gon statistical analysis.** (a) An exponential-law distribution within a type-I network in $YbMnO_3$. (b) An intermediate network in $ErMnO_3$ crystal. (c) A power-law behavior within a type-II network in $YMnO_3$.

As we know, an external electric field or internal oxygen off-stichometry induced self-poling electric field are able to convert type-I domain network into type-II network. To examine the domain evolution process under an electric field, phase-field simulation [120] has been performed by Xue Fei and Long Qing Chen at PSU (will be pubulished). From the results of simulation, type-I networks exhibit a lognormal N-gon distribution with the logarithms of its numbers normally distributed, in contrast to the scale-free power-law distribution in type-II networks.

Based on the simulation, coalescing and splitting of the N-gons during the transition between the two types of networks are responsible for the change of N-gon distributions. Preferential attachments (behaviors that the N-gons with larger N have higher probability to coalesce with other N-gons) are shown to be responsible for the existence of the power-law distribution, which reflect preferential is the main reason for scale-free power-law in vortex networks. The main problem is: according to SOC, the system has to be dynamical and

reach a equilibrium, like "forest fire model".

Note that when network of vortices change from type-I to type-II, Z_2 symmetry is broken, (it could be understood that the symmetry broken happens in the process of applying an electric field on type-I domains with $Z_2 \times Z_3$ symmetry). One can define an order parameter, e.g. the total polarization, to reflect the symmetry breaking. So the transition from type-I to type-II domains can be considered as a phase transition.

2.5 Vortex fragmentation

Vortex core splitting is a rare phenomenon, however draws lots of attentions since it might suggest the breakdown of topological protection in topological vortices. Fig. 2.23 are collection of reported core fragmentation recently of 4 references [121–124]. (a) is a TEM image of core fragmentation on the surface perpendicular to *ab* plane of $ErMnO_3$. b) shows

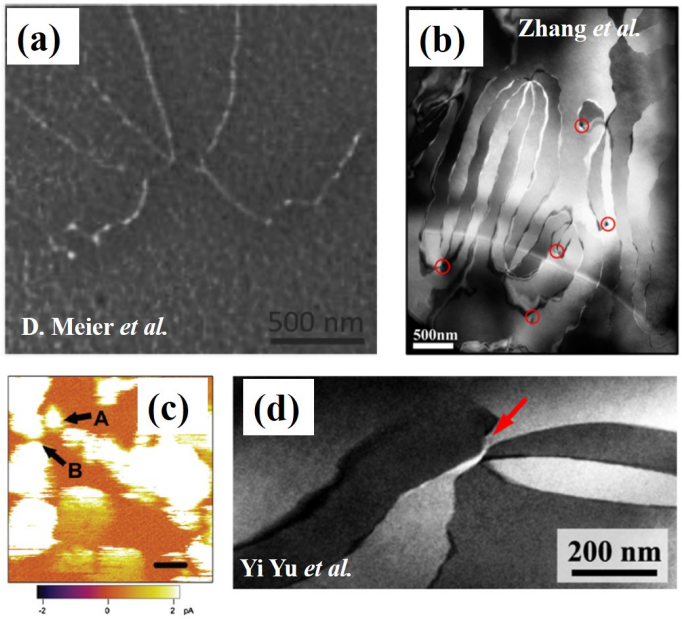

Figure 2.23: **Collection of reported core fragmentation, which are from references [121-124]** (a) TEM image of core fragmentation on the surface perpendicular to *ab* plane of $ErMnO_3$. (b) shows dark-eld TEM image of the domains pattern with broken and closed domain walls. (c) is c-AFM image on $YMnO_3$ showing core splitting when increasing electric poling voltage. (d) shows a vortex-like pattern where different domains do not converge into a point on $YMnO_3$

dark-eld TEM image of the domains pattern with broken and closed domain walls. Note that (b) is different since there is no core splitting, the broken domain walls are highly possible due to the defects pinning during the sample growth. (c) is c-AFM image on $YMnO_3$ showing core splitting when increasing electric poling voltage. (d) shows a vortex-like pattern where different domains do not converge into a point on $YMnO_3$, the channel in the core region is indicated by the arrow.

Theoretically, Toledano *et al.* [121] state that vortices in the *ab* plane originate in the $\bar{6}$m2 high-symmetry lattice point of the paraelectric unit cell. In contrast, vortices in planes parallel to the c axis are expected to fragment, which is consistent with the examples in Fig. 2.23(a) (b) and (d).

In our experiments, we have discovered similarly phenomenon in $YbMnO_3$, however, in *ab* plane, rather than containing *c* plane, as displayed in Fig. 2.24, which is completely different from their theoretical and experimental results. This annealed crystal was polished only one side, and was ion-milled only at the polished surface, so the final specimen is mostly the un-polished virgin surface region. Fig. 2.24(a) shows a $7.5\mu m \times 3.5\mu m$ large-range superlattice DF-TEM (JEOL-2010F) image performed by using a superlattice spot g+=1/3(1 1 6). Bright and dark contrast originates from the Friedels pair breaking due to the presence of 180° ferroelectric domains. The red, blue and green-boxed areas in Fig. 2.24(a) exhibit broken vortex cores. This vortex core split is clearly visible in the magnified images in Fig. 2.24(b), (c) and (d). One pair of type-I vortex and antivortex, where six domains merge at each core, can be found at the right-hand-side top of Fig. 2.24(a). However, most of vortex or antivortex cores are fragmented. Fig. 2.24(e) shows the schematic of all trimerization and ferroelectric domains. Not that the nature of trimerization antiphase and ferroelectric polarization of all domains is un-ambiguously identified using the $Z_2 \times Z_3$ coloring rules [103].

We propose that the vortex core defragmentation originates from strong domain wall pinning and the high energy cost of charged head-to-head domain walls with the identical

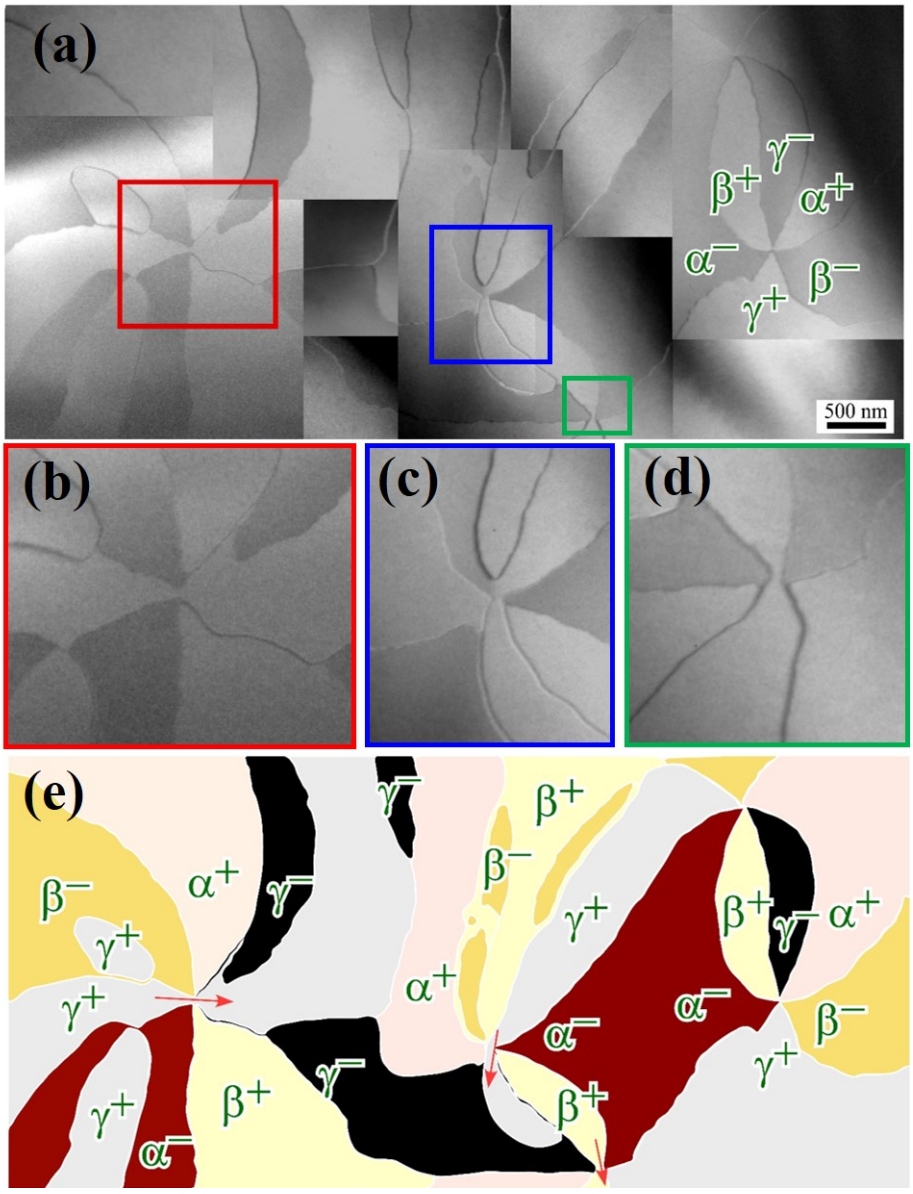

Figure 2.24: **Vortex core fragmentation in *ab* plane of $YbMnO_3$.** (a) A large-range superlattice dark-field TEM image shows vortex core split. (b), (c) and (d) are enlarged images for the red, blue and green boxed regions, respectively. (e) displays the schematic of trimerization and ferroelectric domains.

trimerization antiphase. In Fig. 2.25(a), six domain walls around one vortex core on a crystal surface are shown as blue dashed lines, and inside six domain walls with a tilted vortex core are displayed as red dashed lines. The domains at the surface and inside of the crystal are labeled with black and gray ($\alpha+$, β-, $\gamma+$, α-, $\beta+$, γ-) letters, respectively. This tilted vortex core results in a charged head-to-head domain wall with one trimerization antiphase, as shown in the purple region of Fig. 2.25(a). Fig. 2.25(b) displays a cross-sectional cartoon for the tilted vortex core and the charged head-to-head wall of γ domains. This wall between the top γ- domain and bottom $\gamma+$ domain costs large domain wall energy, and extremely unstable, as evident in the free energy landscape shown in Fig. 2.25(d).

In the Mexican-hat-type energy landscape, the energy barrier between, for example, two neighboring β- and $\alpha+$ domain (black dashed-line) is small, but the energy barrier between γ- and $\gamma+$ domains (pink dashed curve) is much larger[101, 125]. This positively-charged

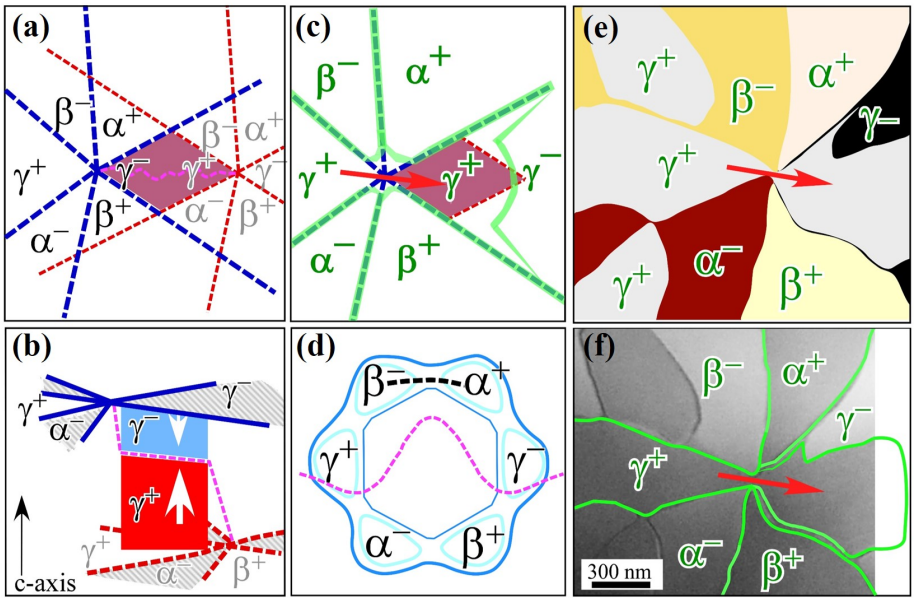

Figure 2.25: **Schematic showing vortex fragmentation.** planar view (a) and side view (b) of a highly tilted vortex core away from the c axis. (c) Schematic diagram showing a vortex core split after removing positively-charged walls of γ domains. Newly-formed domain walls after vortex core split are displayed with the green lines. (d) Mexican-hat-type free energy landscape for six trimerization and ferroelectric phases. (e) Schematic for the red boxed area in Fig. 2.24(a) displays trimerization and ferroelectric phases, vortex core split, and expansion of $\gamma+$ into γ- domains. (f) DF-TEM image shows opposite contrast to Fig. 2.24(b) with identified trimerization and ferroelectric phases.

domain wall between γ- and γ+ domains can be readily removed by upward effective electric field due to oxygen vacancy gradient. As schematically shown in Fig. 2.25(c), this effect combined with strong pinning of domain walls at the surface, probably due to impurities at the surface, results in expansion of γ+ domain to γ- domain region at the surface and also the vortex core split. This scenario is in accordance with our DF-TEM results, as shown in 2.25(e) and (f). Green lines display the newly-formed domain walls after vortex core split.

Note that in most cases of self-poling, we observed the evolution from type-I to type-II domains without any change of vortex cores, which corresponds to vortex core pinning. However, in this particular sample, we suspect that the vortex cores are highly tilted away from the c axis and domain wall pinning is particularly strong at the surface, leading to the vortex core fragmentation.This phenomenon is still an open question for understanding the nature of topological breakdown.

Chapter 3

Manipulation of topological vortices

Understanding and controlling topological defects [126] in ordered states with spontaneously broken symmetries is essential for technological applications of functional materials. A successful demonstration is when a conduction electron passes through the skyrmion, its spin is fully polarized by the spin texture of the skyrmion and resulted in an emergent electromagnetic field, which significantly affects the dynamics of the skyrmions and produces a Magnus force perpendicular to the skyrmion velocity [127–129]. Vortices in superfluid liquids and superconductors are also shown drifting under the influence of the Magnus force in a direction normal to both the supercurrent and vorticity vectors [130]. Moreover, ferromagnetic and ferroelectric memory devices rely on field- and current-induced dynamics of domain walls. Unusual physical properties of topological defects open new ways for their manipulation. The electric polarization induced by chiral magnetic domain walls, for example, was used to shift them with an inhomogeneous electric field [131].

In this chapter we will discuss our work on manipulation of domain, domain walls, and vortex cores in hexagonal manganites, with external electric field and shear strain. We will also shine light on the analogy between vortex in superfluid and multiferroics through the explanation of Magnus-type force.

3.1 Electric field effect on domain walls of vortices

As what we discussed in the electric field poling section, where the electric field change Type-I domain network into Type-II domain network, however, whether the electric poling

affect the vortex, or in other words, whether electric field is able to manipulate the vortex core is still unknown.

The switching dynamic around a vortex is shown in Fig. 3.1 by M. G. Han's group [132]. The switching experiment was done by using DF-TEM, denoted in alphabetical order, and correspondingly illustrated in Fig. 3.1(a) to (m), yellow arrows indicate the polarization direction for each domain. The vortex core is denoted by green dots. Electrostatic charges associated with the domain walls are indicated in red (positive) and blue (negative). The abrupt changes in domain-wall's position from 50 kV/cm to 66.7 kV/cm, from 150 kV/cm to 0 kV/cm, and from 33.3 kV/cm to 50 kV/cm are shown by white arrows. Note that three 0 kV/cm states have similar configurations of the surface domain, indicated by the red circles in In Fig. 3.1(a), (g), and (m). Domains with parallel polarization to the applied electric field expand, while those with antiparallel polarization shrink, as one can predict for

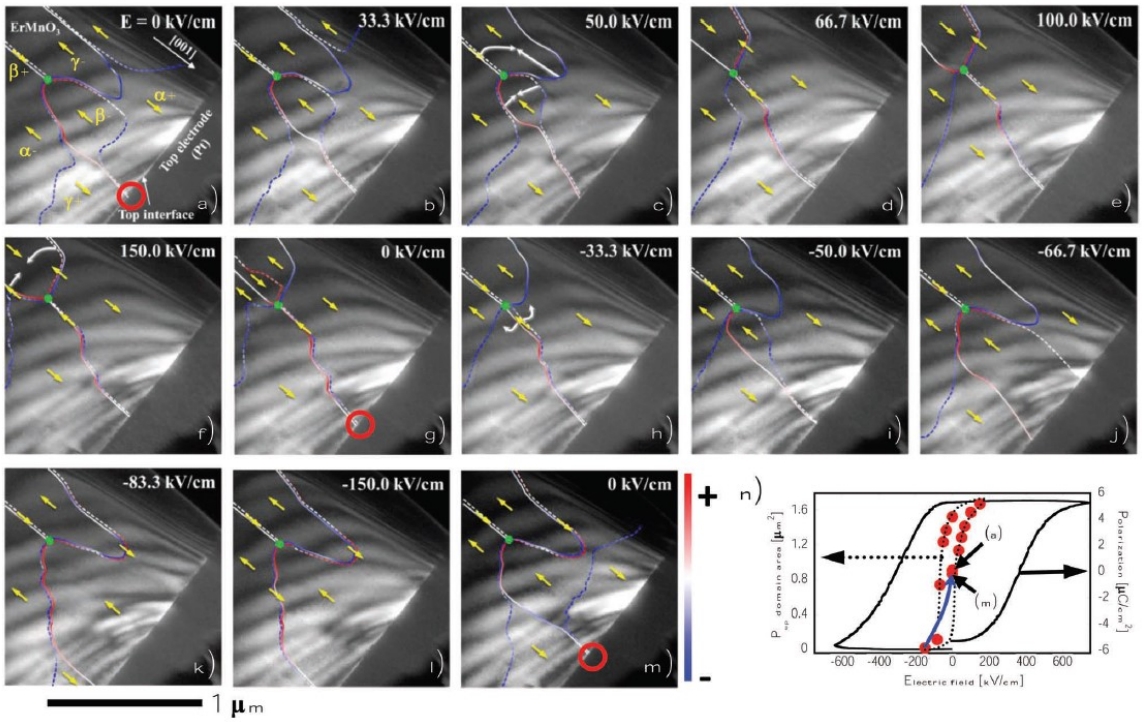

Figure 3.1: **Switching dynamics around a vortex, which is from reference [132]** (a)-(m) are DF-TEM images showing the order of the switching sequence, denoted alphabetically, with an applied field along the [001] direction. (n) is measured P-E loop

typical ferroelectric domain switching. By measuring the area of P_{up} domains (polarization pointing toward the surface of the sample, or along the c-axis), a hysteresis behavior is observed (Fig. 3.1(n)). For comparison, a polarization P electric field E loop electrically measured from a bulk $LuMnO_3$ crystal is shown in Fig. 3.1(n), which shows larger coercive fields.

In fact, it is consistent in that larger field is typically required to achieve a global poling of a bulk $LuMnO_3$ crystal while weaker field is enough to achieve a local poling of a few micron size TEM sample. We note that the three 0 V states (Fig. 3.1(a), (g), and (m)) exhibit a strong preference of P_{up} domains near the surface, which thus suppress the P_{down}-dominant remanent state. It indicates the presence of an internal electric field near the surface, locally lowering the energy of the P_{up} domain with respect to that of P_{down} domain, which also is consistent with the self-poling mechanism.

In Fig. 3.1 , all TEM images show that the vortex cores (marked with a green dot) were fixed during the entire switching process, revealing that its topology protected it. One possible explanation is that: the vortex core where the three up domains and three down domains meet may be electrically neutral and is not influenced by applied electric fields. Moreover, vortex core can be pinned at defects [133] such as oxygen vacancy, and thus becomes immobile.

3.2 Theoretical background for manipulation of vortex core

The project of manipulation of vortex cores are stimulated by Artyukhin *et al.*. Stripes domain are favored and stabilized by an external shear strain [101], which due to the interaction

$$F_{int} = -\lambda \int dV[(u_{xx} - u_{yy})\partial_x \Phi - 2u_{xy}\partial_y \Phi] \tag{3.1}$$

where u_{ij} is the strain tensor and Φ is the phase of the commensurate lattice modulation (trimerization). Equation above is the so-called Lifshitz invariant discussed, in particular,

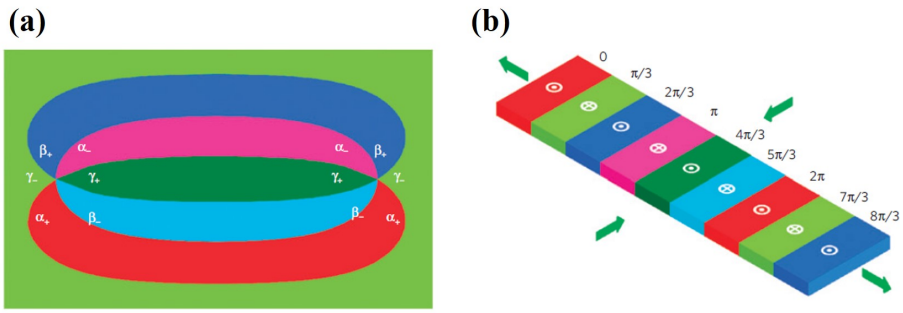

Figure 3.2: **Shear strain generated stripes domain.** (a)shows a pair of vortex and antivortex, (b) displays the topological stripe domain state, the figures are taken from referencee [101]

in the context of commensurate-incommensurate transitions[134]. In the uniform ground state, corresponding to the six degenerate ferroelectric-trimerization states. Shear strain, on the other hand, favors an incommensurate lattice modulation. The compromise is the stripe state – a periodic array of parallel domain walls with Φ monotonically increasing or decreasing by at each wall, as shown in Fig. 3.2. The topological stripe domain state with the alternating polarization (white symbols) along the c axis. A strain indicated by green arrows results in the monotonic increase of Φ in the direction normal to the stripes.

As we discussed in the section of sample growth, when h-$RMnO_3$ crystals are grown below T_c, they exhibit stripe domains of large widths, when a h-$RMnO_3$ crystal with stripe domains is heated above and cooled down across T_c, vortex domains form everywhere in the crystal. However, unaided by external stimuli, this transformation of vortices into stripes has never been directly observed. At the same time, the topological nature of stripe domain states and the direct relationship between stripes and vortices have not been explored.

3.3 Shear strain induced unfolding of vortices into topological stripes

3.3.1 Shear strain on hexagonal manganites crystals

Shear strain was applied on $ErMnO_3$ crystals by putting a weight (alumina rod) on the crystals during a thermal treatment. A schematic cartoon of our strain experiment is

shown in Fig. 3.3(a). A plate-like crystal of h-$ErMnO_3$ was placed across a groove in an alumina plate. An alumina rod was put on the crystal to bend the crystal and provide a downward force. For triangular-shape crystals, the alumina rod was slightly off-centered in the groove direction in a way that there was a larger downward force in the triangular-corner region than in the top-flat region. Fig. 3.3(b) shows the real picture of our strain experimental setup. Note that the alumina rod is placed to be perpendicular to the top-flat edge of plate-like h-$ErMnO_3$ crystals. Fig. 3.3(c) displays a cartoon showing an exaggerated displacement of a triangular-shape crystal under an off-centered alumina rod.

3 different specimen crystals of $ErMnO_3$ (EMO-A, B, and C) with above described experimental setup were slowly cooled across T_c, which is 1130 °C: stayed at 1140 °C for 10 mins, and then slowly cooled to 1100 °C with the rate of 30 °C/h, followed by furnace cooling. Then the specimens are chemically etched for OM observation and AFM scanning.

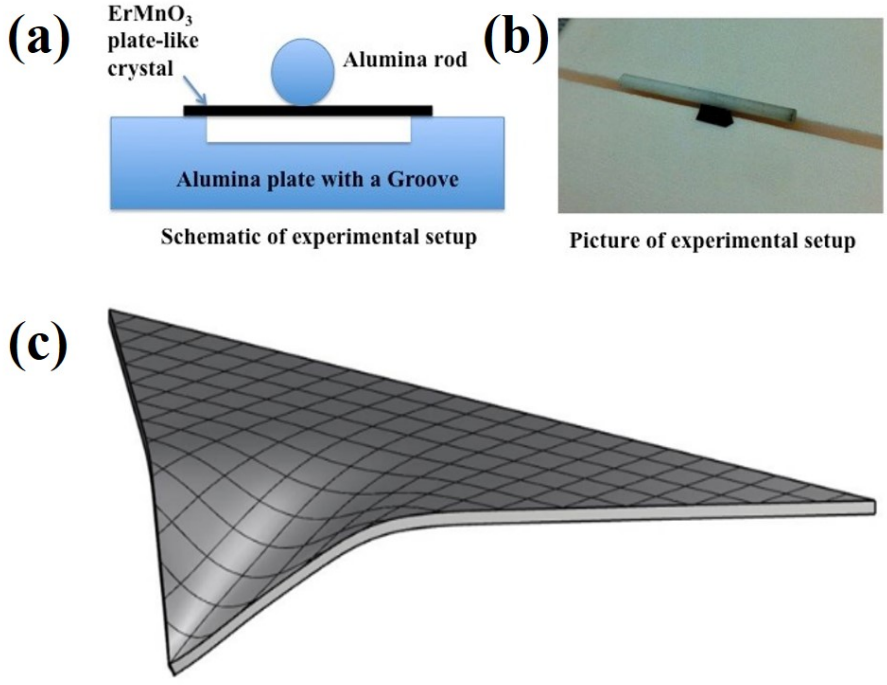

Figure 3.3: **Experimental setup to apply shear strain.** (a) is schematic cartoon depicts a side view of our strain experimental setup. (b) shows the real picture of our strain experimental setup, (c) shows a perspective view of the bending of a triangular-shape crystal under an alumina rod at high temperatures

3.3.2 Experimental results

Fig. 3.4(a) shows a low-magnification OM image of the surface of an $ErMnO_3$ crystal (EMO-A) after applying strain at high temperatures. White dashed lines indicate the position of the alumina rod exerting a downward force on EMO-A. The yellow dashed lines show the location of the edges of the groove in the alumina plate. The tilted dark line between the two white lines indicates where the alumina rod touched the crystal. The rod was off-centered in the vertical direction to make the force in the bottom triangular region larger than in the top region.

Stripe-like domains along the alumina rod direction (perpendicular to the top edge of EMO-A) were observed near the alumina rod, whereas the remaining area showed vortex domains. The vortex-to-stripe transformation takes place near the boundary where vortices meet stripes, as shown in Fig. 3.4(b) which displaying a high-magnification OM image of the green-boxed area in Fig. 3.4(a). Vortices evidently were unfolded and became stripes. The opposite surface of EMO-A exhibits similar domain patterns, as shown in Fig. 3.5. Stripe-type domains along the alumina rod direction were observed near the alumina rod location on both surfaces, and the rest area showed vortex-type domains. Fig. 3.5(c) and (d) are

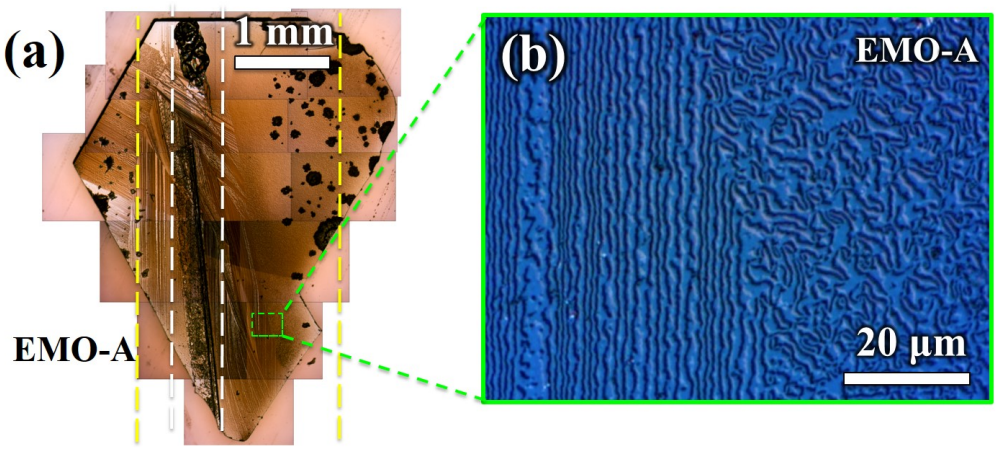

Figure 3.4: **Vortex to stripe transformation.**: (a) is collaged OM image of EMO-A after chemical etching. (b) is Enlarged OM image of the green-box area in (a) showing the vortex-to-stripe transformation.

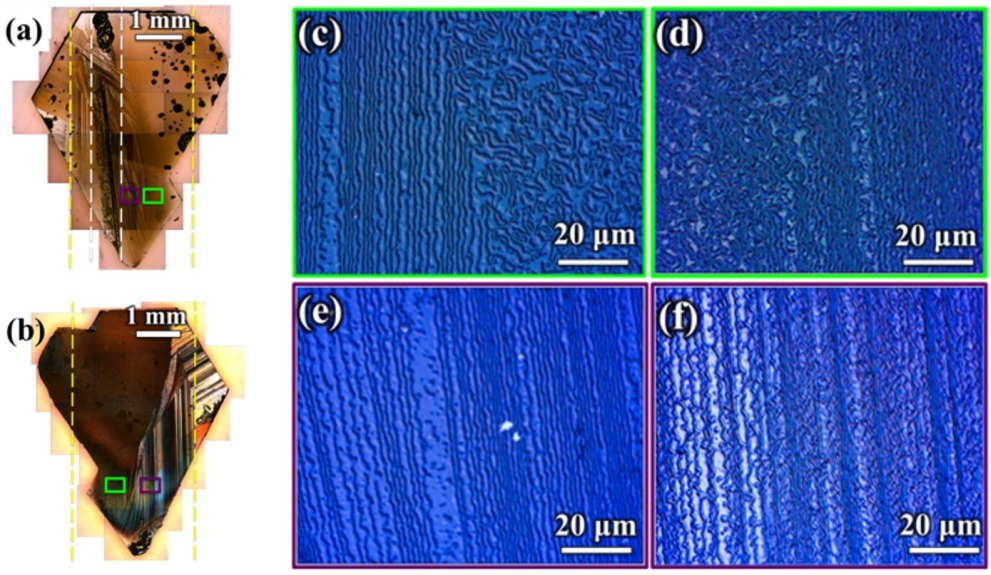

Figure 3.5: **OM images of EMO-A on both surfaces.** (a) and (b) are low magnification OM images of both surfaces of EMO-A. (c) and (d) are OM images of the green-box area in (a) and (b), respectively. (e) and (f) are OM images of stripe domains in the purple-box region, respectively.

high-magnification OM images of the green-box area in Fig. 3.5(a) and (b), respectively, showing the vortex-to-stripe transformation on both surfaces. Fig. 3.5(e) and (f) are high-magnification OM images of stripe domains in the purple-box area in Fig. 3.5(a) and (b), respectively.

In order to clarify the mechanism for the vortex-to-stripe transformation, we performed experiments on two more crystals: another triangular-shaped $ErMnO_3$ (EMO-B) (Fig. 3.6(a)) and the rectangular-shaped $ErMnO_3$ (EMO-C) with an off-centered rod, see Fig. 3.6(b). Surprisingly, EMO-C showed only vortices with no hint of stripes, even in the region right under the alumina rod [see Fig. 3.6(d)], while EMO-B exhibited the vortex-to-stripe transformation, similar to that observed in EMO-A. Evidently, the crystal shape is crucial for the vortex-to-stripe transformation.

Fig. 3.6(e) shows schematically the in-plane strain distribution in triangular-shape and rectangular-shape specimens to illustrate what may be happening in those different-shape crystals (the out-of-plane strain is not shown, as it does not couple to the trimerization

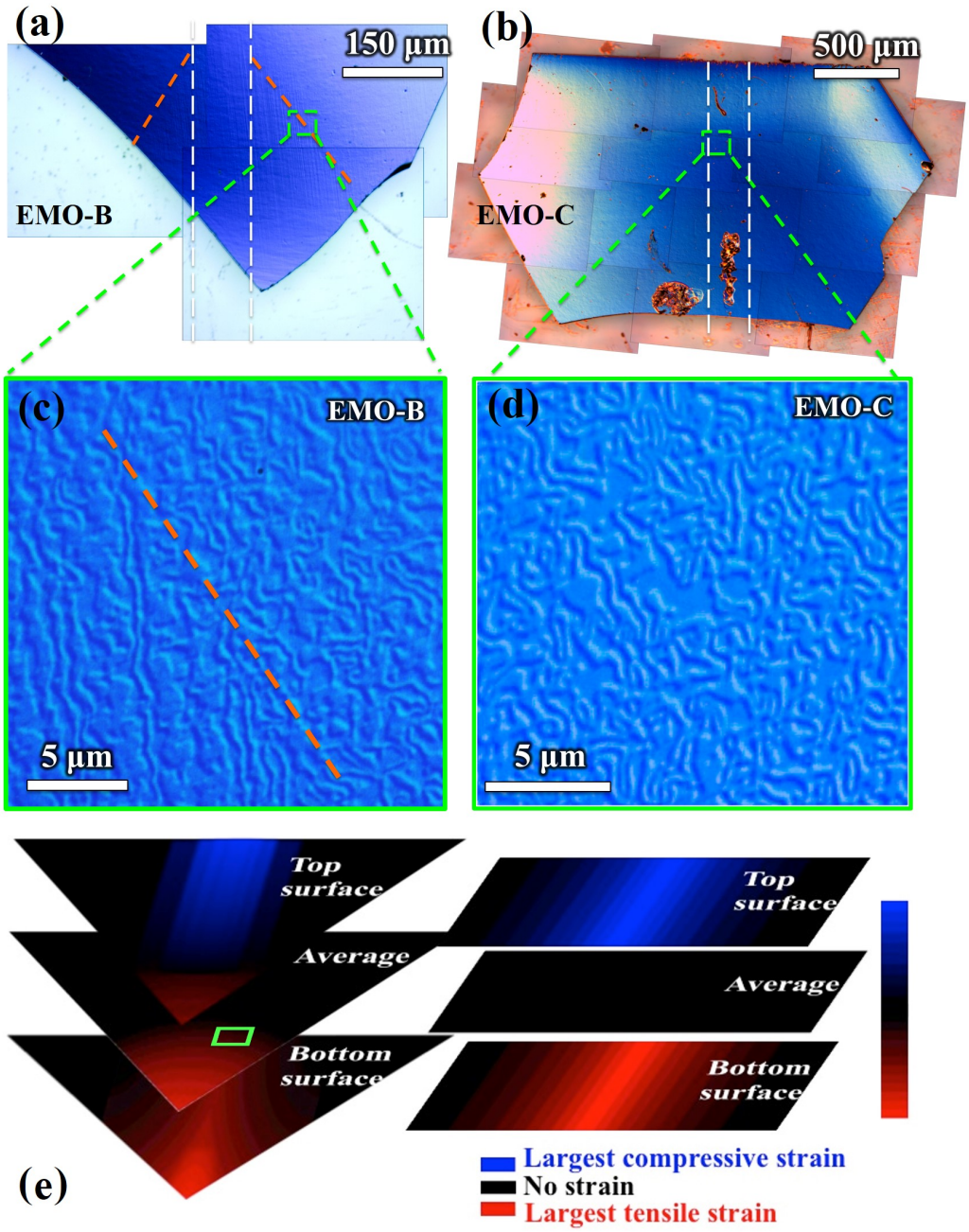

Figure 3.6: **Effect of the crystal shape for annealing under strain (triangle vs. rectangle).** (a)shows OM image of triangular EMO-B (b) is collaged OM image of EMO-C after chemical etching. (c) shows the vortex-to-stripe transformation, and (d) shows only vortices (e) is schematics of in-plane strain on the top surface, average (or middle region), and bottom surface. Blue, red, and black colors indicate compressive, tensile, and no strain, respectively.

phase). In rectangular EMO-C, the top surface is compressed under the weight of the alumina rod, while the bottom surface is stretched. The top compressive and the bottom tensile strains cancel each other on average, i.e. in the middle of the crystal. The triangular corner of EMO-A and EMO-B exposed to an additional strain. To amplify this effect, we intentionally shifted the center of mass of the alumina rod closer to the triangular corner (see Fig. 3.3(c)), which produced an additional shear strain with a large in-plane gradient in the corner. This average shear strain with a large gradient induces the vortex-to-stripe transformation, as discussed below.

AFM scanning images, which exhibit higher spatial resolution than OM images, unveil the details of the vortex-to-stripe transformation. The AFM image of EMO-A in Fig. 3.7(a) corresponds to the optical image in Fig. 3.4(b). The green-boxed area in Fig. 3.7(a) is expanded in Fig. 3.7(b), and the detailed analysis of the purple-boxed area in Fig. 3.7(b) is shown in (c). If we call the defect at the very top of Fig. 3.7(c) a vortex with the sequence of the trimerized phases (α+, β-, γ+, α-, β+, γ-) along a contour in the clockwise direction (red circle), then all cloverleaf defects in Fig. 3.7(c) can be labeled in a consistent manner. The resulting vortices and antivortices are marked with red and blue circles, respectively. The dark (bright) regions in AFM images display valleys (mountain plateaus) corresponding to domains with upward (downward) ferroelectric polarization.

The above analysis reveals several remarkable features: [i] the fixed sequence of the six trimerized phases (...α+, β-, γ+, α-, β+, γ-...) in the stripe region from right to left, [ii] the predominant presence of vortices at the transformation boundary (i.e. the applied strain mostly expels antivortices from the sample). An excess of vortices (red circles, the clockwise (α-, β+, γ-, α+, β-, γ+) sequence) at the vortex-to-stripe transformation boundary results from predominant expulsion of antivortices (dashed blue circles, the anti-clockwise (α-, β+, γ-, α+, β-, γ+) sequence). All domain walls in stripes exhibit the same chirality corresponding to the sequence (α-, β+, γ-, α+, β-, γ+) from right to left in the whole stripe, and [iii] no vortices or antivortices in the stripe domain region (see Fig. 3.4(b) and

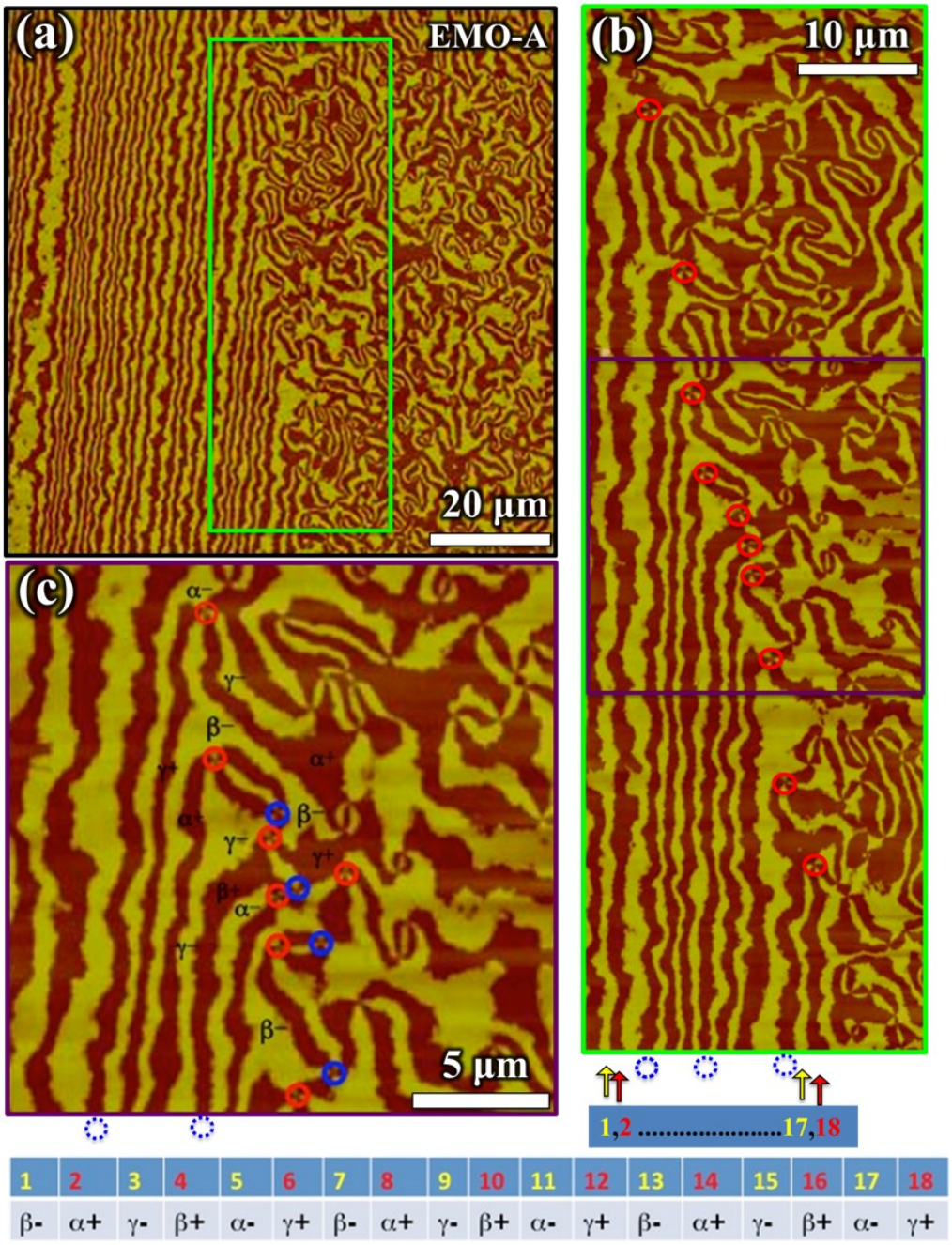

Figure 3.7: **AFM image of the vortex-to-stripe transformation.** (a) Large-range AFM image of the area in Fig. 3.4(b) showing vortex-to-stripe transformation. (b) Fine-scan AFM image of the green-boxed area in Fig. 3.7(a). (c) Expanded AFM image of the purple-box area in Fig. 3.7(b) with the self-consistently assigned trimerization and ferroelectric phases of all vortex and stripe domains.

a larger area shown in Fig. 3.4(a)). These features are consistent with the theory discussed above in Eq. 3.1.

3.3.3 Magnus force

Fig. 3.8 (a) is a schematic for Fig. 3.7(c), and Fig. 3.8(b) is a topologically deformed cartoon of transformation boundary shown in Fig. 3.8(a). Vortices (antivortices) are marked with red (blue) circles. Consider now the change of Φ along a closed yellow contour around the boundary between the topological stripe and the vortex-antivortex domains, as depicted in Fig. 3.8(b). According to Stokes lemma,

$$\oint d\mathbf{x} \cdot \nabla\Phi = 2\pi(N_V - N_A) \tag{3.2}$$

where N_V and N_A are the total numbers of vortices and antivortices inside the contour, respectively. Φ changes monotonically only in the line interval AB, while in the rest of contour Φ changes randomly. Thus, for a sufficiently large integration contour, $\Phi_B - \Phi_A = \frac{\pi}{3}N_{DW} = 2\pi(N_V - N_A)$, N_{DW} being the total number of domain walls in the stripe domain. The excess of vortices is, therefore, related to the number of stripes: one extra vortex per 6 domain walls.

The transformation of a random network of topological defects into the array of parallel stripes involves the separation of vortices from antivortices. A uniform shear strain $u_{xx} - u_{yy}$ favoring stripes along the y-axis applies a force to a domain wall connecting a vortex with an antivortex. Using Eq.3.1, we find that, independent from the shape of the wall, its total interaction energy is $F_{int} = -\frac{h\pi\lambda}{3}(u_{xx} - u_{yy})(y_V - y_A)$, where $y_V(y_A)$ is the y-coordinate of the vortex(antivortex) and h is the sample thickness. Differentiating this energy with respect to y_V and y_A, we obtain the forces that pull the vortex and antivortex away from each other and lead to their unfolding into stripes. This process is illustrated in Figs. 3.8(c) and(d) showing a vortex-antivortex pair. The phase Φ increases in the positive x-direction in the region between the vortex and antivortex, which in the presence of the strain $u_{xx} - u_{yy}$

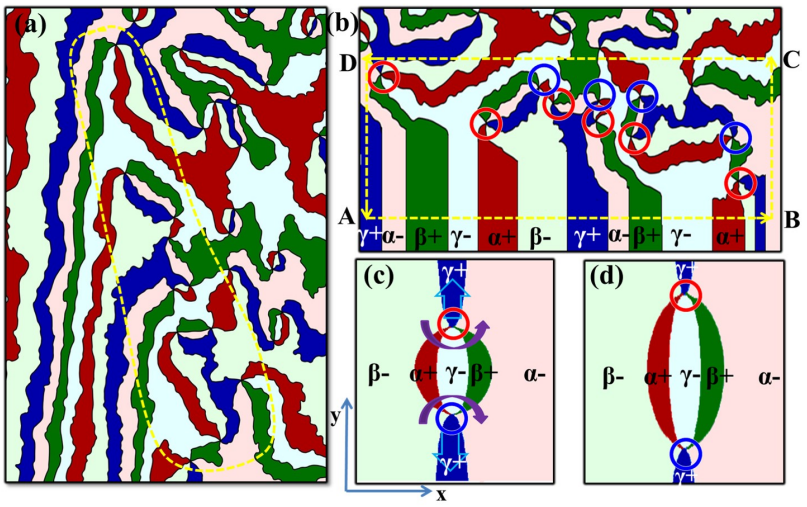

Figure 3.8: **Magnus-type force on vortex-antivortex pair.** (a) A schematic of Fig. 3.7(c). (b) is a topologically deformed cartoon of the boundary between the vortex-antivortex domains (upper part) and the topological stripe domains (lower part). (c) shows vertical forces (light blue arrows) on the vortex and antivortex. Purple arrows indicate the direction of the phase gradient. (d) Vertical stripe domains which are about to form, as the Magnus-type force pulls the vortex and antivortex apart.

lowers F_{int}, whereas above the vortex and below the antivortex the phase gradient has the energetically unfavorable direction. The force pulling the vortex and antivortex apart, $F_y = 2h\pi\lambda(u_{xx} - u_{yy})$, increases the length of the energetically favorable domain walls at the expense of the unfavorable ones.

Fig. 3.9 explains pictorially how a shear strain coupled to the phase gradient by the interaction showing in 3.1 can lead to stripes with monochirality. If we assume that the order of (γ-, β+, α-, γ+, β-, α+ from left to right) is favored by the term $u_{xx}\partial_x\Phi$ in the presence of a horizontal (the x-direction) shear strain, then the domain walls following the purple arrows 2 and 3 have a lower energy then the domain walls following yellow arrows 1 and 4. Then, the upward motion of a vortex and downward motion of antivortex will enlarge the region with lower energy walls and shrink the region with higher energy walls, which will lead to lowering of the total energy. This effect will result in strain-induced Magnus-type force acting on vortices and antivortices in opposite directions.

Therefore, the strain favors the topological stripe domain state with a nonzero average

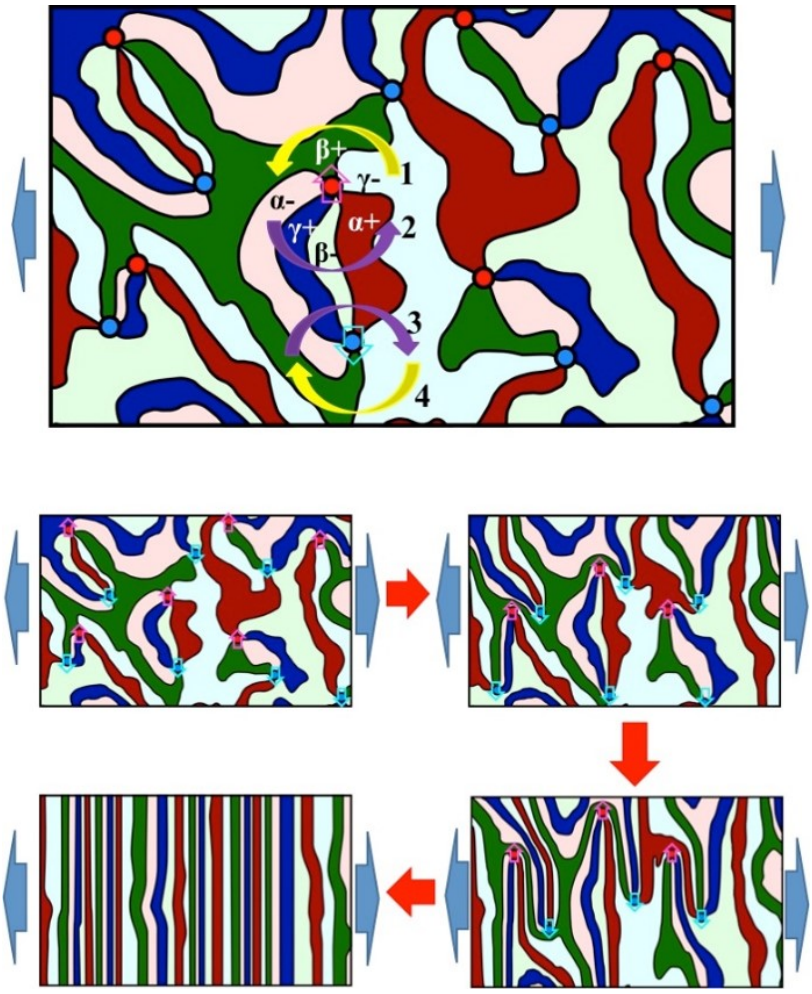

Figure 3.9: **Schematics showing the unfolding process.** The unfolding process of vortices and antivortices intoto mono-chiral stripes induced by horizontal shear strain (large blue arrows). The shear strain induces a Magnus type force (open arrows) acting on vortices (red) and antivortices (sky blue) in opposite directions.

gradient of the phase Φ, which forces vortex and antivortex to move in opposite directions (normal to the shear strain direction). One can draw an analogy between the topological stripe state and a superfluid liquid with a superfluid current proportional to the gradient of the condensate phase. The force on vortices and antivortices in h-$RMnO_3$ generated by strain is analogous to the Magnus force that moves superfluid vortices and antivortices in the direction transverse to the superfluid current, where the supercurrent $\mathbf{j} \propto \nabla\Phi$. The Magnus force in such states pulls vortices away from antivortices in the direction normal to $\mathbf{j}$ (or that of the average phase gradient). This effect is similar to the transverse force in h-$RMnO_3$, the difference being the smooth variation of the condensate phase vs. discontinuous jumps of the phase of the periodic lattice modulation at domain walls in h-$RMnO_3$s.

3.3.4 Strain gradient

If the applied uniform strain pushes all antivortices out of the sample and all vortices towards the transformation boundary, the presence of a much larger excess of vortices is be expected at the boundary, which is not consistent with our observations. Therefore, the transformation of vortices into stripes must involve an additional mechanism, which may be the coupling between vortices(antivortices) and the strain gradient due to the lattice distortion created at the vortex(antivortex) core by six merging domain walls. The resulting force pushes vortices and antivortices in the same direction. This strain-gradient-induced force can expel extra vortices and antivortices from the strained area to the outside of the specimen. This mechanism is consistent with the fact that the stripes are only observed in the regions where the strain is non-uniform.

This force induced by strain gradient can results from expansion/contraction of lattice around vortices described, for example, by the term,

$$F_{int}^{(2)} = g(u_{xx} + u_{yy})(\partial_i Q \partial_i Q + Q^2 \partial_i \Phi \partial_i \Phi) \tag{3.3}$$

where Q is the amplitude of the order parameter (lattice trimerization) and Φ is its phase.

For an inhomogeneous strain $u_{xx}+u_{yy}$ depending on the (x,y) coordinates in the ab-plane, this coupling is effectively a potential energy, $U(x,y)$, of the vortex which, depending on the sign of the coupling constant g, forces the vortex to move into regions with larger or smaller strain.Since $F_{int}^{(2)}$ is independent of sign of the phase gradient, it gives rise to a force that moves vortex and antivortex in the same direction. The result of the two different couplings to strains is the formation of mono-chiral stripes with only a small excess amount of vortices remaining at the transformation boundary. We note that the interaction $F_{int}^{(2)}$ also leads to strain-mediated interactions between vortices, as was discussed in the context of vortex arrays in superconductor [135, 136].

We also note that for the bending deformation caused by the alumina rod, the non-zero components of the strain tensor, u_{xx}, u_{yy}, u_{xy} and u_{zz}, are proportional to the z-coordinate (normal to the surface) and have opposite signs at the upper and lower surfaces of the sample [137]. Such a strain favors stripes with opposite signs of the gradient of the phase Φ at the two surfaces, which are energetically very costly because a nonzero $\oint d\mathbf{x}\cdot\nabla\Phi$ around the sample surface implies the presence of an array of parallel vortex cores inside the sample. This explains why we do not observe stripes in EMO-C.

Both topological and non-topological couplings to strain originate from lattice anharmonicity and are proportional to the second power of the trimerization amplitude Q. The energy of the topological interaction per unit area of the domain wall can be estimated as $u\frac{Q^4}{a^4}Ry$, where u is the strain, a is the lattice constant and Ry is Rydberg constant. Similarly, the energy of the non-topological interaction per unit length of the vortex line is $\sim u\frac{Q^2}{a^3}Ry$. Thus for a vortex displaced by a length L, the ratio of the non-topological and topological interactions is $\sim \frac{a}{L}\frac{(u(L)-u(0))}{u} \ll 1$, since the typical width of the stripe phase is much larger than one lattice constant. Although weak, the coupling to strain gradient can play an important role for kinetics of domain wall and vortices near the phase transition, e.g. by moving crystallographic defects accumulated at vortices and domain walls and hindering their motion.

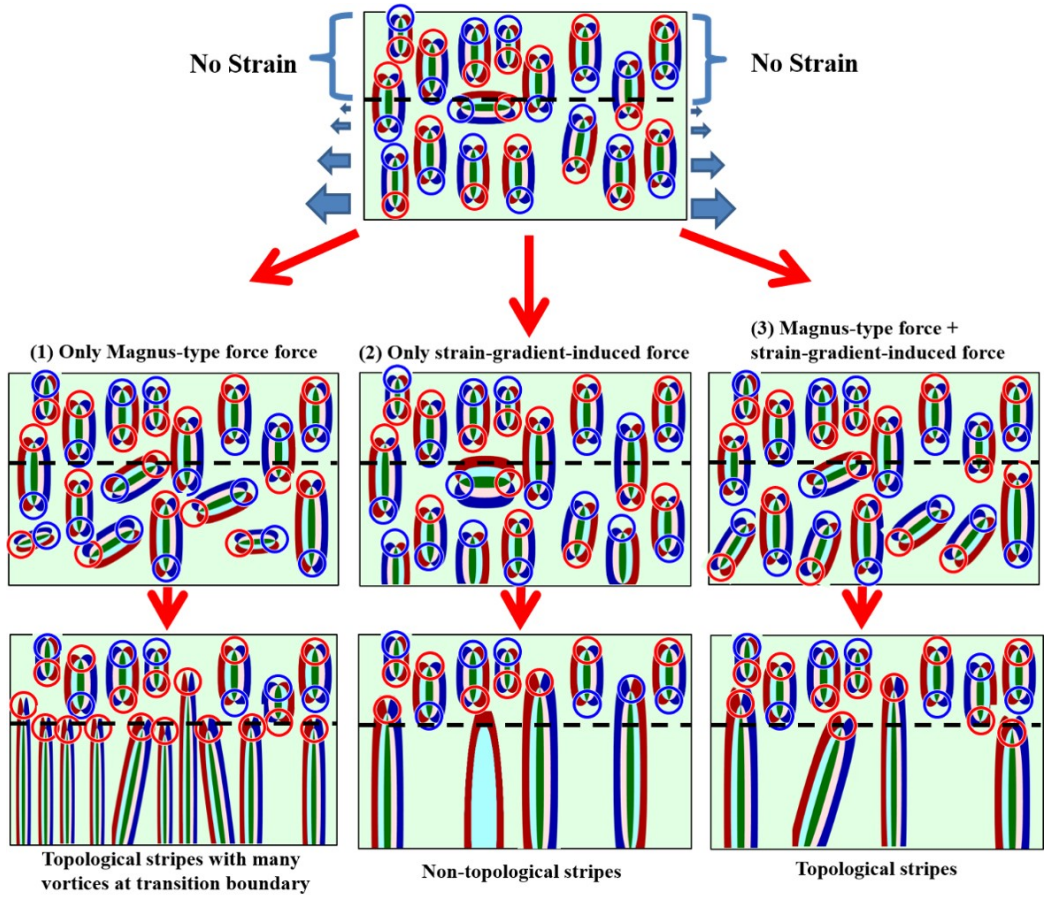

Figure 3.10: **Magnus type + strain gradient induced forces.** (1) only Magnus-type force without strain-gradient-induced force, (2) only strain-gradient-induced force without Magnus-type force, and (3) Magnus-type force plus strain-gradient-induced force.

Fig. 3.10 shows schematic cartoons for a simple situation of having only isolated vortex and antivortex pairs. We start with a random distribution of isolated vortex-antivortex pairs - all colors and labels are identical with what we discussed above, and then we compare 3 different cases with top panels showing beginning stage of a simple situation with randomly-distributed isolated vortex-antivortex pairs. Above the black dashed line, there is no strain, while below the black dashed line, there exists a non-uniform shear strain (blue arrows), which reflects our experimental situation with triangular crystals: (1) only Magnus-type force without strain-gradient-induced force, if only the Magnus-type force is present, topological stripes with a high density of vortices at the vortex-stripe transition boundary are formed, which is inconsistent with our experimental observation (left-bottom two cartoons). (2) only strain-gradient-induced force without Magnus-type force, if only the strain-gradient-induced force is present, the resulting stripes do not follow the sequence of (α+, β-, γ+, α-, β+, γ-) and thus are non-topological (middle-bottom two cartoons) and (3) Magnus-type force plus strain-gradient-induced force (which is consistent with our experimental observation), both Magnus-type force and strain-gradient-induced forces are present, the topological stripes with a smaller number of vortices near the stripe domain boundary are formed, which is consistent with our experimental observation.

From these cartoons, it is clear that if we have only the Magnus-type force, then there should be a large excess of vortices at the vortex-stripe transition boundary, because only antivortices are expelled from the sample, while the relevant vortices accumulate at the transition boundary, and the number of vortices remains the same. If we also take the strain-gradient-induced force into account, then we obtain topological stripes with a smaller number of vortices at the vortex-stripe transition boundary, as is observed experimentally. Note that if we consider only the strain-gradient-induced force (case (2) in Fig. 3.10), then the trimerization phases in the stripes do NOT follow the sequence of (α+, β-, γ+, α-, β+, γ-), which is inconsistent with our experimental observation. Therefore, both the Magnus-type and strain-gradient-induced forces are necessary to explain our experimental

observation, resulting topological stripes.

3.4 Revisit of stripe domains

3.4.1 TEM study of topological stripes

A specimen (EMO-D) for high-angle annular-dark-field scanning transmission electron microscopy (HAADF-STEM) imaging with the detection angles ranging from 68 mrad to 280 mrad was prepared using a focused ion beam lift-out technique on a chemical-etched crystal showing the surface domain structure on the ab plane. HAADF-STEM images were obtained using a JEOL ARM 200 CF equipped with a CEOS Cs-corrector.

The monochirality of stripes is confirmed by atomic-resolution HAADF-STEM images. A scanning electron microscope (SEM) image of the top surface of EMO-D after chemical etching is shown in Fig. 3.11(a): narrow valleys are upward (+) polarization domains. A specimen for HAADF-STEM experiments was obtained cutting out the green-box area in Fig. 3.11(a) with focused-ion beam (FIB) milling, and a dark-field TEM image of the specimen taken with the $(00\bar{4})$ reflection near the [100] projection shown in Fig. 3.11(b) displays the cross-sectional view of domain structures, which are consistent with the SEM image in Fig. 3.11(a). Atomic-scale HAADF-STEM experiments were performed on the domain walls labeled domain wall 1 to 4 (DW1-DW4), and false-colored HAADF-STEM images of Er-ion columns are shown in Fig. 3.11(c). Dark lines are narrow ferroelectric domains with upward polarization which also shown are crystallographic axes and an enlarged image of the red box area.

Kumagai and Spaldin have discussed four different types of domain walls in h-$RMnO_3$, which we label A-D: the A and B types have undistorted R ions at the walls, and the C and D types do not have undistorted R ions at the walls [125]. The results of our HAADF-STEM experiments lead to two important findings: stripe domains are indeed monochiral (i.e. (α-, β+, γ-, α+, β-) along one direction), and domain walls alternate between the A

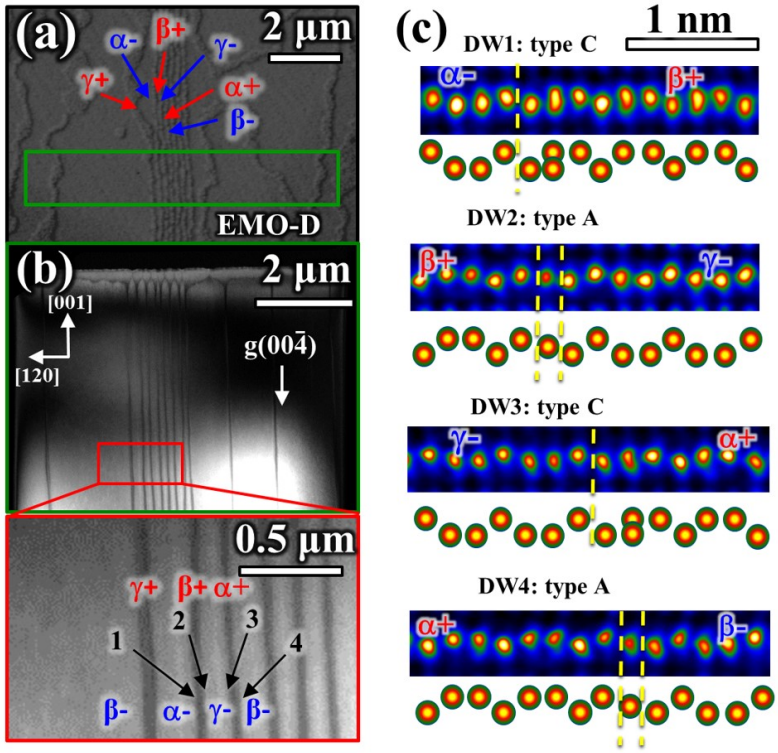

Figure 3.11: **STEM-HAADF analysis of different types of domain walls.** (a)shows SEM image of EMO-D *ab*-plane surface. (b) is DF-TEM image of a STEM-HAADF specimen. (c) False-colored STEM-HAADF images of 1-4 domain walls in the inset of Fig. 3.11(b).

and C types. Although the sampling region in atomic-scale HAADF-STEM experiments is rather small, these results are fully consistent with our results discussed earlier.

According to Ref. [125], the lowest energy wall is of C type. The adjacent parallel walls must then be of either A type or D type. Consistently, we find the alternation of A and C type walls. This result suggests that the domain walls around a vortex core probably exhibit the alternation of B and C types, as shown in Fig. 3.12, which is an AFM image showing a vortex-to-stripe transformation and the corresponding schematic with colored trimerization-ferroelectric phases. Red, blue, and green colors represent three different types of trimerization antiphase (α, β, γ) and dark and light colors indicate ferroelectric polarization directions (up and down, respectively). Local ionic distortions corresponding to the yellow- and light-blue-box areas are depicted in Fig. 3.12(c) and (d), respectively.

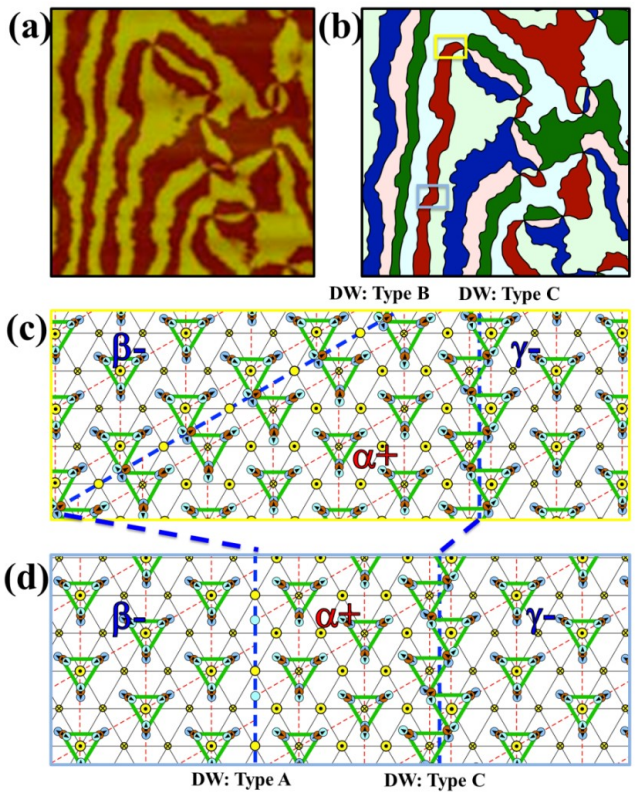

Figure 3.12: **Local ionic distortions for a vortex-to-stripe transformation.** (a) AFM image showing a vortex-to-stripe transformation. (b) Schematic cartoon corresponding to Fig. 3.12(a). (c) and (d) depict local ionic distortions corresponding to the yellow-and light blue-box areas, respectively.

Blue dashed lines indicate connected domain walls from vortex to stripe domains. In this schematic, the B type domain wall between [β-, α+] near the vortex core switches to A type in the stripe area, while the C type domain wall between [α+, γ-] remains unchanged. Note that B type and C type walls exist at an angle with 60 degrees, and A type and C type walls are parallel to each other.

3.4.2 Non-topological stripes in as grown $YMnO_3$

In as grown $YMnO_3$ crystals, we also find at the edge of crystal, vortices are unfolded to stripes [103], which is most likely due to the natural strain during the flux crystal growth.

During flux crystal growth, many crystals are randomly stuck together to form a chunk (see 2.2, and those crystals in a chunk tend to provide significant mutual strain, especially

near crystal edges, when the crystal chunk is cooled right after flux crystal growth. The anisotropic thermal contraction of $YMnO_3$ probably plays the key role for this mutual strain in a crystal chunk. This mutual strain sometimes does result in stripes near crystal edges of as-grown $YMnO_3$ crystals, which otherwise exhibit vortex domains. Note that this can happen only in as-grown $h-YMnO_3$ among all as-grown h-$RMnO_3$, since only T_c of $YMnO_3$ is lower than the flux crystal growth temperature (if T_c is higher than the flux crystal growth temperature, then domains in as-grown crystals are stripe-type everywhere).

The stripes induced by the mutual strain during the flux crystal growth process is not mono-chiral (i.e. not topological), which is probably due to the random nature of the mutual strain. For example, in one image in the reference [103], we have identified all vortices(antivortices) near the vortex-stripe transition boundary and all vortices(antivortices) removed away from a crystal edge, as shown in Fig. 3.13. Red circles are vortices, blue circles are antivortices, and dashed circles represent expelled vortices or antivortices. As evident in Fig. 3.13, both vortices and antivortices exist at the vortex-stripe transition boundary, and the expelled ones can be either vortices or antivortices in different regions in a random manner. Therefore, the stripes are not topological (i.e., not mono-chiral).

This random nature probably originates from the random distribution of mutual strain

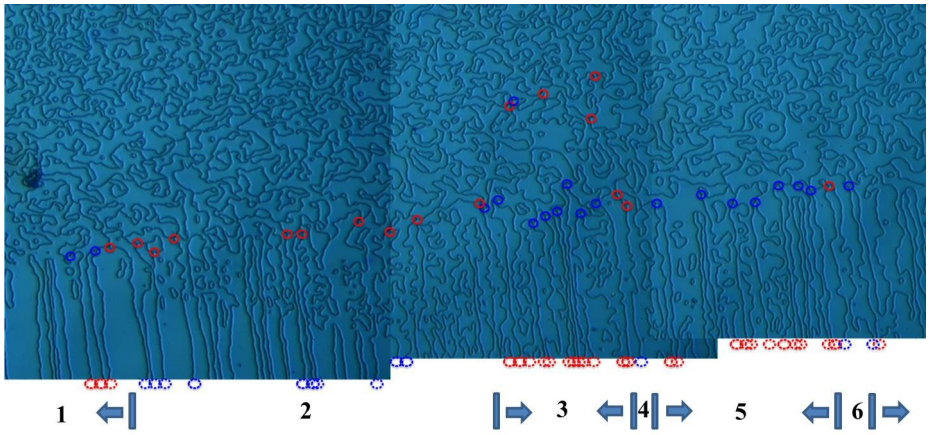

Figure 3.13: **Non-topological stripes.** Stripes in the entire region do not maintain mono-chirality.

near the edge of a crystal in a chunk, where many crystals are embedded randomly, during the cooling process after flux crystal growth. Note that the nature of in-plane strain (compressive vs. tensile) determines the chirality of stripes, due to the $u_{xx}\partial_x\Phi$ term in the free energy. Consequently, if regions 1, 3, 5 are associated with compressive strain, then regions 2, 4, 6 should be associated with tensile strain, and the stripe chirality changes at the boundary between different regions. Thus, if tensile-strain regions are associated with expelled antivortices, then vortices are expelled in compressive-strain regions.

Furthermore, even if an as-grown $YMnO_3$ crystal does exhibit stripes near a crystal edge, it shows uniformly-random vortex domains when it is individually annealed across T_c (i.e., it is removed from a crystal chunk, and then annealed across T_c), as shown in Fig. 3.14. (a) as-grown $YMnO_3$ crystal showing a vortex-stripe transition boundary in flux-grown crystals. (b)shos when the crystal in (a) is annealed across T_c without strain, uniformly-random vortices appear everywhere, including in the original stripe region. The bottom panel is an expanded view of the purple-boxed region in the top panel, and the AFM image in the inset shows the vortices in the green-boxed region.

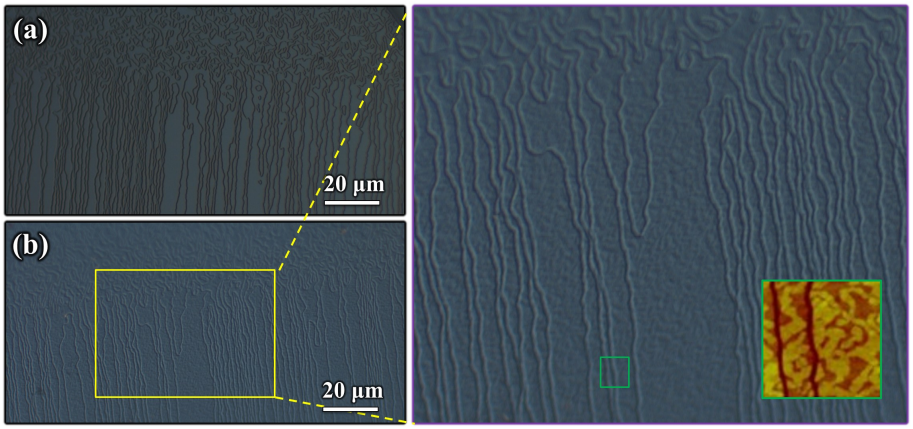

Figure 3.14: **Re-annealing of stripes on $YMnO_3$.**

Chapter 4

From multiferroics to cosmology

Symmetry breaking leads to the birth of our universe in the study of cosmology as well as the symmetry determined properties in material science. On one hand, it has been speculated that, in the hot early universe, the vacuum possessed a large number of symmetries. As the universe expanded and cooled, the vacuum underwent a series of symmetry-breaking phase transitions. For example, the electro weak transition broke the $SU(2) \times U(1)$ symmetry of the electro weak field into the $U(1)$ symmetry of the electromagnetic field. This transition is important for understanding the asymmetry between the amount of matter and antimatter in the present-day universe. On the other hand, symmetry breaking in the materials gives rise to a variety of interesting phenomena like multiferroicity, the magnetoelectric effect, ferrotoroidicity, polar superconductivity, magnetic monopoles, and skyrmions. It seems that 2 completely independent subject areas are actually connected to each other by the concept of symmetry breaking and phase transition.

The theory bring the study of cosmology into the condensed matter physics lab is called Kibble-Zurek Mechanism (KZM), which describes the associated non-equilibrium dynamics and to estimate the density of defects as a function of the quench rate through the transition. As we discussed, the formation of topological defects happens during the phase transition not even in cosmology but also in materials. In the course of a non-equilibrium continuous phase transition, the dynamics ceases to be adiabatic in the vicinity of the critical point as a result of the critical slowing down (the divergence of the relaxation time in the neighborhood of the critical point). This enforces a local choice of the broken symmetry and can lead to the formation of topological defects.

In this chapter, we will start from introducing KZM and relative concepts like winding numbers, then we apply KZM to the study of topological vortices in hexagonal manganites, which turns out that there is emergent continuous phase transition when temperature approaches the critical temperature. Moreover, the frozen of topological vortices can also be described as the condensation of disorder field as we will discuss following.

4.1 Kibble-Zurek Mechanism (KZM)

KZM is named after Tom Kibble [11], who first proposed the formation of the domain structure in the early universe in cosmology. In the reference [11, 138], Kibble pointed out that the universe can be correctly described by a theory showing a phase transition at a critical temperature. Then after a few years, Zurek [139, 140] developed similar ideas in condensed matter physics which provides us a new path to study the phase transition as well as the critical behavior in condensed matter physics. KZM describes the non-equilibrium dynamic and the formation of topological defects through a continuous phase transition. Topological defects are measurable in the experimental condensed matter physics, so the KZM, which at first is trying to study the early universe in cosmology can be potentially tested and proved in condensed matter physics.

4.1.1 Brief introduction of KZM

The main difference between the cosmological and laboratory settings is that the relaxation time and coherence length (and speed of the relevant sound rather than the speed of light) determine the sonic horizon – the linear size $\hat{\xi}$ of regions that can break symmetry in step. The basic idea [139] is to compare the relaxation time τ with the timescale of change of the key parameter (here, relative temperature $\varepsilon = (T - T_c)/T_c$). We assume $\varepsilon(t)$=t/τ_Q , where τ_Q is the quench time. The relaxation time $\tau(\varepsilon) = \tau_0/|\varepsilon|^{\nu z}$ (where ν and z are spatial and dynamical critical exponents, and τ_0 is a timescale set by microphysics) determines the reaction time of the order parameter. Relaxation characterized by $\tau(\varepsilon)$ is faster than

$|\varepsilon/\dot{\varepsilon}| = t$ outside interval $\hat{t} = (\tau_0 {\tau_Q}^{z\nu})^{1/(1+z\nu)}$ around the transition, so the system can quasi-adiabatically follow the change imposed by the quench. This instant is determined by the equation [139]:

$$\tau(\varepsilon(\hat{t})) = |\varepsilon/\dot{\varepsilon}| = \hat{t} \tag{4.1}$$

The system will cease to keep up with the imposed change at time $\hat{t}$ before reaching the critical point, while its reflexes are recovered at time $\hat{t}$ (that is, when $\hat{\varepsilon} = (\tau_0/\tau_Q)^{1/(1+z\nu)}$) after the transition. Thus, broken symmetry is chosen by fluctuations when their coherence length is [139]:

$$\hat{\xi} = \frac{\xi_0}{|\hat{\varepsilon}|} = \xi_0(\tau_Q/\tau_0)^{1/(1+z\nu)} \tag{4.2}$$

The above estimate of the $\hat{\xi}$ is often recast as an estimate for the resulting density of topological defects,

$$n \sim \frac{\hat{\xi}^d}{\hat{\xi}^D} = \frac{1}{\xi_0^{D-d}}(\frac{\tau_o}{\tau_Q})^{(D-d)\frac{\nu}{1+z\nu}} \tag{4.3}$$

where D and d are the dimensions of the space and of the defects (e.g., D = 3 and d = 1 for vortex lines in a 3D superfluid). Thus, if one were able to check the power law above, one could claim that the KZM holds and show that the non-equilibrium dynamics across the phase transition is also universal. This requires the ability to measure the average number of excitations after driving the system at a given quench rate, and repeating this measurement for different quench rates.

The choice of broken symmetry is random within fluctuating domains of this size. Topological defects are then expected to form with the density of one defect fragment per domain. Thus, the scaling of $\hat{\xi}$ with quench rate set by the universality class of the transition translates into the scaling of the defect density. This prediction has been verified for the 3D XY model.

4.1.2 Dependence of vortices density on cooling rate

Is hexagonal manganites system a potential test bed for KZM?

In hexagonal manganites, as we discussed in the chapter about origin of ferroelectricity, the first-principles calculations show that the energy lowering provided by the condensation of the K_3 mode is independent of the angle of the tilt until the polar mode subsequently develops. This observation means below the phase-transition temperature, the potential energy is given by the continuous Mexican-hat form, see Fig. 2.7. The atomic nature of the lattice does not manifest itself until at lower temperatures when the domain structure is already determined. So the full rotational symmetry is broken when the polyhedrons tilt in the 2π range of angles, resulting in a $U(1)$ vacuum. So the dynamics of symmetry breaking in phase transitions is another fascinating phenomenon that can be tested in h-$RMnO_3$.

Because phase transitions are ubiquitous, their dynamics can be investigated experimentally. Although relativistic causality is no longer a useful constraint in the laboratory, cosmological motivations can be combined with the scaling relations in the near-critical regime of second order phase transitions to estimate the density of topological defects as a function of the quench rate [139].

As we discussed in the section of stripes vs. vortices, if we heat up the specimen cross the T_c, the network of vortices is spanning the entire crystal surface, they are conserved with various thermal treatments. In order to test how the density varies as changing the cooling rate cross the T_c, annealing experiments have been carried out on 2 different sets of $RMnO_3$: $ErMnO_3$ [91] and $TmMnO_3$ [66].

For the $ErMnO_3$ case, the cooling rate near T_c was changed from 0.5 °C/h to 300 °C/h, followed by quenching to room temperature. As shown in Fig. 4.1 (a), (b) and (c), they are AFM images of etched $ErMnO_3$ crystals with cooling rate (a) cooled from 1220 °C to 890 °C with rate of 0.5 °C/h, followed by furnace cooling, (b) cooled from 1200 °C to room temperature with rate of 5 °C/h, (c) from 1200 °C to room temperature with rate of 300 °C/h. With the large variation of cooling rate, vortex(antivortex) domain patterns remain

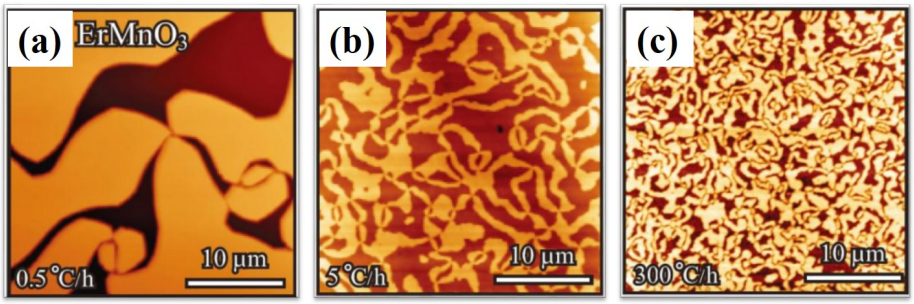

Figure 4.1: **Evolution of vortices with varying cooling rate in $ErMnO_3$.** The AFM images of chemically etched $ErMnO_3$ crystals.

intact, but the density of vortices changes drastically.

For the $TmMnO_3$ case, a series of annealing with different cooling rates have been done: 2, 20, 200, 1000 and 12000 °C/h. Optical images of 4 of them are shown in Fig. 4.2.

To simulate this "density variation depends on the cooling rate" phenomenon, we ran Monte Carlo (MC) simulations of equation

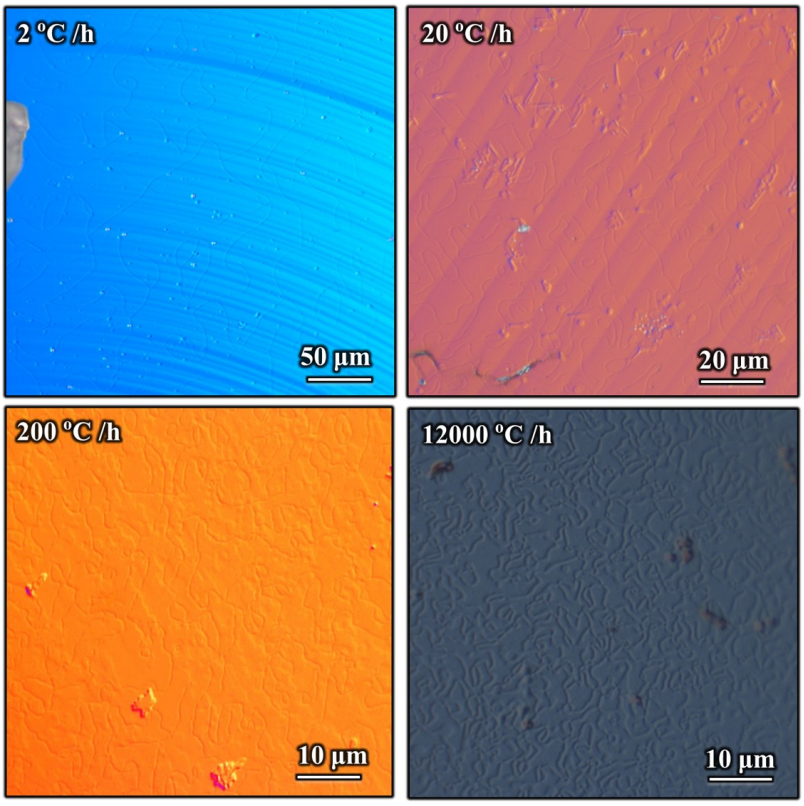

Figure 4.2: **Evolution of vortices with varying cooling rate in $TmMnO_3$.** The OM images of chemically etched $TmMnO_3$ crystals with 4 different cooling rate.

$$\mathcal{H} = J \sum_{\langle j,l \rangle} \cos\left(\phi_j - \phi_l\right) + J' \sum_{\langle\langle j,l \rangle\rangle} \cos\left(\phi_j - \phi_l\right), \tag{4.4}$$

which is an effective $p = 6$ clock model. The simulation is based on a local update Metropolis algorithm because the microscopic dynamics of $RMnO_3$ is expected to be local. The system undergoes a continuous phase transition in the 3D XY universality class. The phase $\phi_j = n2\pi/6$ takes six possible values when the integer n runs between 0 and 5. The electric polarization $\mathbf{P}_j$ is perpendicular to the triangular layers and $P_j \propto \cos 3\phi$. The trimerization order parameter is described by a 2D vector $\mathbf{T}_j \propto (\cos 2\phi_j, \sin 2\phi_j)$. The three possible orientations of this vector will be denoted by (α, β, γ). J and J' are effective coupling constants between nearest-neighbor variables j, l on the same triangular layer ($\langle j, l \rangle$) and on adjacent layers ($\langle\langle j, l \rangle\rangle$), respectively. The lattice size is $L^2 \times L_z$ with $L = 192$ and $L_z = 96$ and we use periodic boundary conditions in the xy plane and open boundary condition along the z direction. The critical temperature obtained for $J' = J$ is $T_c \simeq 3.03J$.

The experimental results and theoretical simulations are shown in Fig. 4.3. Fig. 4.3(a) shows Experimental vortex density in the final state as a function of the cooling rate. The vortex density as a function of cooling rate is consistent with a power law dependence with

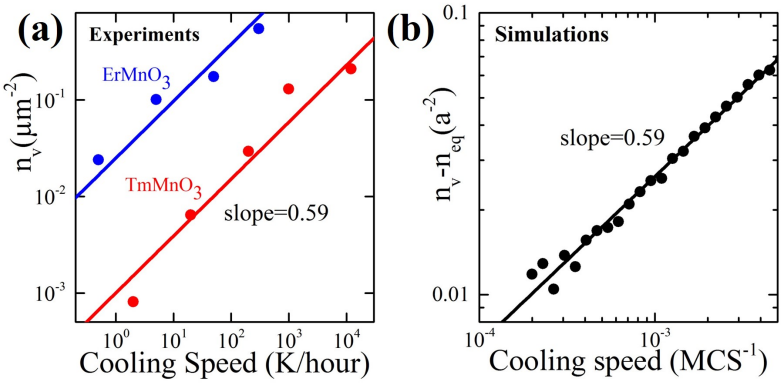

Figure 4.3: **Dependence of vortex density on cooling rate.** (a) is experimental vortex density in the final state as a function of the cooling rate. In (b), the cooling speed is given in inverse MC sweep, n_{eq} is the density of the thermally excited vortices subtracted to reveal the KZM scaling

exponent 0.59 (full lines), that is obtained from our MC simulations shown in Fig. 4.3(b) for a final temperature of 0.92 T_c (black dots), as well as with the prediction of ∼0.57 that follows from the KZM. Our experimental results for $RMnO_3$, as well as our simulations confirm this prediction and corroborate KZM.

The obtained exponent of ∼0.59 is very close to the value $\frac{2\nu}{1+z\nu} \cong 0.57$ that is expected for a 3D XY fixed point: $\nu = 0.67155(27)$ [141] and $z \cong 2$ [142]. We emphasize that the 3D XY fixed point is a consequence of the Z_6 symmetry of $RMnO_3$ compounds (the Z_6 anisotropy is dangerously irrelevant at $T = T_c$ [143, 144]).

By using the above estimate of one $\hat{\xi}$ defect fragment per volume of the domain of that linear size, one can estimate the defect density as a function of quench rate and of τ_0 and ξ_0 - 2D constants that characterize the system - and its universality class given by the spatial and dynamical critical exponents ν and z.

Moreover, reference [102] observed an unexpected phenomenon, as shown in Fig. 4.4 the increase in the rate of much faster quenches (with cooling rates of up to 102K/s) suppressed defect production, resulting in increasing size of domain sizes structures. The red triangles data is from ref. [91] and blue circles are from [102]. This has not been yet explained and texted, although several possibly relevant effects have been discussed. At present, it seems reasonable to wait for experimental confirmation of this anti-KZM effect before attempting to advance a detailed theory.

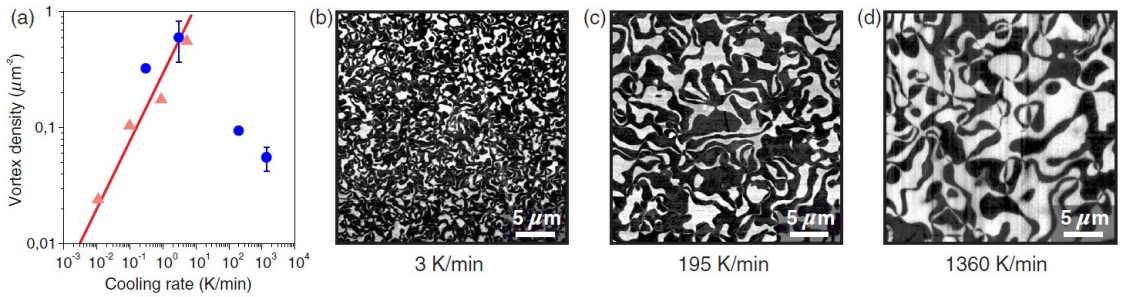

Figure 4.4: **"Anti-Kibble Zurek" mechanism in $YMnO_3$, which is from reference [102]** Vortex-core density as a function of cooling rate for slow cooling (red triangles) and fast cooling (blue circles). (b)(d) show PFM images on $YMnO_3$ with different cooling rate as labeled.

4.2 Winding number

Symmetry-breaking phase transitions yields a formation of topological defects in a seemingly random distribution. Winding numbers are defined to see the randomness of distribution of topological defects. We can define the winding number using the polar coordinate system. Assuming If we draw a enclosed loop which does not pass through the origin, we can write the equation in polar form: $r = r(t) \quad \text{and} \quad \theta = \theta(t)$ where $0 \leq t \leq 1$. The functions $r(t)$ and $\theta(t)$ are required to be continuous, with $r > 0$. Because the initial and final positions are the same, $\theta(0)$ and $\theta(1)$ must differ by an integer multiple of 2π, see Fig. 4.5. This integer is the winding number:

$$\text{winding number} = \frac{\theta(1) - \theta(0)}{2\pi} \tag{4.5}$$

In condensed matter, $\theta(t)$ can be defined as changing of order parameter field, take magnetic spin as an example: The winding number is the total variation of the magnetization angle $\Delta\theta$ as one moves counterclockwise around a circle, divided by 2π, see examples [145] in Fig. 4.6(a). Note that one cannot deform a given spin configuration into another of different winding number. A topological defect exists if one cannot deform a spin configuration into the ferromagnetic state. Following this definition, a pair of magnetic vortex and antivortex apparently can be defined with winding number equal to 1 or -1, see Fig. 4.6(b).

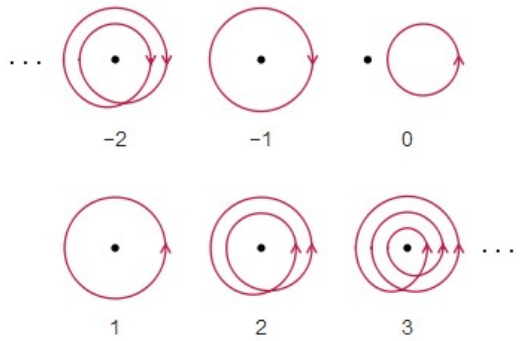

Figure 4.5: **Mathematical definition of winding number.** Image is taken from wikipedia / Winding number

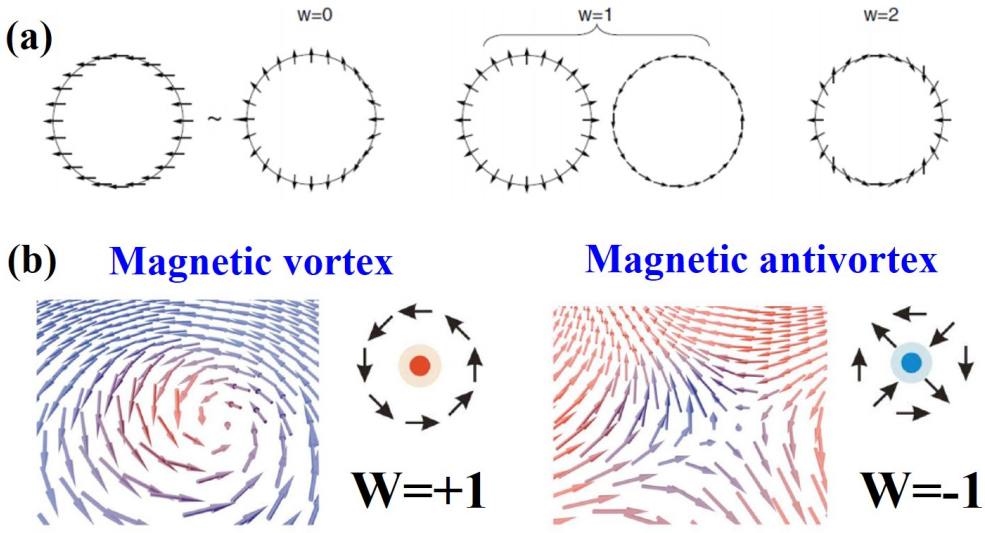

Figure 4.6: **Winding number of magnetic spins.** (a) shows the examples of winding number = 0, 1, 2. Images are from reference [145] (b shows magnetic vortex and antivortex and the corresponding winding numbers (Courtesy of Prof. Sang-Wook Cheong)

Similarly, we can also define ferroelectric vortex in the identical way, with the total variation is trimerization phase instead of magnetization angle. See Fig. 4.7.

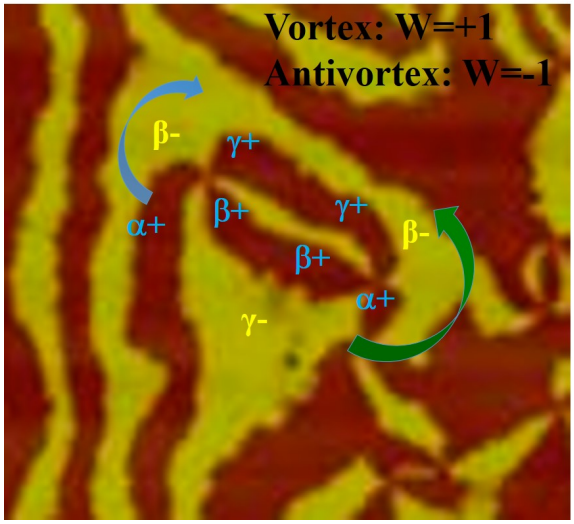

Figure 4.7: **Winding number of ferroelectric vortex and antivortex.**

4.2.1 Winding number from a random distribution of vortex-antivortex pairs

The essence of KZM is the randomness of the choices of broken symmetry in domains of size $\hat{\xi}$. This randomness - in addition to defect density - predicts [139] scaling of the winding number W subtended by a contour C. The winding number is the net topological charge: $W = n_+ - n_-$, the difference of the numbers n_+ and n_- of vortices and antivortices inside C. If these charges were assigned at random, typical net charge would be proportional to the square root of their total number, $n = n_+ + n_-$, inside C, so it would scale as a square root of the area A inside C. Therefore, for contours of a fixed shape, it would scale as the length of the contour, $W \propto \sqrt{A} \propto C$.

According to the KZM, W is set by the winding of the phase along C. In our clock model, broken symmetry phases correspond to even hours on the clock face. W is then the number of days elapsed along the contour C. As choices of even hours (phases) are random in $\hat{\xi}$-sized domains, the typical net winding number W scales as $\sqrt{\frac{C}{\hat{\xi}}}$ it is proportional to the square root of the number of steps. It can be easily understood in the following way: since in hexagonal manganites, one vortex must be paired with another antivortex, so we

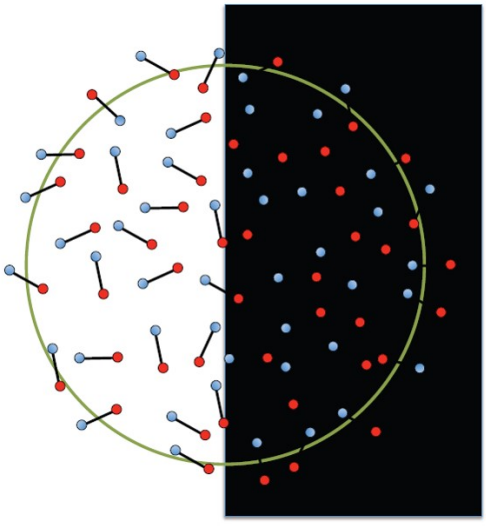

Figure 4.8: **Winding number of pairs of vortices and antivortices.** Winding number for the pairs completely outside the loop or inside the loop are cancelled out. Only the pairs straddle the loop gives the contribution. Figure is taken from reference [140]

can consider the red dots as vortices and blue dots as antivortices (See Fig.4.8 [140]), and the black bar connecting them can be consider as a vortex antivortex pair. It is rather clear that the winding number for the pairs completely outside the loop or inside the loop are cancelled out. Only the pairs straddle the loop gives the contribution. So this can be consider a random walk question along the contour, which gives the typical winding number (characterized either by the average absolute value $|W|$ or the dispersion $\sqrt{\langle W^2 \rangle}$)) indeed scales like $\sqrt{C/\hat{\xi}}$, as long as $C > \hat{\xi}$.

This scaling dependence changes when the magnitude of W falls below 1. Moreover, the scalings of $\langle |W| \rangle$ and of the dispersion $\sqrt{\langle W^2 \rangle}$ diverge in this regime. This may seem surprising, but it is actually predicted by the KZM [146]: $|W| < 1$ occurs when $C < \hat{\xi}$, i.e., C normally contains a single defect or none. In this case $\langle |W| \rangle \approx p_+ + p_- = p_{DEFECT}$, while $\sqrt{\langle W^2 \rangle} = \sqrt{p_{DEFECT}}$ in terms of probabilities. Moreover, the probability p_{DEFECT} of finding a defect inside C is proportional to area A subtended by C, accounting for both

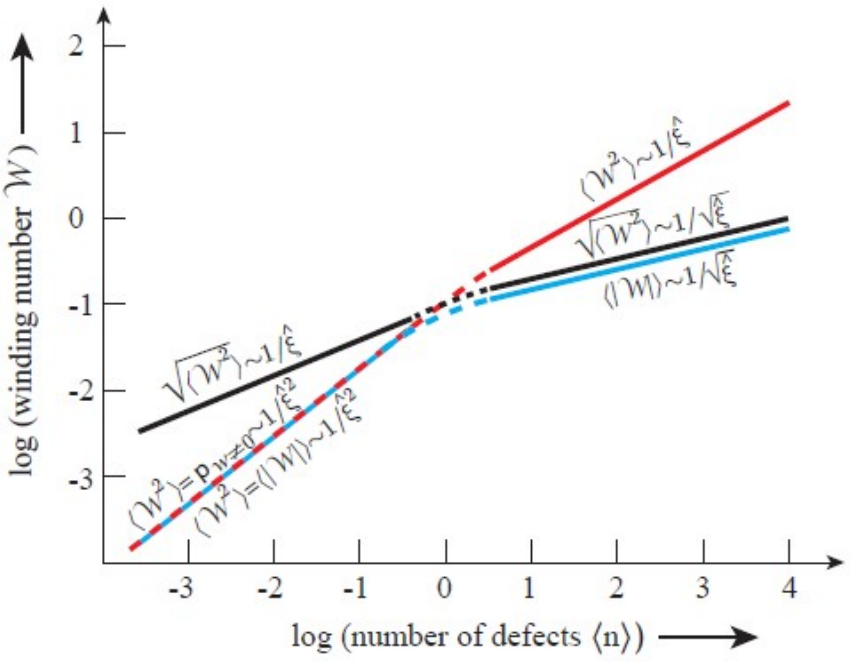

Figure 4.9: **Theoretical prediction of winding number for KZM defects.** Dependence of winding number on the size of contour, note that the slope diverge when $|W| < 1$. The figure is taken from reference [140]

$\langle n\rangle > 1$	$\langle\|W\|\rangle = \sqrt{\langle W^2\rangle} = \langle n\rangle^{1/4}$
$\langle n\rangle < 1$	$\langle\|W\|\rangle = \langle n\rangle$ and $\sqrt{\langle W^2\rangle} = \langle n\rangle^{1/2}$

Table 4.1: **Scaling of winding number for vortex-antivortex pairs.**

the change and divergence of the scalings of $\langle|W|\rangle$ and $\sqrt{\langle W^2\rangle}$) seen in Fig. 4.9. For a fixed shape $C \sim \langle n\rangle^{1/2}$ and large $\langle n\rangle$ typical winding number scaling $|W| \sim \sqrt{\frac{C}{\hat{\xi}}}$ result in $\langle|W|\rangle$ and $\sqrt{\langle W^2\rangle}$) proportional to $\langle n\rangle^{1/4}$.

By contrast, when $\langle n\rangle < 1$, there is usually at most one defect inside C, so W can be only 0, +1, or -1, so $\langle|W|\rangle$ is proportional to probability p of finding a defect. Moreover, $p \sim A$, so now $\langle|W|\rangle \sim A \sim \langle n\rangle$ – typical winding numbers depend on the area A inside C. However, dispersion is proportional to $p^{1/2}$, so $\sqrt{\langle W^2\rangle} \sim C \sim \langle n\rangle^{1/2}$. Thus, when $\langle n\rangle < 1$ scaling of average $\langle|W|\rangle$ and $\sqrt{\langle W^2\rangle}$ differ. It is simply summarized in Table.4.1

4.2.2 Winding number for topological ferroelectric vortices

In order to test the winding number of KZM defects in $RMnO_3$. Large-region optical images have been taken on $ErMnO_3$, $YMnO_3$ and $YbMnO_3$ after chemical etching, see Fig. 2.15. Coordinates for every vortex and antivortex core were found and then analyzed for vortex-antivortex pair correlation function. The average distance between the defects for all the 3 samples: 2.3 m for $YMnO_3$, 2.5 m for $YbMnO_3$, and 14.8 m for $ErMnO_3$. The winding numbers were calculated using the coordinates of the vortices and antivortices in these optical images. Contours of square and rectangular shapes with various sizes were used in the calculations. The results for all three samples are very similar. Fig. 4.10 shows the winding number data for the $YMnO_3$ sample, for which the largest number of the defects (∼4100) was recorded.

The scaling of $\langle|W|\rangle$ and $\sqrt{\langle W^2\rangle}$ with the deformation of the shape of the contour (and the consequent changes of the area A inside) is shown in Fig. 4.11, in which as long as the size of the contour is large compared to $\hat{\xi}$, the winding number depends only on its length, and not on the area enclosed by the loop. However, as expected, the area becomes

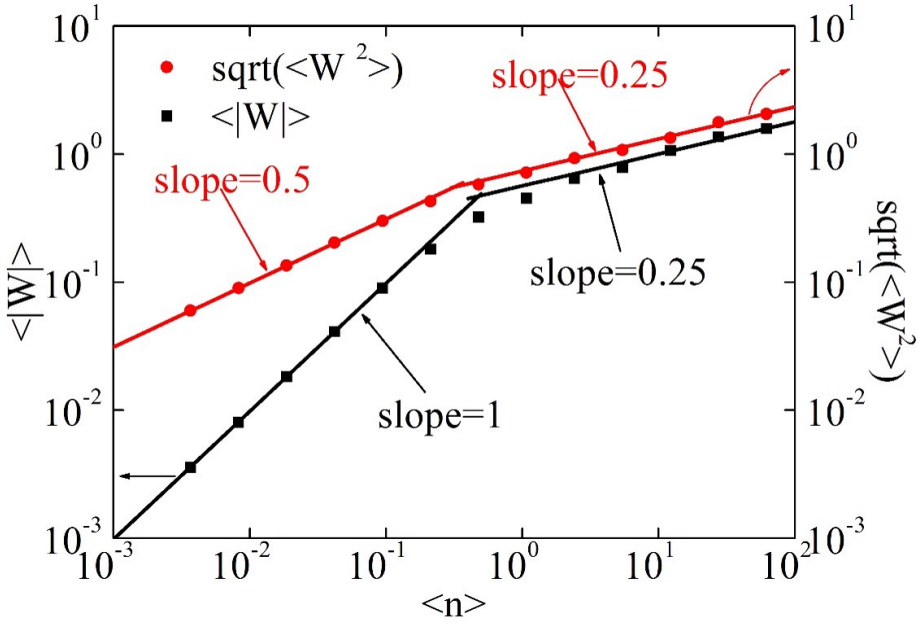

Figure 4.10: **Experimental result of winding number for KZM defects on specimen $YMnO_3$.** The KZM prediction is confirmed for randomly placed contours of a fixed shape

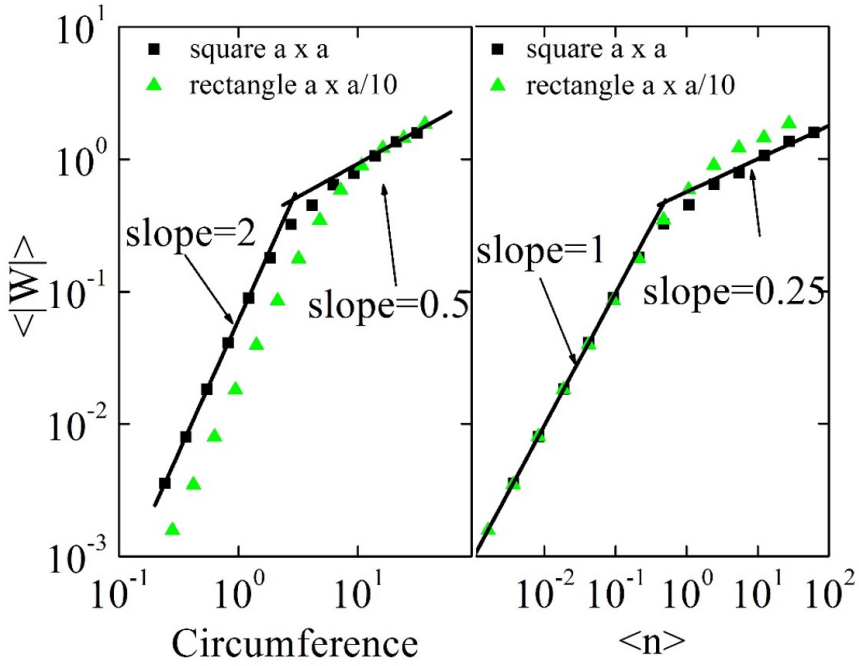

Figure 4.11: **Experimental result of winding number for KZM defects on specimen $YMnO_3$.** Left panel shows $\langle|W|\rangle$ for contours of the same circumference, but with different shapes and, hence, areas that differ by a factor of ~ 3. As expected, $\langle|W|\rangle$ depends on $C^{1/2}$for large $< n >$, but on $A \sim < n > \sim C_2$ for fractional $< n >$. Right panel shows the same data redrawn as a function of $< n >$.

important when the number of defects falls below 1 and the scalings of $\langle|W|\rangle$ and $\sqrt{\langle W^2\rangle}$) steepen and diverge.

Moreover, the vortex-antivortex pair correlation function was also tested by theoretical and experimental studies. Theoretical vortex-antivortex pair correlation function $G(r)$ for the configuration obtained on the surface of the system after annealing from $T_i = 6.0J$ to $T_f = 0.0J$ with a rate $\Delta T = 0.001J$ per MC sweep. we compared the distributions of point-like vortices and anti-vortices (see inset of Fig. 4.12).

We also calculated vortex-antivortex correlation function for the topological defects in hexagonal manganties. We define the vortex-antivortex pair correlation function as $G(r) =< n_s(0)n_s(r) >$, where $n_s(r) = \sum_\alpha q_\alpha \delta(r - r_\alpha)$ is a signed defect density, $q_\alpha = 1(-1)$ for vortices (antivortices), and r_α is the defect position. Both the overall domain patterns and the $G(r)$ obtained from the MC simulations (Fig. 4.12(a)) reproduce well the results obtained from applying the same analysis to the 2D experimental images (Fig. 4.12(b))

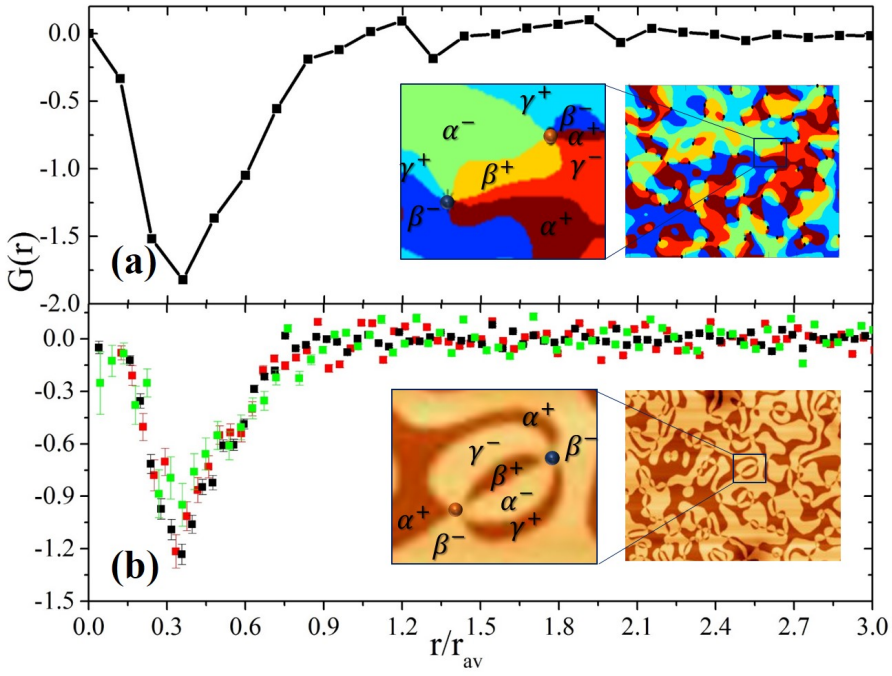

Figure 4.12: **Vortexantivortex pair correlation function.** (a) shows theoretical vortex-antivortex pair correlation function $G(r)$, and (b) is measured $G(r)$ for 3 different specimens.

of three different hexagonal manganites with different vortex densities: $ErMnO_3$ (green), $YMnO_3$ (black) and $YbMnO_3$ (red).

The experimental data are taken and analyzed from Fig. 2.22. Note that The correlation functions were normalized by average distance r_{av} between defects. Thus the distances are scaled by the average defect separation r_{av}, making $G(r)$ dimensionless. Error bars are from counting statistics and represent one standard deviation. The insets show parts of the domain patterns obtained in the calculations (Fig. 4.12(a)) and experimentally measured by AFM in YbMnO3 (Fig. 4.12(b)). The magnified images show vortexantivortex pairs in small regions of these patterns, with the structural phases labelled.The peak in Fig. 4.12(b) occurs at an optimum distance of $0.3^{*}r_{av}$, indicating localized pair formation with a preferred distance. As expected, the same behavior was demonstrated in both Type I and Type II patterns, as well as both low and high density of vortices, with the exact same peaks.

4.3 Duality and Higgs condensation

The topological defects are sources of disorder. More topological defects means more disorder in the system. It is tempting to continue this reasoning by stating that also the transitions into a more disordered phase are therefore caused by topological defects. The defects are then the agents that restore symmetry in the system. The alternative of focussing on disordering instead of ordering of matter is known as a duality. Each point of view is equally valid, and one can freely switch between the one or the other, in the ideal case via a mathematical proof. Moreover, the role of these topological defects in symmetry-breaking phase transitions is now a prime topic in cosmology [63, 138] and high-T_c superconductivity [147–151], even though they are difficult to observe [152].

4.3.1 Duality

As envisioned by Onsager and Feynman [153, 154], the restoration of a continuous $U(1)$ symmetry, like the superfluid to normal transition of ^{4}He, can occur via proliferation of vortices. The potential of having emergent continuous symmetries in magnets or ferroelectrics with discrete microscopic symmetries opens the possibility of observing a similar proliferation of vortices in insulating materials.

In hexagonal manganites, the ϕ^4 field theory of the ferroelectric, where ϕ describes a two-dimensional polarization vector, can be transformed into a dual ψ^4 field theory in terms of a new order-parameter field ψ, known as the disorder field, which describing vortex lines. In this dual description, based on the disorder field of topological vortices instead of the order parameter field [155–157] (see Appendix B), the phase transition is described as a condensation of the disorder field which is coupled to a gauge field [149, 155]. Upon heating across T_c, the vortex condensation makes the gauge field massive via the Higgs mechanism. In this case of superfluid ^{4}He, the corresponding ψ field represents spontaneous vortex excitations in the liquid.

Fig. 4.13 (a) and (b) shows the same phase diagram from two different viewpoints with the order and disorder fields. The local order parameter Φ takes six values, represented by the even hours in the clock dials in (a). They correspond to the six multiferroic states or domains $\alpha+$ through $\gamma-$ distinguished by the polarization direction (+ or -), and the trimerization phase (α, β, γ), as described in the text. Continuous $U(1)$ symmetry emerges from $Z_2 \times Z_3$ order parameter at the critical temperature. The disordered phase above T_c can be described as a condensation of the disorder field ψ signaled by the proliferation of vortex lines spanning the whole system (yellow lines). Only quickly fluctuating closed vortex loops (red lines) are present for $T < T_c$. The Higgs and Coulomb phases of the disorder field are described Appendix B.

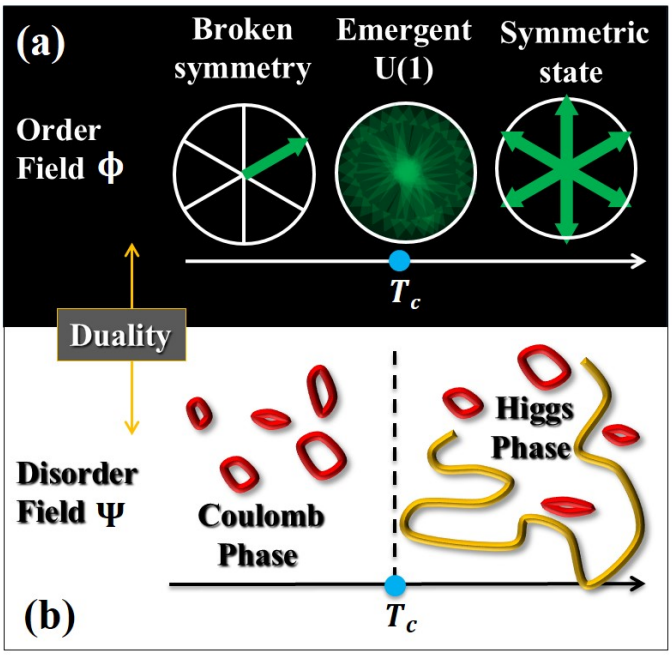

Figure 4.13: **Dual description of a phase transition with $Z_2 \times Z_3$ symmetry.** The phase transition can be described in terms of (a) order field Φ or (b) disorder field Ψ.

4.3.2 Higgs condensation

The vortex-vortex interaction becomes screened above T_c, instead of the Biot-Savart interaction that characterizes the Coulomb phase below T_c. The effective vector potential originates from the long-range hydrodynamic interactions existing between vortices. Thus, the dual theory is a gauge field theory describing a type of fluid exhibiting some of the characteristics of 'superflow' above T_c. Coupling to the effective gauge field gives rise to an Anderson-Higgs mechanism in which the gauge field and the Goldstone mode of the ψ field become massive. This state above T_c in the dual theory is known as the Higgs phase.

In the dual theory, vortex loops are the disordered field. The disorder matter field ψ condensed right above T_c and the emergent gauge field $\mathcal{A}$ acquires a finite mass via the Higgs mechanism. Because the vortices of ϕ are loops of superfluid currents of ψ, a finite faction of these loops must go from one end to the other end of the system when ψ condenses above T_c. Vortices that span the whole system disappear at a much slower rate. Consequently, the final state must be very different depending on whether the initial temperature T_i is

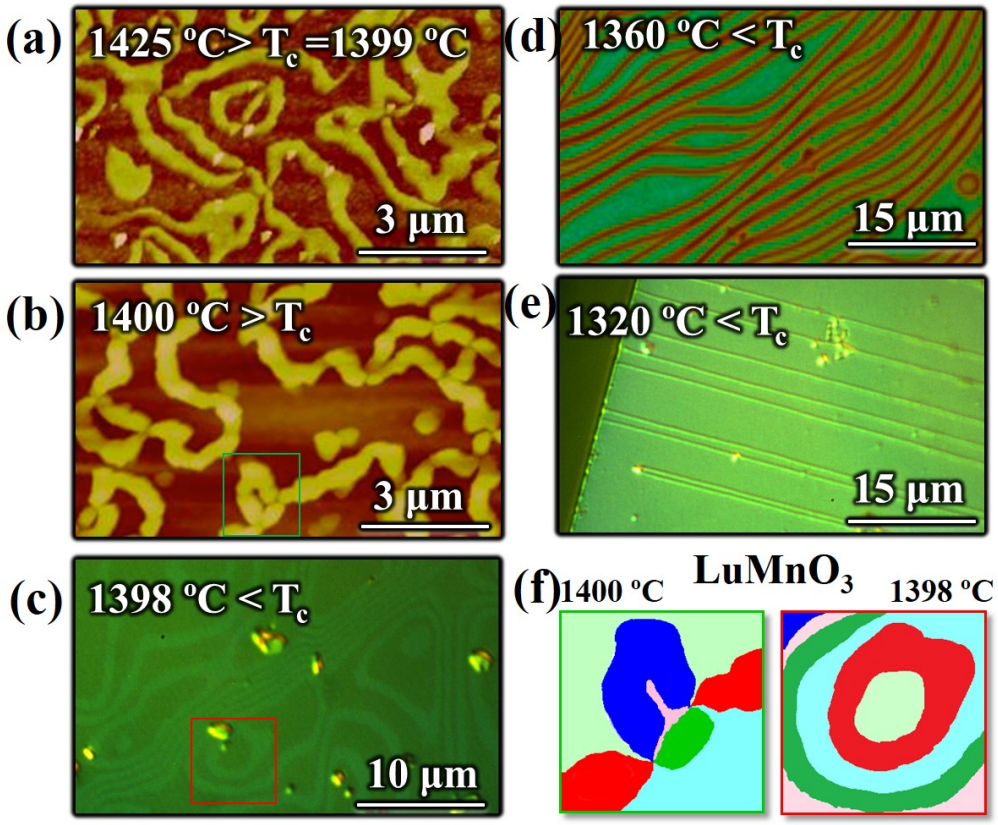

Figure 4.14: **Domain patterns for different initial annealing temperatures T_i (above, close, and below T_c).** AFM images (a,b), and OM images (c-e) of $LuMnO_3$, with T_i indicated in each panel. Vortices are found only for $T_i > T_c$, while stripe and annular domain patterns are observed for $T_i < T_c$. This is illustrated by schematic blowups in panel (f). The plots in (f) correspond to the data in the green and red boxes in panels (b) and (c).

lower or higher than T_c. If $T_i < T_c$, all the vortices form as loops of a finite size implying that they should shrink and disappear upon cooling. The resulting fluctuations turn out to correspond to lines of polarization vortices in which the polarization vectors twist around, forming vortex tubes that run through the crystal and terminate at the crystal surface. On the contrary, if $T_i > T_c$, a significant fraction of the vortex network comes as an infinite string that spans the whole system and can be expected to survive upon cooling.

The experiment in Fig. 4.14 confirmed this analysis. Fig. 4.14(a) and (b), showing AFM images on $LuMnO_3$ with $T_c = 1399°C$ annealed from 1425 °C and 1400 °C, demonstrate the presence of vortices(antivortices), indicating a finite vortex density for $T_i > T_c$. When

$LuMnO_3$ is annealed from temperatures lower than T_c, annular domain patterns, high-density wavy stripes, and low-density straight stripes are found with annealing Ts at 1398 °C, 1360 °C and 1300 °C, respectively. The OM images are shown in Fig. 4.14(c)-(e). The trend is evident: many vortices remain in the final state when $T_i > T_c$. In contrast, the final state for $T_i < T_c$ consists of annular patterns or straight stripes, and contains no vortices or antivortices (Stripes are expected to form due to the long-range dipolar interactions, which are present in the real system, but are not included in our model). This is illustrated by schematic blowups in panel (f), showing vortices for T_i=1400 °C (above T_c), and annular patterns for T_i=1398 °C (below T_c).

Note that the six-fold anisotropy of the clock model is dangerously irrelevant [143, 144] i.e., the critical point belongs to the XY universality class but the discreteness becomes relevant away from T_c. Because the critical region around T_c can be described by the same Ginzburg-Landau ϕ^4 theory that describes the transition of a neutral superfluid (see Appendix B), the ferroelectric order parameter is also destroyed by proliferation of (Z_6) vortices.

4.4 Depth profiling of vortices

Thermally excited vortexantivortex pairs in liquids can form and annihilate rapidly and are therefore usually difficult to study directly. However, in hexagonal manganites, vortices can be frozen-in by rapid cooling, which leading topological defects are not only clearly visible, but (in contrast to e.g. superfluids) they are immobilized by the structure of the material that solidifies below the critical point. Consequently, they can be seen and counted at leisure, long after the transition using AFM, PFM and depth profiling techniques. Moreover, in contrast to other systems used as a test bed for KZM [158–166], the quench timescale τ_Q can be varied over orders of magnitude. This is important, as densities of defects predicted by KZM often scale as τ_Q to small fractional power.

According to the dual theory (see Fig. 4.13 and Appendix B), a finite fraction of vortex

lines span the whole system above T_c, i.e., the corresponding vortex cores connect opposite surfaces of the sample. Therefore, it is natural to conjecture that the 6-state vortex domain structures observed on the surface of $RMnO_3$ correspond to transverse cuts of these vortex cores. This conjecture is substantiated by the PFM 3D images of vortex cores in the *h*-$LuMnO_3$ crystal, showing in Fig. 4.15.

These images are obtained after a sequence of three steps: a) heating a hexagonal $LuMnO_3$ single crystal up to $T = 1425°C$ ($> T_c = 1399°C$), b) keeping the temperature constant for 30 minutes, and c) cooling the specimen down to room temperature. The emergence of a vortex domain pattern on the *ab* surface of the crystal is revealed by chemical etching. To obtain a 3D picture of vortex cores (i.e. a depth profiling of vortex domain patterns), the sample is consecutively thinned down (polished) along the *c* axis and PFM images of the same region are taken for different depths (see Fig. 4.15(a)). The depth of each polished surface from the original surface is shown in micro-meters. Enlarged areas exhibiting the depth evolution of vortex cores in red and green boxed regions are shown in Fig. 4.15 (b) and (c), respectively. The large spatial extension of vortex cores is evident in the figure. The schematics of the vortex networks shown in Figs. 4.15(d) and (e) are obtained by depth profiling of the 2D vortex cores. The dark and light regions correspond to the domains with the opposite electric polarizations.

To simulate this phenomenon, we ran Monte Carlo (MC) simulations of 3D clock model based on a local update Metropolis algorithm because the microscopic dynamics of $RMnO_3$ is expected to be local. The lattice size is $L^2 \times L_z$ with L = 192 a and $L_z = 96$ a (a is the lattice parameter). We used periodic boundary conditions in the xy plane and open boundary condition along the z direction. The critical temperature obtained for $J' = J$ is $T_c \approx 3.03J$. The vortices shown in Fig. 4.15(f) were obtained after annealing from an initial temperature $T_i = 6.0J$ down to $T_f = 0$ with a rate $\Delta T = 0.005J$ per MC sweep (MCS). This prediction can be motivated [146] by using a simple model where defects of opposite charge appear in pairs and both their size and typical separations are given by $\hat{\xi}$.

This pairing of vortices and antivortices is an *adhoc* model, although it can be motivated by considering the 3D geometry of vortex lines and their relation to the vortices that appear as a 2D plane intercepts a 3D sample (see e.g. Fig. 4.15).

The observation of the KZM in a non-equilibrium phase transition with the scaling of

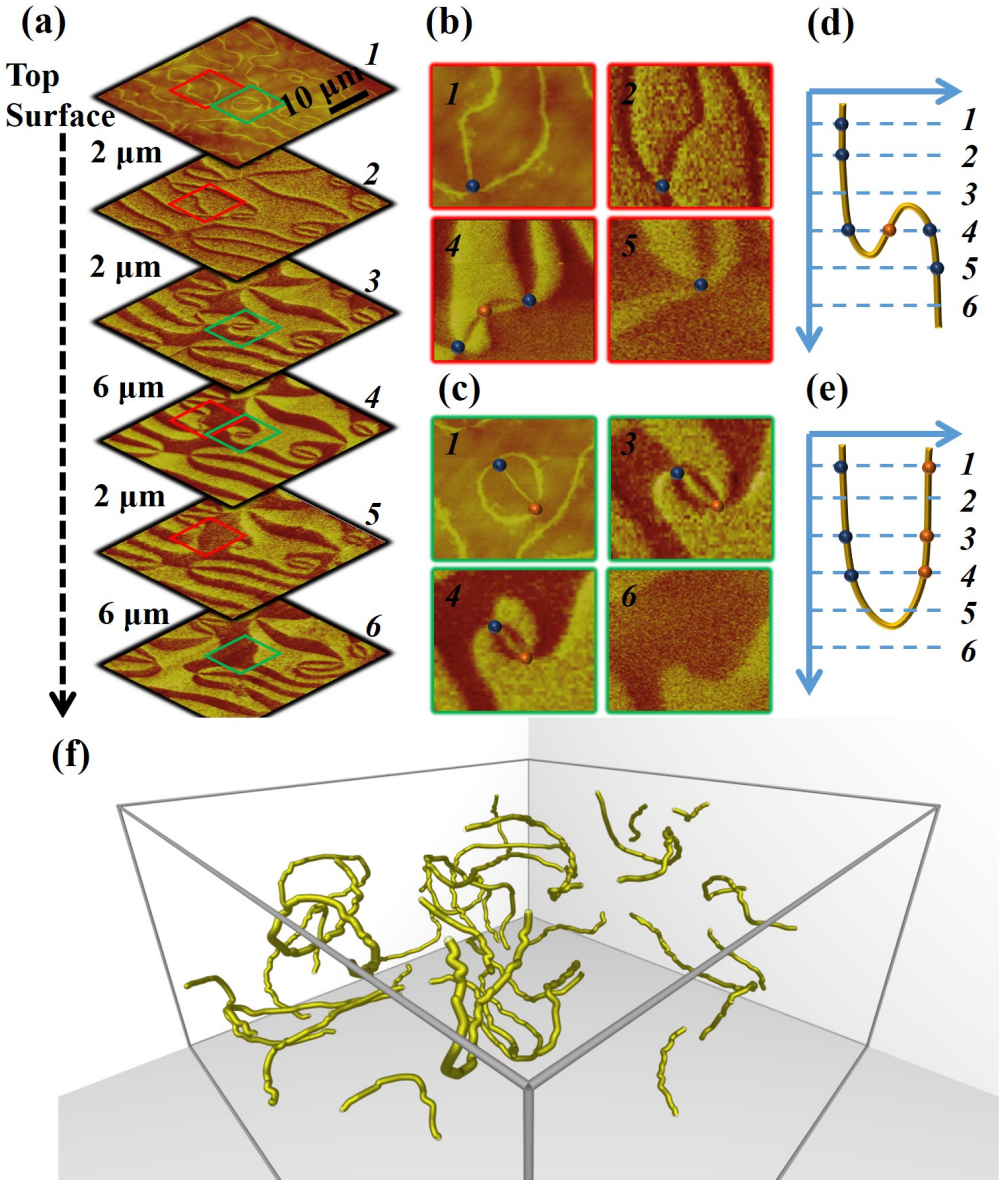

Figure 4.15: **3D picture of vortex cores: a depth profiling of vortex domain patterns.** (a) Evolution of ferroelectric domains on the polished surface of a h-$LuMnO_3$ crystal. (b) and (c) are enlarged areas exhibiting the evolution. Panels (d) and (e) depict the obtained depth profiles of the vortex cores for the regions shown in (b) and (c), respectively. (f) Vortex loops and lines spanning the whole system obtained from our Monte Carlo simulations of the 3D clock model at $T > T_c$.

defects density determined by the exponents of the 3D XY model provides further confirmation of the emergent $U(1)$ at the critical point of the structural transition. It is then natural to expect a proliferation of vortices right above the transition. However, because the symmetry remains discrete at temperatures away from the critical point, the continuous $U(1)$ vortices that appear in superfluid systems are replaced by the discrete Z_6 vortices observed in h-$RMnO_3$ at room temperature. This novel realization of a 3D XY transition has a unique advantage relative to superuids: the possibility of freezing vortices in h-$RMnO_3$ provides a unique opportunity to study the disorder eld (dual theory) and measure the experimental consequences of the Higgs mechanism that arises from its condensation.

In particular, geometric properties of the vortex field of $RMnO_3$ can be related to the critical exponents of the dual abelian gauge theory that describes the disorder field (see Appendix B). For instance, the critical exponent that controls how the effective line tension of vortices vanishes when T_c is approached from below is $\gamma = \nu_\psi(2 - \eta_\psi)$, where ν and η are the critical exponents of the dual or disorder matter field [167]. Because the dual field is described by the same abelian gauge theory that describes the order parameter field of a charged superfluid, measuring the critical behavior of vortices in $RMnO_3$ would provide information about the critical exponents of a charged superfluid, such as a strongly type II superconductor.

Chapter 5

Partially Undistorted Antipolar (PUA) vortex

Ferroelectric $YMnO_3$ is following the determination by that these manganites have a structure described as that of a distorted perovskite, led to substantial interest in their properties. Among these h-$RMnO_3$ family, $InMnO_3$, where In ions are much smaller than any RE ions in size, does form in a similar hexagonal structure, and thus it is also intriguing to have potential of ferroelectricity in h-$InMnO_3$. However, ferroelectricity in $InMnO_3$ has been highly controversial and still under debate.

In this chapter, we will firstly clarify the correct crystallographic ground state and the ferroelectricity in well-controlled specimens of $InMnO_3$, which will be followed by a discussion of an interesting state which can be stabilize by Ga doping in h-$InMnO_3$. It turns out to be a "dual" picture to the $Z_2 \times Z_3$ vortex.

5.1 Sample growth

Polycrystalline crystals of $InMnO_3$ were prepared from In_2O_3 (99.999%), MnO_2 (99.99%) and Bi_2O_3 (99.975%) as flux [168]. The flux to reactants ratio was 1: 2: 0.05. The binary oxides were ground together and pelletized, then was heated at 980 °C for 200 hours in air on platinum lid. The cooling sequence influence the properties of the specimen, which we will discuss below.

Note that with different ratio of Bi_2O_3 flux, one can improve the growth of $InMnO_3$, with ratio In_2O_3 : Bi_2O_3 = 1: 0.05, one can get mostly pure phase of polycrystalline $InMnO_3$, since most of Bi_2O_3 is vaporized at high temperature. With ratio 1:0.2, the grain size of

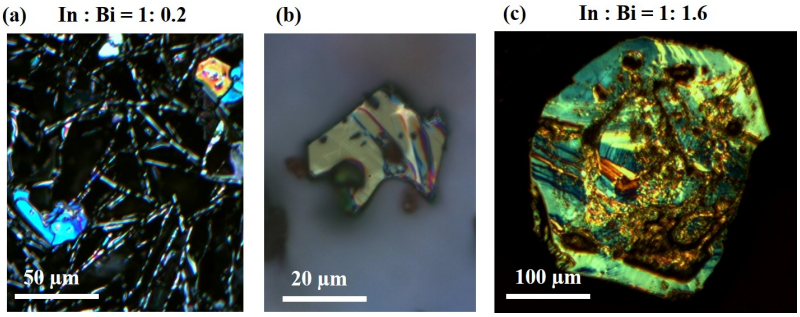

Figure 5.1: **Bi_2O_3 flux improves the growth of $InMnO_3$.** (a) shows when In_2O_3 : Bi_2O_3 = 1: 0.2, the grain size of polycrystalline $InMnO_3$ is around 50 microns, (b) is after breaking the pellet, one can get tiny single crystal of $InMnO_3$. (c) shows one single crystal of $InMnO_3$ by ratio 1: 1.6

polycrystalline $InMnO_3$ is enlarged. With higher ratio like 1: 1.6, one can get small single crystal of $InMnO_3$, where partial melting of the pellet occurred during the heating cycle, and Bi_2O_3 flux apparently enhanced the growth of $InMnO_3$ crystals. See Fig. 5.1.

Polycrystalline crystals of $In(Ga_xMn_{1-x})O_3$ (x=0.05, 0.10, 0.20, 0.30, 0.35, 0.37, 0.39, 0.40, 0.41, 0.42, 0.43, 0.45, 0.47)were prepared from In_2O_3 (99.999%), MnO_2 (99.99%), Ga_2O_3 (99.99%), and Bi_2O_3 (99.975%) as flux. The flux to reactants ratio was 1: 2: 0.05. The binary oxides were ground together and pelletized, then was heated at 1000 °C for 200 hours in air on platinum lid, then followed by 10 °C/h cooling to room temperature. However, single crystal growth of Ga doped $InMnO_3$ is still unclear.

A complete list of growth trials of all relative compounds are shown in Appendix C

5.2 Ferroelectricity in $InMnO_3$

$InMnO_3$ was theoretically predicted and experimentally claimed to show weak ferroelectricity with $T_c \sim 500$ K [169, 170]. More recently, despite a fully filled 4d orbital in $InMnO_3$ distinct from $YMnO_3$ [171], Oak *et al.* proposed an alternative intra-atomic orbital mixing of In and a covalent bonding along the *c* axis, resulting in a ferroelectric ground state [172]. On the other hand, Belik *et al.* reported the absence of spontaneous polarization [173]. In addition, Kumagai *et al.* reported their experimental results of no ferroelectric signals

in second-harmonic generation (SHG) and PFM measurements, and concluded a nonpolar structure for $InMnO_3$ [174]. Based on density functional theory (DFT) calculations, they also claimed that the ground state is a nonferroelectric state with the space group of $P\bar{3}c1$ even though there exists only a small energy difference between the nonpolar $P\bar{3}c1$ and ferroelectric $P6_3cm$ states.

In general, X-ray and electron-diffraction methods are the two main powerful and robust techniques to study crystallographic structures. However, the same extinction rules in both $P6_3cm$ and $P\bar{3}c1$ states provide difficulties to distinguish them from, for example, x-ray structural refinements, even though slightly different intensity ratios of Bragg peaks exist due to different structural factors. Moreover, PFM scanning is also able to tell if the system has polar properties, however, on one hand, as we discussed in the KZM section, the domain size of vortex can be either small or large with different RE ion, so PFM scanning may not have enough resolution for distinguishing the vortex. On the other hand, the preparation of high-quality $InMnO_3$ and the growth of decent-size single crystals turn out to be challenging, which is partially the origin of the controversy.

However, DF-TEM is an ideal and well-known technique to examine domain structures in ferroelectric and nonferroelectric materials because of its high spatial resolution and ability to isolate specific types of domains using a specific diffraction spot. In particular, we can examine the existence of inversion symmetry by taking advantage of Friedels law, where the Friedel-related pairs of Bragg reflections should behave differently in a noncentrosymmetric structure.

Four polycrystalline $InMnO_3$ specimens are discussed in the following: IMO-a was slowly cooled (2 °C/h) from 980 °C, IMO-b was furnace cooled, IMO-c was quenched from 950 °C, and IMO-d was quenched from 650 °C to room temperature after being cooled slowly (10 °C/h) from 980°C. All four $InMnO_3$ specimens have been confirmed to show a $\sqrt{3} \times \sqrt{3}$ super-lattice from the $P6_3/mmc$ paraelectric structure in x-ray diffraction patterns.

Fig. 5.2 is a typical DF-TEM image of IMO-a using the 2 opposite **g** vectors along the

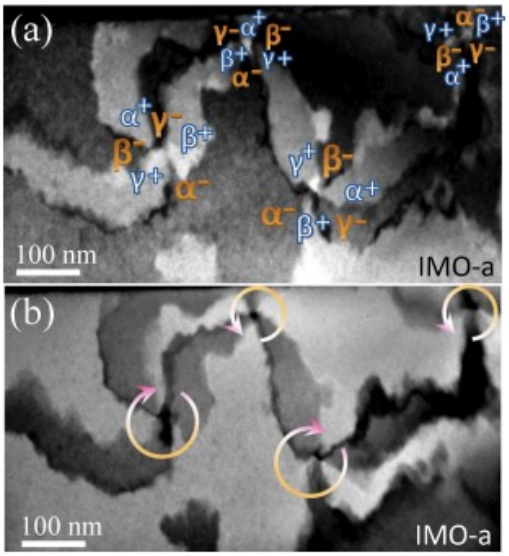

Figure 5.2: **DF-TEM images of slowly cooled $InMnO_3$.** DF-TEM image of slow-cooled IMO-a, exhibits topological vortexantivortex domains. The contrast reversal is due to the Friedels pair breaking.

[101] direction based on $P6_3cm$, which displays $Z_2 \times Z_3$ vortices. This contrast reversal between Fig. 5.2(a) and (b) demonstrates unambiguously the Friedels pair breaking due to the non-centrosymmetrical structure of $InMnO_3$. The bright and dark contrasts of vortices also result from the violation of the Freidels law where neighboring domains have exactly parallel lattices, but oppositely-oriented non-centrosymmetry axes, i.e. they are 180° non-centrosymmetric domains. The typical size of vortex domains in IMO-a is about 100-200 nm, which is significantly smaller than that of any h-$RMnO_3$, showing vortex domains with the size of a few micrometers [48].

However, on the other hand, for IMO-b, which is furnace cooled specimen, the DF-TEM image in Fig. 5.3(b) shows diffusive contrasts and many nanometer-sized dark speckles indicates by sky-blue circles. It is plausible that the speckle-type pattern turns into vortex domains when a specimen is cooled slowly from the synthesis temperature. Note that the breaking of the Friedel pairs does not take place for those speckles, indicating that those speckles contribute to the $\sqrt{3} \times \sqrt{3}$ superlattice peaks but are not associated with

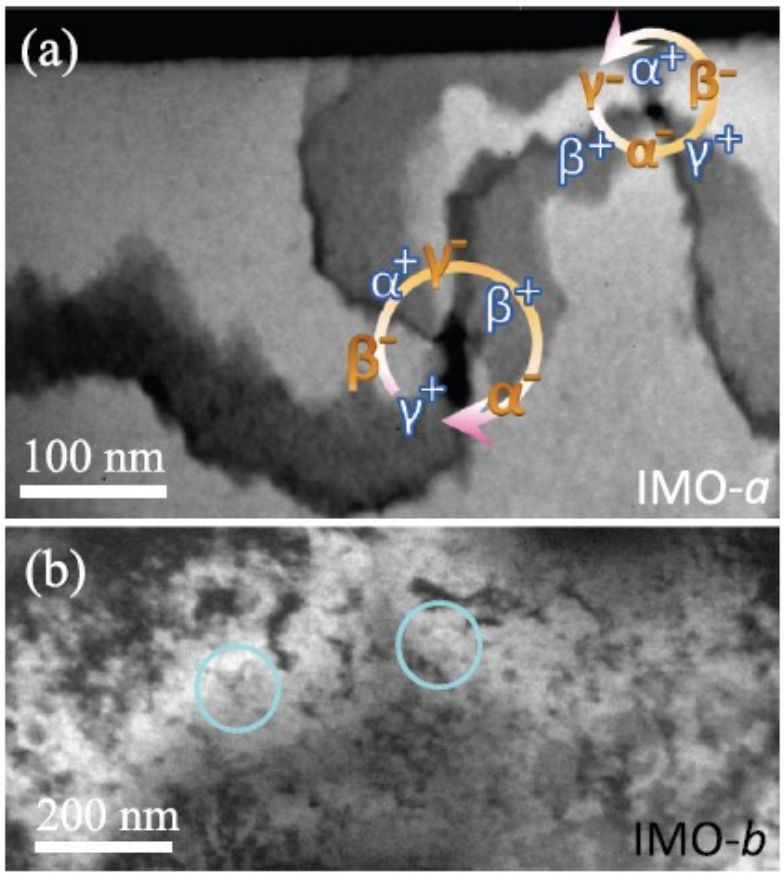

Figure 5.3: **DF-TEM images of slowly cooled and furnace cooled $InMnO_3$.** DF TEM image of slow-cooled IMO-a, exhibits topological vortex(antivortex) domains. (b)DF TEM image of furnace-cooled IMO-b, showing numerous nanoscale speckles.

the inversion symmetry breaking. It turns out the furnace-cooled IMO-b exhibits a few-nanometer-scale region with a non-polar down-no-up In configuration embedded in the polar up-up-down matrix [175].

In the non polar $P\bar{3}c1$ state, In ions sit equally on 1/3 downward, 1/3 in mirror plane, and 1/3 upward (down-no-up) positions [174]. In frustrated Ising triangular (i.e., hexagonal) antiferromagnets, a PDA state refers to a partially disordered antiferromagnetic state where spins on a honeycomb lattice portion of the hexagonal lattice order antiferromagnetically, and the rest of spins are disordered [176]. Due to the evident analogy, we call the nonpolar $P\bar{3}c1$ a partially undistorted antipolar (PUA) state.

The existence of such nanoscale PUA islands,which appear to correspond to speckles in DF-TEM images is certainly different from the behavior of the thin domain walls with down-no-up distortions, which were first proposed as a possible configuration for the ferroelectric-trimerization domain walls in hexagonal $YMnO_3$, studied theoretically[125] and also observed experimentally [100].

In order to clarify the origin of the PUA islands in IMO-b, we performed DF-TEM and HAADF-STEM experiments on specimens from two different annealing temperatures [950 °C(IMO-c) and 650 °C(IMO-d)]. Fig. 5.4(a) shows a DF-TEM image of IMO-c, which exhibits no hint of the vortex type domains, and a HAADF-STEM image [Fig. 5.4(d)], in fact, demonstrates a long-range PUA statei.e., down-no-up In distortions are everywhere in the image. On the other hand, IMO-d exhibits small vortex-antivortex domains (50200 nm in size) with highly curved boundaries as shown in Fig. 5.4(b), which indicates the presence of a ferroelectric state. Furthermore, when a specimen was quenched from 750 °C, its behavior was in between those of IMO-c and IMO-d i.e., a mixture of very fine vortex-antivortex domains and PUA islands.

These results suggest strongly that the PUA is a stable state near 950 °C, the high-temperature PUA can be quenched to room temperature, the transition from the high-temperature PUA to the low-temperature FE is very sluggish, and the ground state is

FE.10,11 The evolution of the structural phase in $InMnO_3$ is schematically illustrated in Fig. 5.4(c). Note that $P6_3cm$ and $P\bar{3}c1$ are subgroups of $P6_3/mmc$, but $P6_3cm$ and $P\bar{3}c1$ have no subgroup relationship to each other, so it is expected that the transition between $P6_3cm$ and $P\bar{3}c1$ is first-order type. So the ground state of $InMnO_3$ is ferroelectric with $P6_3cm$ symmetry, but a non-ferroelectric $P\bar{3}c1$ state exists at high temperature and can be quenched to room temperature.

5.3 PUA vortex

Though the PUA phase can be achieved and stabilized through fast quenching of the $InMnO_3$ specimen from high temperature, the PUA vortex has never been observed in

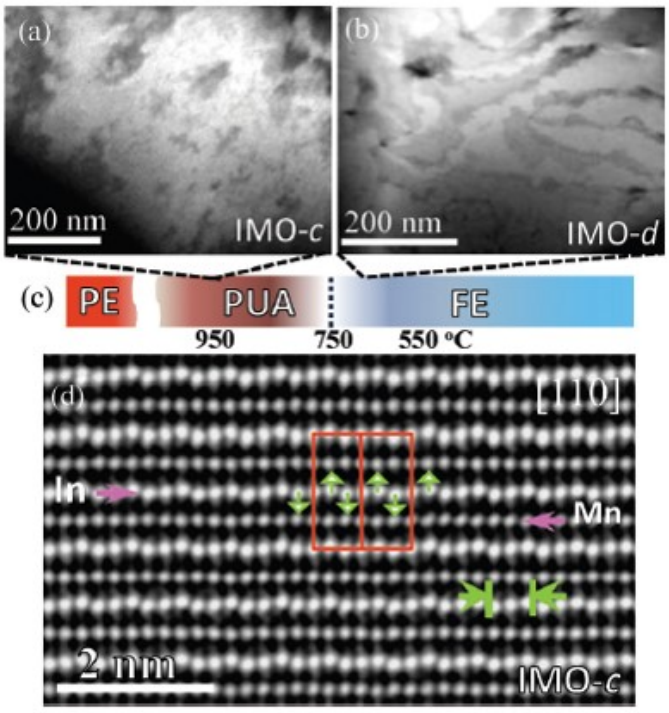

Figure 5.4: **A schematic for the temperature evolution of $InMnO_3$ phase.** (a, b) DF-TEM images of IMO-c and IMO-d. (c) A schematic for the temperature evolution of $InMnO_3$ phases. (d) HAADF-STEM image of IMO-c shows a long-range PUA state with down-no-up In distortions. The red rectangles display the unit cells, and green arrows depict atomic In distortions.

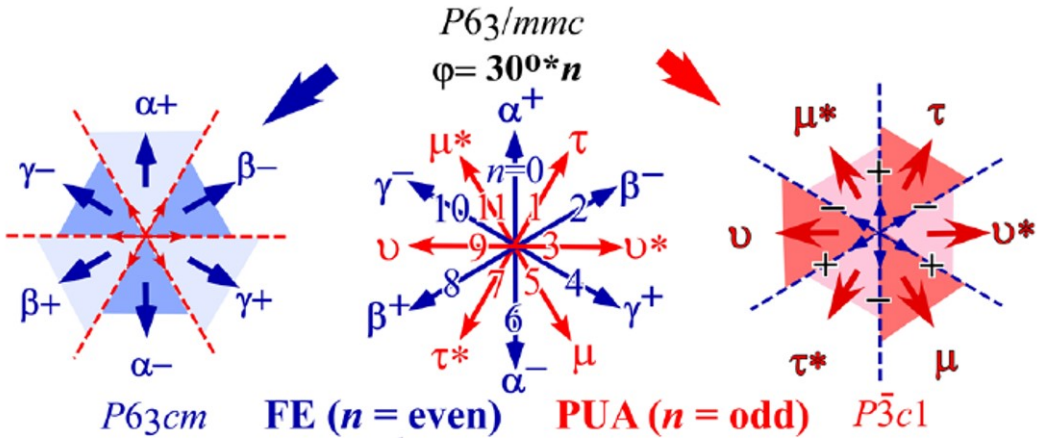

Figure 5.5: **Cloverleaf vortex domains and domain walls in ferroelectric and PUA phases.** Twelve possible angles of MnO_5 tilting and relevant phases. Schematics of FE (left) and PUA (right) vortices.

the ground state of h-$RMnO_3$ series. In stead of focusing on $InMnO_3$, we choose an alternative approach to stabilize PUA phase: Using Ga doping on the Mn site we apply an effective in-plane compressive strain which was shown previously to tip the energy balance between the ferroelectric and PUA phases so that PUA is the ground state [174].

For the vortex in ferroelectric $P6_3cm$ symmetry phase, it is reduced from hight symmetry phase to $Z_2 \times Z_3$ for larger K_3 through an angle-dependent coupling to a secondary polar mode Γ_2^- consisting of a polar displacement of the R cation sublattice. For positive Γ_2^- the coupling is most energy lowering for K_3 tilt angles of 0°, 120° and 240° , whereas negative Γ_2^- favours angles of 60°, 180° and 300° (Fig. 5.5(a) blue arrows), yielding a modified Mexican hat potential with six minima in the brim that have alternating polarization directions. In the same analogy, the vortex in $P\bar{3}c1$ structure is obtained by tilting of the MnO_5 bipyramids at intermediate angles of 30°, 90°, 150°, 210°, 270°, and 330°, accompanied by an up-down-no pattern of In-ion displacements, see red arrow in Fig. 5.5(a). From symmetry arguments, this PUA state should, in principle, present $Z_2 \times Z_3$ PUA vortices analogous to those in the ferroelectric structure, with six possible domains corresponding to three different phase shifts (τ, ν, μ) combined with two oxygen-distortion handedness.

A superlattice DF-TEM image showing a ferroelectric vortex in h-$InMnO_3$ is shown

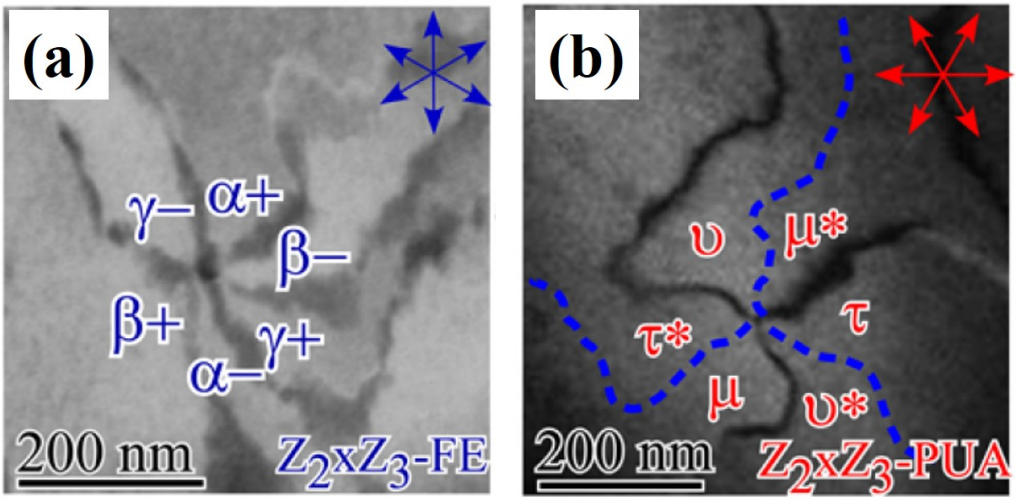

Figure 5.6: **Cloverleaf vortex domains and domain walls in ferroelectric and PUA phases.** (a) A superlattice DF-TEM image showing a ferroelectric vortex in h-$InMnO_3$. (b) A superlattice DF-TEM image showing three obvious domain walls meeting at one point (PUA vortex) in $In(Ga_xMn_{1-x})O_3$. The blue dashed lines depict the three hidden walls.

in Fig. 5.6(a), and (b) shows our superlattice DF-TEM images of PUA domains in h-$InMn_{0.95}Ga_{0.05}O_3$. At first sight, Fig. 5.6(b) appears to show a Z_3 pattern, with three lines meeting at one point, which would contradict the known $P\bar{3}c1$ symmetry. Careful examination by tilting to tune contrast through enhancing excitation error reveals, however, six domains with hidden walls alternating with easily visible walls [177]. Our DF-TEM images for the first time demonstrate a $Z_2 \times Z_3$ PUA vortex pattern in $In(Ga_xMn_{1-x})O_3$ comparable with that in the ferroelectric h-$RMnO_3$, although, in this case, three of the domain walls are clearly of a different nature than the other three. Since strain provides the main diffraction contrast change in our DF-TEM images, we associate the weak-contrast walls with a lower internal strain field.

Such a continuous symmetry is unexpected for crystallographic phase transitions in condensed-matter systems, the nature of the spontaneous symmetry breaking can be systematically chemically manipulated to yield two complementary ground states; a ferroelectric phase of $P6_3cm$ symmetry, and a non-polar $P\bar{3}c1$ phase. We discover that both

symmetry breakings, which are described by related Mexican hat-like potentials, yield topologically protected $Z_2 \times Z_3$ vortex defects, with those of the non-polar phase being dual to those of the ferroelectric phase. A complete unified symmetry description of the hexagonal manganites is more discussed in [177].

Chapter 6

Epilogue

This thesis presents a systematic study of the ferroelectric domains in multiferroic hexagonal manganites $h-RMnO_3$, to reveal the beauty of the multiferroic vortex, as topological defect. What I want to emphasize is: all the work are based on high quality single crystal of various $h-RMnO_3$ by different crystal growth method. Note that the domain and domain walls are easily pinned and bounded by any 'real defects' on the sample surface or inside the sample, which might destroy the nature of self-organized vortices domain network. In this chapter I will summarized the results of all discussed projects and try to give a future research direction.

6.1 Review of results

In chapter 2, following previous researcher's solid steps, we have clarified the origin of two types of topological vortex domains: type-I and type-II domain networks in bulk crystals of hexagonal manganites, one of which is induced by self-poling due to oxygen off-stoichiometry. We have performed different annealing procedures of a large number of well-controlled crystal specimens, we found that the nature of self-poling in $h-RMnO_3$ is much richer than that ever reported in any other system: (i) we found the change from type-II domains at the surface into bulk type-I domains is induced by oxygen vacancy gradient; (ii) the change between two different type-II domains with opposite preferred polarization directions induced by non-monotonic oxygen vacancy distribution, and the presence of charged walls between two different trimerization antiphase domains associated with these domain configuration changes. (iii) we also investigate the statistical distributions of the N-gons

in the domain networks of hexagonal manganites on three different $h-RMnO_3$ specimens. Different behaviors of N-gon distributions between type-I and type-II are observed, which might related to self-organized criticality. (iv) We have also observed an extreme self-poling effect with strong vortex domain wall pinning, resulting in vortex core fragmentation. This vortex core defragmentation appears to stem from the high instability of charged ferroelectric domain walls with the same trimerization phase.

The self-poling part is published in [178] *Xueyun Wang, Fei-Ting Huang, Rongwei Hu, Fei Fan and Sang-Wook Cheong*, **Self-poling with oxygen off-stoichiometry in ferroelectric hexagonal manganites**, APL Mat. **3**, 041505 (2015). The N-gon analysis part is under review, *Fei Xue, Xueyun Wang, Ion socolenco, Yijia Gu, Long-Qing Chen, and Sang-Wook Cheong*, **Complex networks of topological vortices and antivortices in hexagonal manganites**.

Chapter 3 mainly focuses on the manipulation of vortices. Unlike what happened in skymrions or vortices in superconductors, electric field can only readily move domain walls instead of topological vortices cores, we demonstrated that, in $h-RMnO_3$, employing shear strain with a large gradient, we were able to transform vortices and antivortice into stripes in $h-$ $ErMnO_3$. This stripe domain state is monochiral and shows the alternation of walls with distorted and undistorted (can be viewed as a PUA wall) Er ions. Combining the theoretical calculation and experimental observation, we proposed that shear strain induces a Magnus-type force pulling vortices and antivortices in opposite directions and unfolding them into a topological stripe domain state. The analogy between this effect and the current-driven dynamics of vortices in superconductors and superfluids is also discussed. Our findings reveal an unexpected topological relation between vortex and stripe domains in $h-RMnO_3$, and also provide a novel way of controlling topological defects.

The relative part in Chapter 3 is published [179] *Xueyun Wang, Maxim Mostovoy, Myung-Geun Han, Yoichi Horibe, T. Aoki, Yimei Zhu and Sang-Wook Cheong*, **Unfolding of Vortices into Topological Stripes in a Multiferroic Material**, Phys. Rev. Lett.

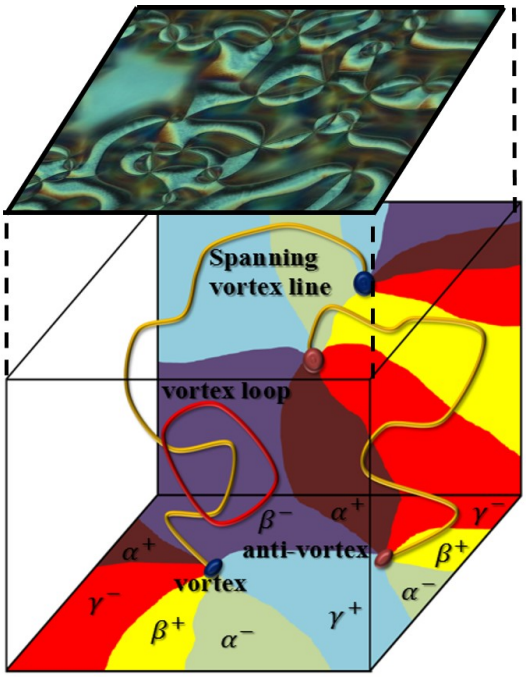

Figure 6.1: **A simple summary of $Z_2 \times Z_3$ vortices.**

112, 247601, 2014 and [132] *Myung-Geun Han, Yimei Zhu, Lijun Wu, Toshihiro Aoki, Vyacheslav Volkov, Xueyun Wang, Seung Chul Chae, Yoon Seok Oh and S. W. Cheong* , **Ferroelectric Switching Dynamics of Topological Vortex Domains in a Hexagonal Manganite**, Advanced Materials. **25**, 2415-2421, 2014.

Following the work done by Griffin *et al.* [102] and Chae *et al.* [91], in chapter 4, we performed more detailed study of manipulation on density of vortices depending on various cooling rates. Like what we expect, we found a similar scaling of vortices density determined by the exponents of the 3D XY model, which provides further confirmation of the emergent $U(1)$ at the critical point of the ferroelectric structural transition in $h-\mathrm{RMnO_3}$.

More importantly, we have successfully imaged 3D vortex evolution from a proliferation technique. This novel realization of a 3D XY transition has a unique advantage relative to superfluids: the possibility of freezing vortices in $h-\mathrm{RMnO_3}$ provides a unique opportunity to study the disorder field (dual theory) and measure the experimental consequences of the Higgs mechanism that arises from its condensation. The confirmation of the KZM in a 3D

XY critical point (the same universality class as the λ transition in ^{4}He) suggests that the failure to detect [180] KZM vortices in ^{4}He quench experiments may be due to their rapid annihilation combined with the inability to measure their density right after the quench. $h-RMnO_3$ bypass this problem by immobilizing vortices in the matrix of the material soon after the quench, preventing their annihilation.

The relative part in Chapter 4 is published [66] *Shi-Zeng Lin*, Xueyun Wang*, Y. Kamiya, Gia-Wei Chern, Fei Fan, David Fan, Brian Casas, Yue Liu, Valery Kiryukhin, Wojciech H. Zurek, Cristian D. Batista, and Sang-Wook Cheong (*These authors contribute equally)*, **Emergent continuous symmetry and Higgs condensation of disorder in ferroelectrics** , Nature Physics **10**, 970977 (2014).

After comprehensive physics exploration on the nature of vortex, in Chapter 5, firstly, we have clarified a long-standing dispute of the ferroelectric state in $h-InMnO_3$. From a systematic study of well controlled specimens, we identified that the ground state is a ferroelectric state with $P6_3cm$ symmetry. In addition, the ferroelectric ground state accompanies topological vortex domains, similar to what was observed in $h-RMnO_3$. On the other hand, we have demonstrated the existence of an intermediate centrosymmetric structure with $P\bar{3}c1$ symmetry. Furthermore, we found that the transition from the intermediate centrosymmetric to the ferroelectric ground states is unusually sluggish. Our findings reveal the rich nature of structure-driven improper ferroelectricity. We also extended our scope from typical vortex to its dual image – PUA vortex. We show that the spontaneous symmetry breaking in multiferroic hexagonal manganites can be chemically manipulated to yield two complementary ground states: the well-known ferroelectric $P6_3cm$ and an antipolar $P\bar{3}c1$ phase. Both symmetry breakings yield topologically protected vortex defects, with the anti-polar vortices dual to those of the ferroelectric. This duality stems from the existence of 12 possible angles of MnO_5 tilting, and broad strain-free walls with low energy spontaneously emerge through an intermediate $P3c1$ state, providing a complete unified symmetry description.

Note that the unique duality between topological PUA and ferroelectric vortices reveal the nature and beauty of space group change from high symmetric phase to low symmetric phase. In the PUA phase, the non-polar domains are separated by polar domain walls of alternating polarity, whereas in the ferroelectric phase, the alternating polar domains are separated by non-polar walls which can have the PUA structure. The broad domain walls show a progressive evolution of the In displacements and polyhedral tilt angles corresponding to a new phase of $P3c1$ symmetry, which completes the set of symmetry-allowed structures for the hexagonal manganites. Our results indicate and explain the duality between the vortices in ferroelectric and PUA hexagonal manganites, and provide a unified picture of the symmetry by identifying for the first time the $P3c1$ phase.

The PUA part is published [175, 177]: *Fei-Ting Huang, Xueyun Wang, Y. S. Oh, K. Kurushima, S. Mori, Y. Horibe, and S. W. Cheong* , **Delicate Balance between ferroelectricity and antiferroelectricity in hexagonal $InMnO_3$**, Phys. Rev. B. **87**, 184109 (2013), and *Fei-Ting Huang, Xueyun Wang, SineadM. Griffin, Yu Kumagai, Oliver Gindele, Ming-Wen Chu, Yoichi Horibe, Nicola A. Spaldin, and Sang-Wook Cheong*, **Duality of Topological Defects in Hexagonal Manganites**, Phys. Rev. Lett. **113**, 267602 (2014).

6.2 Future research

Starting from the scope of this work, there still unsolved problems requiring more research as discussed below.

(1) On the materials improvement side, intrinsic physics always require high quality single crystals. In term of $h-RMnO_3$, single crystal of $InMnO_3$ is only reported in ref.[181]. On one hand, domain study by scanning experiments, like PFM or MFM will be much easier if we have high quality single crystal of $InMnO_3$. On the other hand, as we discussed, stabilization of PUA vortex with Ga doping in $InMnO_3$ enable the existence of broad polar walls in the PUA phase, which will provide a novel way to design new ferroelectric devices,

considering the tunable conducting domain walls.

Moreover, identifying new types of (multi)ferroics with topological phase transitions will also be interesting. It has been discussed that the discrete six-fold clock nature of the polarization in the ferroelectric manganites develops a continuous $U(1)$ XY symmetry close to the ferroelectric critical point. This 'emergent symmetry' has also been anticipated for certain ferroelectrics with a discrete 3D order parameter. For ferroelectrics and paraelectrics with a polarization free to point in 3D space, it would be fascinating to search for the corresponding thermally excited skyrmions and anti-skyrmions. The domains and defects related to their formation will provide new test bed for the phenomena happened during the topological phase transition.

(2) On the physics side, though we proposed a Magnus-type force to explain the unfolding process of the dynamic for the unfolding process (discussed in Chapter 3), however, high temperature imaging technique will give more direct evidence for the mechanism. In addition, as we know, thermal energy is critical to manipulate topological defects. One promising direction is electric field with gradient at high temperature might be able to move multiferroic vortex cores. This will give more insight to understand the analogy among multiferroic vortex, skyrmions and vortex in superconductors. Another unsolved question which is discussed in Chapter 4 is that the reason for anti-KZM in $YMnO_3$ is still unclear.

If we jump out the scope of this thesis, finding new materials based on non centrosymmetry will be technologically important, since their symmetry-dependent properties such as piezoelectricity, ferroelectricity, and nonlinear optical behavior are the basis of numerous applications. The crystallographic inter-relationships between physical properties and non-centrosymmetric crystal classes [182] are shown in Fig 6.2, which gives a guidance of developing and finding new materials. Meanwhile, the visualization, characterization and manipulation of symmetry-dependent domains and domain walls in non-centrosymmetric systems determine the most important characteristics in practical applications.

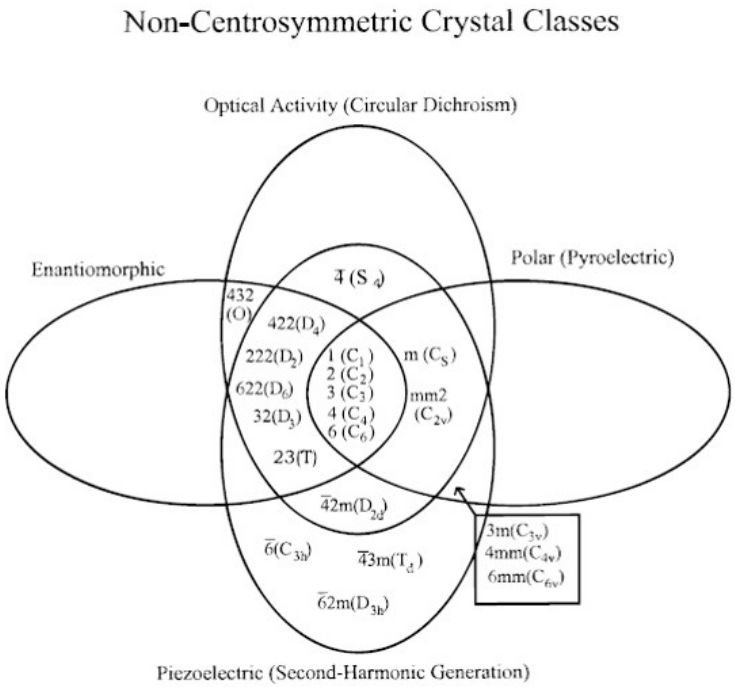

Figure 6.2: **Interrelationships of noncentrosymmetric crystal classes in both Hermann-Mauguin and Schoenflies symbols.**

Chapter 7

List of abbreviations

(h-$RMnO_3$)	hexagonal-$RMnO_3$
(0D)	0-dimensional
(1D)	1-dimensional
(2D)	2-dimensional
(3D)	3-dimensional
(AC)	Alternating Current
(OM)	Optical microscopy
(AFM)	Atomic force microscopy
(PFM)	Piezoresponse force microscopy
(MFM)	Magnetic force microscopy
(TEM)	Transmission electron microscopy
(DF-TEM)	dark-field transmission electron microscopy
(LTEM)	Lorentz transmission electron microscopy
(SEM)	Scanning electron microscope
(STEM)	Scanning-transmission electron microscopy
(HAADF-STEM)	high-angle annular-dark-field STEM
(SHG)	Second-harmonic generation
(KZM)	Kibble-Zurek Mechanism
(SOC)	Self-organized criticality
(EMO)	$ErMnO_3$
(IMO)	$InMnO_3$

(FIB)	focused-ion beam
(APB)	antiphase boundary
(PUA)	Partially undistorted anti-polar

Appendix A

Forces on vortices resulting from Lifshitz term

Consider a single domain wall connecting a vortex with an antivortex, as shown in Fig. (clearly, a domain wall cannot connect two vortices or two antivortices). At the domain wall the trimerization phase Φ increases by $\pi/3$ and we assume that $\Phi = 0$ on the right hand side of the wall beginning at the vortex and ending at the antivortex and $\Phi = \pi/3$ on the left hand side. Furthermore, we introduce local Cartesian coordinates(ξ, η), such as ξ varies along the domain wall and in the direction perpendicular to the wall, so that

$$\frac{\partial \Phi}{\partial \eta} = \frac{\pi}{3}\delta(\eta) \tag{A.1}$$

Then the Lifshitz invariant (Eq. 3.1) can be written as

$$F_{int} = -\lambda h \int \frac{d\xi d\eta}{|detJ|}[(u_{xx} - u_{yy})\partial_x \eta - 2u_{xy}\partial_y \eta]\delta(\eta) \tag{A.2}$$

$$= -\lambda h \frac{\pi}{3} \int d\xi [(u_{xx} - u_{yy})\frac{\partial_x \eta}{detJ} - 2u_{xy}\frac{\partial \eta}{detJ}] \tag{A.3}$$

Here, h is the sample thickness and J is the transformation matrix:

$$J = \begin{bmatrix} \partial_x \xi & \partial_y \eta \\ \partial_x \eta & \partial_y \xi \end{bmatrix} \tag{A.4}$$

The directions of the η and ξ axes are chosen such that the determinant of J is positive (see Fig. A.1), so that $|detJ| = detJ$.

Using the expression for the inverse transformation matrix,

$$J^{-1} = \begin{bmatrix} \partial_\xi x & \partial_\eta x \\ \partial_\eta y & \partial_\xi y \end{bmatrix} = \frac{1}{detJ} \begin{bmatrix} \partial_y \eta & -\partial_y \xi \\ -\partial_x \eta & \partial_x \xi \end{bmatrix} \tag{A.5}$$

We can then re-write F_{int} for the uniform strain in the form,

$$F_{int} = \lambda h \frac{\pi}{3} \int d\xi [(u_{xx} - u_{yy}) \partial_\xi y + 2u_{xy} \partial_\xi x] \tag{A.6}$$

$$= \lambda h \frac{\pi}{3} [(u_{xx} - u_{yy})(y_A - y_V) + 2u_{xy}(x_A - x_V)] \tag{A.7}$$

where (x_V, y_V) and (x_A, y_A) are the coordinates of the vortex and antivortex, respectively. The forces acting on vortex and antivortex are then given by

$$f_V = -\frac{\partial F_{int}}{\partial\ x_V} = -f_A = \lambda h \frac{\pi}{3} (2i_{xy}, (u_{xx} - u_{yy})) \tag{A.8}$$

The result of the action of these forces is illustrated in Fig. A.2. If, for example, $u_{xy} = 0$ and $\lambda(u_{xx} - u_{yy}) > 0$ the Magnus-type force acting on the vortex is applied along the y axis (Fig. A.2(a)). It favors vertical stripes, as shown in Fig. A.2(b). If, on the other hand, $(u_{xx} - u_{yy}) = 0$ and $\lambda u_{xy} > 0$, the force is applied the x axis (Fig. A.2(c)), resulting in horizontal stripes (Fig. A.2(d)). In both cases the sign of the phase Φ jump across the wall is such that the interaction energy F_{int} is minimal.

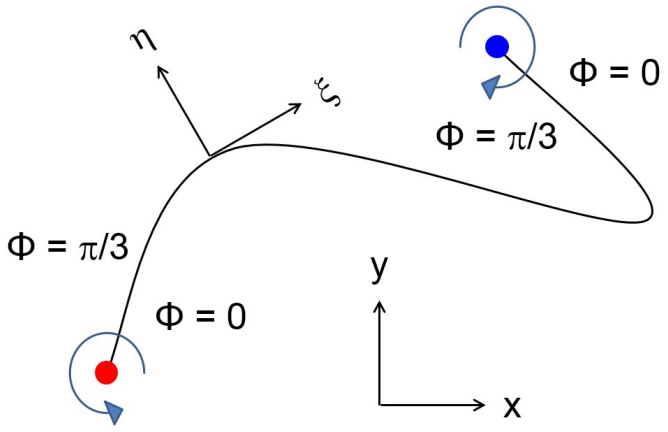

Figure A.1: **A pair of vortex and antivortex connected by a single domain wall.** The trimerization phase is labeled

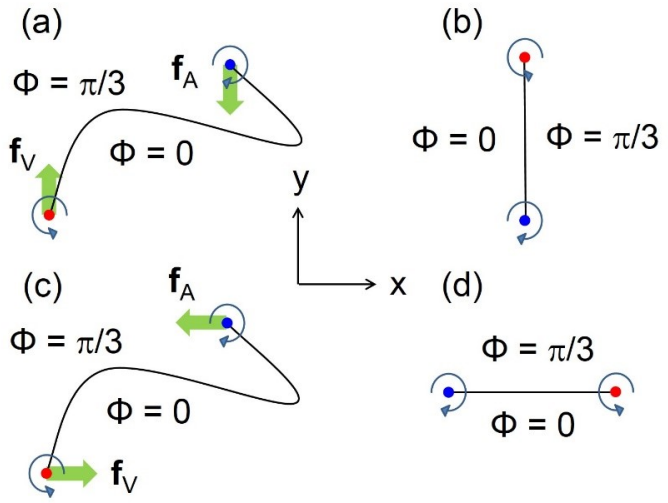

Figure A.2: **Magnus-type forces on vortex and antivortex.**(a) and (b) shows when $u_{xy} = 0$ and $\lambda(u_{xx} - u_{yy}) > 0$, the force acting on the vortex is along the y axis, resulting in vertical stripes are favored. (c) and (d) shows when $(u_{xx} - u_{yy}) = 0$ and $\lambda u_{xy} > 0$, the force is along the x axis, giving the horizontal stripes.

Appendix B

Dual theory

The local order parameter of our problem is a complex field $\phi_j = |\phi_j|e^{i\phi_j}$, that takes six possible values ($Z_2 \times Z_3$) corresponding to the even times of a clock. By assuming that the local trimerization and dipole moments develop above T_c, we neglect the amplitude ($|\phi_j|$) fluctuations near T_c. The six orientations of $|\phi_j|$ are enforced by an effective potential, $V(\phi_j) = A\cos(6\phi_j)$, which reflects the anisotropy of the underlying crystal lattice. V(ϕ_j) is dangerously irrelevant at T_c, i.e., the coarse grained action near the ferroelectric transition becomes identical to the isotropic ϕ^4 action for the normal to superfluid transition of a neutral system like ^{4}He [see Fig. 4.13(a)]:

$$H_\phi = m_\phi^2\phi^2 + u_\phi\phi^4 + (\nabla\phi)^2 \tag{B.1}$$

The superfluid to normal transition occurs via proliferation of vortex lines at $T > T_c$. The problem admits a dual description, in which the proliferation of vortex lines spanning the whole system arises from a condensation of a dual or disorder field $\psi = |\psi|e^i$ minimally coupled to an effective gauge field. Below T_c, the photon of this gauge field is the Goldstone mode of the superfluid field ϕ. This photon acquires a finite mass via the Higgs mechanism for $T > T_c$ [see Fig. 4.13(b)]. Consequently, the Biot-Savart (Coulomb) interaction between vortex segments for $T < T_c$ becomes screened (Yukawa) for $T > T_c$.

The dual description is obtained after a sequence of transformations. The original ϕ^4 theory (B1) for a neutral superfluid is first mapped into a loop gas of vortices coupled to a vector gauge field $\mathbf{A}$ generated by the smooth phase fluctuations of the original field ϕ.

The fluctuating vortex loops are then described by a disorder $|\psi|^4$ field theory in which the vortex loops correspond to supercurrents of ψ, which remain minimally coupled to $\mathbf{A}$ [155–157].

$$H_\psi = m_\psi^2\psi^2 + u_\psi\psi^4 + \frac{1}{2t}|(\nabla - iq_{eff}\mathbf{A})\psi|^{\mathbf{2}} + \frac{\mathbf{1}}{\mathbf{2}}(\nabla \times \mathbf{A})^{\mathbf{2}} \tag{B.2}$$

The constants t and q_{eff} are determined by non-universal parameters, such as the vortex core energy and the transition temperature [155–157]. Having direct experimental access to the vortex field, we can observe the Higgs condensation of ψ: the emergence of vortex lines that span the whole system above T_c implies that superfluid currents of the disorder field ψ connect opposite ends of the sample, i.e., the disorder field has condensed into a superfluid state [see Fig.4.13(b)].

Appendix C

List of $InMnO_3$ and Ga-doped $InMnO_3$ growth

A list of polycrystalline $InMnO_3$ growth is shown in Fig. C.1. A list of polycrystalline $In(Ga_xMn_{1-x})O_3$ growth is shown in Fig. C.2. A list of standard tilting growth of both is shown in Fig. C.3.

Ratio(In:Mn:Bi)	T sequence	Comments
1:1:1	950C, 77h, step	
1:1:1	970C, 150h, step Then 990C, 100h, step	
1:1:1	970C, 100h, step	
1:1:0.7	970C, 100h, step	
1:1:1.6	970C, 100h, step	Single crystal is shown in Fig. 5.1(c)
1:1:1.4	970C, 100h, step	
1:1:1.8	970C, 100h, step	
1:1:0.1	970C, 100h, step	High quality
1:1:0.05	1000C, 200h, 10C/h	Phase is not hexagonal phase
1:1:0.1	1000C, 200h, 10C/h	Phase is not hexagonal phase
1:1:0.15	1000C, 200h, 10C/h	Phase is not hexagonal phase
1:1:0.05	970C, 200h, 10C/h	High quality
1:1:0.05	970C, 200h, 10C/h	High quality
1:1:0.1	970C, 200h, 10C/h	High quality
1:1:0.1	970C, 200h, 10C/h	High quality
1:1:0.15	970C, 200h, 10C/h	3 of these are sealed Trying to make more insulating samples
1:1:0.2	970C, 200h, 10C/h	
1:1:0.25	970C, 200h, 10C/h	
1:1:0.1	980C, 400h 2C/h	Longer sintering with slower cooling
1.1:1:0.1	980C, 400h 2C/h	In excess, not good quality
1:1:0.1	980C, 200h, 10C/h	
1.1:1:0.1	980C, 200h, 10C/h	In excess, not good quality

Figure C.1: **A complete list of polycrystalline $InMnO_3$ growth.**

Ratio(In:Bi), Ga=x	T sequence	Comments
1:0.1, x=0.45	1000C, 100h, step	High quality
1:0.1, x=0.43	1000C, 200h, 10C/h	
1:0.1, x=0.47	1000C, 200h, 10C/h	
1:0.1, x=0.41	1000C, 200h, 10C/h	
1:0.1, x=0.42	1000C, 200h, 10C/h	
1:0.1, x=0.4	1000C, 200h, 10C/h	
1:0.1, x=0.3	1000C, 200h, 10C/h	
1:0.1, x=0.35	1000C, 200h, 10C/h	
1:0.1, x=0.37	1000C, 200h, 10C/h	
1:0.1, x=0.39	1000C, 200h, 10C/h	
1:0.1, x=0.1	1000C, 200h, 10C/h	
1:0.1, x=0.2	1000C, 200h, 10C/h	
1:0.03, x=0.05	1000C, 200h, 10C/h	Different Bi2O3 ratio to optimize the growth
1:0.1, x=0.05	1000C, 200h, 10C/h	
1:0.2, x=0.05	1000C, 200h, 10C/h	
1:0.1, x=0.01	1000C, 200h, 10C/h	High quality
1:0.1, x=0.02	1000C, 200h, 10C/h	
1:0.1, x=0.03	1000C, 200h, 10C/h	
1:0.1, x=0.04	1000C, 200h, 10C/h	
1:0.1, x=0.05	1000C, 200h, 10C/h	
1:0.1, x=0.02	1000C, 20h, FC Then 1000C, 200h, 10C/h (2 step)	2 step growth gives best sample
1:0.1, x=0.04	1000C, 20h, FC Then 1000C, 200h, 10C/h (2 step)	
1:1, x=0.1	1000C, 100h, fast Q	All melt, too high T
1:0.5, x=0.1	980C, 100h, 10C/h	Very small crystal, hard to extract
1:0.7, x=0.1	980C, 100h, 10C/h	
1:1, x=0.1	980C, 100h, 10C/h	
1:1, x=0.02	980C, 100h, 10C/h	3 of these are using T gradient by furnace itself, still very small crystal
1:1, x=0.02	980C, 100h, 10C/h	
1:1, x=0.02	980C, 100h, 10C/h	
1:1, x=0.01	1000C, 200h, 10C/h	Not good
1:1.3, x=0.01	1000C, 200h, 10C/h	
1:1.6, x=0.01	1000C, 200h, 10C/h	
1:1, x=0.04	1000C, 200h, 10C/h	
1:1.3, x=0.04	1000C, 200h, 10C/h	

Figure C.2: **A complete list of polycrystalline $\mathbf{In(Ga_xMn_{1-x})O_3}$.**

Growth type	Ratio(In:Mn:Bi)	T sequence	Result
Tilting InMnO3	1:1:1	1050C, 10h, 2C/h 970C,tilting	No Crystal
Tilting InMnO3	1:1:3	1080C, 10h, 2C/h 1000C, tilting	No Crystal
Tilting InMnO3	1:1:4	1150C, 10h, 2C/h 990C, tilting	No Crystal
Tilting InMnO3	1:1:6	1150C, 10h, 5C/h 990C, tilting	No Crystal
Tilting InGa0.1Mn0.9O3	1: 0.9: 0.1 : 18	1280C, 7h, 6C/h 950C, tilting	Small rectangular In2O3 crystal
Tilting InGa0.1Mn0.9O3	1: 0.9: 0.1 :6	1280C, 5h, 6.5C/h 900C, tilting	In2O3
Tilting InGa0.1Mn0.9O3	In:(Ga0.1Mn0.9): Bi = 1:2:10	1280C, 5h, 6.5C/h 900C, tilting	No crystal

Figure C.3: **A complete list of standard tilting growth of both.**

Bibliography

[1] J. Scheib, S. Gangestad, and R. Thornhill, "Facial attractiveness, symmetry and cues of good genes," *Proceedings of the Royal Society B-Biological Sciences* , vol. 266, pp. 1913–1917, SEP 22 1999.

[2] L. D. Barron, "Chirality and life," *Space Sci. Rev.*, pp. 187–201, JAN 2008.

[3] G. H. Wagnire, *Chirality and the Universal Asymmetry.* Wiley-VCH, 2007.

[4] Y. Nambu and G. Jona-Lasinio, "Dynamical model of elementary particles based on an analogy with superconductivity. i," *Phys. Rev.*, vol. 122, pp. 345–358, Apr 1961.

[5] T. D. Lee and C. N. Yang, "Question of parity conservation in weak interactions," *Phys. Rev.*, vol. 104, pp. 254–258, Oct 1956.

[6] C. S. Wu, E. Ambler, R. W. Hayward, D. D. Hoppes, and R. P. Hudson, "Experimental test of parity conservation in beta decay," *Phys. Rev.*, vol. 105, pp. 1413–1415, Feb 1957.

[7] D. B. Lichtenberg, *Unitary Symmetry and Elementary Particles.* Academic, New York, 1978.

[8] P. W. Higgs, "Broken Symmetries and the Masses of Gauge Bosons," *Phys.Rev.Lett.*, vol. 13, pp. 508–509, 1964.

[9] F. Englert and R. Brout, "Broken symmetry and the mass of gauge vector mesons," *Phys. Rev. Lett.*, vol. 13, pp. 321–323, Aug 1964.

[10] G. S. Guralnik, C. R. Hagen, and T. W. B. Kibble, "Global conservation laws and massless particles," *Phys. Rev. Lett.*, vol. 13, pp. 585–587, Nov 1964.

[11] T. W. B. Kibble, "Topology of cosmic domains and strings," *Journal of Physics A: Mathematical and General*, vol. 9, no. 8, p. 1387, 1976.

[12] M. Cruz, N. Turok, P. Vielva, E. Martinez-Gonzalez, and M. Hobson, "A cosmic microwave background feature consistent with a cosmic texture," *Science*, vol. 318, pp. 1612–1614, DEC 7 2007.

[13] G. Blatter, M. V. Feigel'man, V. B. Geshkenbein, A. I. Larkin, and V. M. Vinokur, "Vortices in high-temperature superconductors," *Rev. Mod. Phys.*, vol. 66, pp. 1125–1388, Oct 1994.

[14] A. S. Sidorkin, *Domain Structure in Ferroelectrics and Related Materials*. Cambridge University Press, 2006.

[15] C. H. A. Karin M Rabe, Jean-Marc Triscone, *Physics of Ferroelectrics: A modern perspective*. Springer, 2007.

[16] D. Jiles, *Introduction to magnetism and magnetic materials*. London: Chapman & Hall, 1998.

[17] T. H. R. Skyrme, "A unified field theory of mesons and baryons," *Nucl. Phys.*, vol. 31, pp. 556–569, 1962.

[18] J. Valasek, "Piezo-electric and allied phenomena in rochelle salt," *Phys. Rev.*, vol. 17, pp. 475–481, Apr 1921.

[19] J. Scott and C. Dearaujo, "Ferroelectric memories," *Science*, vol. 246, pp. 1400–1405, DEC 15 1989.

[20] N. Hur, S. Park, P. Sharma, J. Ahn, S. Guha, and S. Cheong, "Electric polarization

reversal and memory in a multiferroic material induced by magnetic fields," *Nature*, vol. 429, pp. 392–395, MAY 27 2004.

[21] G. Catalan and J. F. Scott, "Physics and Applications of Bismuth Ferrite," *Advanced Materials*, vol. 21, pp. 2463–2485, JUN 26 2009.

[22] O. Auciello, J. Scott, and R. Ramesh, "The physics of ferroelectric memories," *Physics Today*, vol. 51, pp. 22–27, JUL 1998.

[23] J. F. Scott, "Applications of modern ferroelectrics," *Science*, vol. 315, pp. 954–959, FEB 16 2007.

[24] Martienssen, *Springer Handbook of Condensed Matter and Materials Data*. Springer, 2005.

[25] R. Naber, C. Tanase, P. Blom, G. Gelinck, A. Marsman, F. Touwslager, S. Setayesh, and D. De Leeuw, "High-performance solution-processed polymer ferroelectric field-effect transistors," *Nature Materials*, vol. 4, pp. 243–248, MAR 2005.

[26] M. Dawber, K. M. Rabe, and J. F. Scott, "Physics of thin-film ferroelectric oxides," *Rev. Mod. Phys.*, vol. 77, pp. 1083–1130, Oct 2005.

[27] S. Mathews, R. Ramesh, T. Venkatesan, and J. Benedetto, "Ferroelectric field effect transistor based on epitaxial perovskite heterostructures," *Science*, vol. 276, pp. 238–240, APR 11 1997.

[28] S. Millers and P. Mcwhorter, "Physics of The Ferroelectric Nonvolatile Memory Field-effect Transitor," *Jorunal of Applied Physics*, vol. 72, pp. 5999–6010, DEC 15 1992.

[29] G. M. G. B. M. Vula and I. I. Ivanchika, "Encountering domains in ferroelectrics," *Ferroelectrics*, vol. 6, pp. 29–31, 1973.

[30] W. J. Merz, "Domain formation and domain wall motions in ferroelectric batio$_3$ single crystals," *Phys. Rev.*, vol. 95, pp. 690–698, Aug 1954.

[31] Y. Du, X. L. Wang, D. P. Chen, S. X. Dou, Z. X. Cheng, M. Higgins, G. Wallace, and J. Y. Wang, "Domain wall conductivity in oxygen deficient multiferroic $YMnO_3$ single crystals," *Applied Physics Letters*, vol. 99, p. 252107, DEC 19 2011.

[32] J. Seidel, L. W. Martin, Q. He, Q. Zhan, Y. H. Chu, A. Rother, M. E. Hawkridge, P. Maksymovych, P. Yu, M. Gajek, N. Balke, S. V. Kalinin, S. Gemming, F. Wang, G. Catalan, J. F. Scott, N. A. Spaldin, J. Orenstein, and R. Ramesh, "Conduction at domain walls in oxide multiferroics," *Nature Materials*, vol. 8, pp. 229–234, MAR 2009.

[33] R. K. Vasudevan, W. Wu, J. R. Guest, A. P. Baddorf, A. N. Morozovska, E. A. Eliseev, N. Balke, V. Nagarajan, P. Maksymovych, and S. V. Kalinin, "Domain Wall Conduction and Polarization-Mediated Transport in Ferroelectrics," *Advanced Functional Materials*, vol. 23, pp. 2592–2616, MAY 28 2013.

[34] W. J. Merz, "Domain formation and domain wall motions in ferroelectric batio$_3$ single crystals," *Phys. Rev.*, vol. 95, pp. 690–698, Aug 1954.

[35] T. Sluka, A. K. Tagantsev, P. Bednyakov, and N. Setter, "Free-electron gas at charged domain walls in insulating $BaTiO_3$," *Nature Communications*, vol. 4, MAY 2013.

[36] A. P. Levanyuk and D. G. Sannikov, "Improper ferroelectrics," *Soviet Physics Uspekhi*, vol. 17, no. 2, p. 199, 1974.

[37] M. Kenzelmann, A. B. Harris, S. Jonas, C. Broholm, J. Schefer, S. B. Kim, C. L. Zhang, S.-W. Cheong, O. P. Vajk, and J. W. Lynn, "Magnetic Inversion Symmetry Breaking and Ferroelectricity in $TbMnO_3$," *Phys. Rev. Lett.*, vol. 95, p. 087206, Aug 2005.

[38] T. Goto, T. Kimura, G. Lawes, A. P. Ramirez, and Y. Tokura, "Ferroelectricity and giant magnetocapacitance in perovskite rare-earth manganites," *Phys. Rev. Lett.*, vol. 92, p. 257201, Jun 2004.

[39] N. A. Benedek and C. J. Fennie, "Hybrid improper ferroelectricity: A mechanism for controllable polarization-magnetization coupling," *Phys. Rev. Lett.*, vol. 106, p. 107204, Mar 2011.

[40] J. M. Rondinelli and C. J. Fennie, "Octahedral Rotation-Induced Ferroelectricity in Cation Ordered Perovskites," *Advanced Materials*, vol. 24, pp. 1961–1968, APR 17 2012.

[41] Y. S. O. X. L. F. T. H. Y. Wang and S.-W. Cheong, "Experimental demonstration of hybrid improper ferroelectricity and the presence of abundant charged walls in $(Ca,Sr)_3Ti_2O_7$ crystals," *Nature Materials*, JAN 2015.

[42] M. Lobanov, M. Greenblatt, E. Caspi, J. Jorgensen, D. Sheptyakov, B. Toby, C. Botez, and P. Stephens, "Crystal and magnetic structure of the $Ca_3Mn_2O_7$ Ruddlesden-Popper phase: neutron and synchrotron x-ray diffraction study," *Journal of Physics-Condensed Matter*, vol. 16, pp. 5339–5348, JUL 28 2004.

[43] S. Senn, M. A. Bombardi, A. Murray, C. C. Vecchini, A. Scherillo, X. Luo, and W. Cheong, S. "Negative thermal expansion in hybrid improper ferroelectric ruddlesden-popper perovskites by symmetry trapping," *Phys. Rev. Lett.*, vol. 114, p. 035701, Jan 2015.

[44] M. J. Pitcher, P. Mandal, M. S. Dyer, J. Alaria, P. Borisov, H. Niu, J. B. Claridge, and M. J. Rosseinsky, "Tilt engineering of spontaneous polarization and magnetization above 300 k in a bulk layered perovskite," *Science*, vol. 347, no. 6220, pp. 420–424, 2015.

[45] N. Spaldin and M. Fiebig, "The renaissance of magnetoelectric multiferroics," *Science*, vol. 309, pp. 391–392, JUL 15 2005.

[46] S.-W. Cheong and M. Mostovoy, "Multiferroics: a magnetic twist for ferroelectricity," *Nature Materials*, vol. 6, pp. 13–20, JAN 2007.

[47] N. A. Spaldin, S.-W. Cheong, and R. Ramesh, "Multiferroics: Past, present, and future," *Pysics Today*, vol. 63, pp. 38–43, OCT 2010.

[48] T. Choi, Y. Horibe, H. T. Yi, Y. J. Choi, W. Wu, and S. W. Cheong, "Insulating interlocked ferroelectric and structural antiphase domain walls in multiferroic $YMnO_3$," *Nature Materials*, vol. 9, pp. 253–258, MAR 2010.

[49] N. Lee, Y. J. Choi, M. Ramazanoglu, W. Ratcliff, V. Kiryukhin, and S.-W. Cheong, "Mechanism of exchange striction of ferroelectricity in multiferroic orthorhombic $HoMnO_3$ single crystals," *Phys. Rev. B*, vol. 84, p. 020101, Jul 2011.

[50] R. C. Pullar, "Hexagonal ferrites: A review of the synthesis, properties and applications of hexaferrite ceramics," *Progress in Materials Science*, vol. 57, pp. 1191–1334, SEP 2012.

[51] H. Das, A. L. Wysocki, Y. Geng, W. Wu, and C. J. Fennie, "Bulk magnetoelectricity in the hexagonal manganites and ferrites," *Nature Communications*, vol. 5, JAN 2014.

[52] W. Wang, J. Zhao, W. Wang, Z. Gai, N. Balke, M. Chi, H. N. Lee, W. Tian, L. Zhu, X. Cheng, D. J. Keavney, J. Yi, T. Z. Ward, P. C. Snijders, H. M. Christen, W. Wu, J. Shen, and X. Xu, "Room-temperature multiferroic hexagonal lufeo$_3$ films," *Phys. Rev. Lett.*, vol. 110, p. 237601, Jun 2013.

[53] S. A. Pikin and I. S. Lyubutin, "Phenomenological model of multiferroic properties in langasite-type crystals with a triangular magnetic lattice," *Phys. Rev. B*, vol. 86, p. 064414, Aug 2012.

[54] I. S. Lyubutin, P. G. Naumov, B. V. Mill', K. V. Frolov, and E. I. Demikhov, "Structural and magnetic properties of the iron-containing langasite family $A_3M\mathrm{Fe}_3X_2\mathrm{O}_{14}$ (A = Ba, Sr; M = Sb, Nb, Ta; X = Si, Ge) observed by Mössbauer spectroscopy," *Phys. Rev. B*, vol. 84, p. 214425, Dec 2011.

[55] N. Lee, Y. J. Choi, and S.-W. Cheong, "Magnetic control of ferroelectric polarization in a self-formed single magnetoelectric domain of multiferroic $Ba_3NbFe_3Si_2O_{14}$," *Applied Phyiscs Letters*, vol. 104, FEB 17 2014.

[56] S. Park, Y. J. Choi, C. L. Zhang, and S.-W. Cheong, "Ferroelectricity in an $S = 1/2$ Chain Cuprate," *Phys. Rev. Lett.*, vol. 98, p. 057601, Jan 2007.

[57] Y. J. Choi, H. T. Yi, S. Lee, Q. Huang, V. Kiryukhin, and S.-W. Cheong, "Ferroelectricity in an ising chain magnet," *Phys. Rev. Lett.*, vol. 100, p. 047601, Jan 2008.

[58] T. Kimura, J. C. Lashley, and A. P. Ramirez, "Inversion-symmetry breaking in the noncollinear magnetic phase of the triangular-lattice antiferromagnet $CuFeO_2$," *Phys. Rev. B*, vol. 73, p. 220401, Jun 2006.

[59] R. D. Johnson, L. C. Chapon, D. D. Khalyavin, P. Manuel, P. G. Radaelli, and C. Martin, "Giant Improper Ferroelectricity in the Ferroaxial Magnet $CaMn_7O_{12}$," *Phys. Rev. Lett.*, vol. 108, p. 067201, Feb 2012.

[60] G. Zhang, S. Dong, Z. Yan, Y. Guo, Q. Zhang, S. Yunoki, E. Dagotto, and J.-M. Liu, "Multiferroic properties of $CaMn_7O_{12}$," *Phys. Rev. B*, vol. 84, p. 174413, Nov 2011.

[61] N. D. Mermin, "The topological theory of defects in ordered media," *Rev. Mod. Phys.*, vol. 51, pp. 591–648, Jul 1979.

[62] J. P. Sethna, *Statistical Mechanics: Entropy, Order Parameters, and Complexity.* Oxford University Press, 2006.

[63] A. Vilenkin and E. P. S. Shellard, *Cosmic Strings and Other Topological Defects.* Cambridge Univ. Press,, 1994.

[64] H. E. Stanley, "Dependence of critical properties on dimensionality of spins," *Phys. Rev. Lett.*, vol. 20, pp. 589–592, Mar 1968.

[65] G. S. Grest and D. J. Srolovitz, "Vortex effects on domain growth: The clock model," *Phys. Rev. B*, vol. 30, pp. 6535–6539, Dec 1984.

[66] S.-Z. Lin, X. Wang, Y. Kamiya, G.-W. Chern, F. Fan, D. Fan, B. Casas, Y. Liu, V. Kiryukhin, W. H. Zurek, C. D. Batista, and S.-W. Cheong, "Topological defects as relics of emergent continuous symmetry and higgs condensation of disorder in ferroelectrics," *Nat Phys*, vol. 10, pp. 970–977, Dec 2014.

[67] S. Muehlbauer, B. Binz, F. Jonietz, C. Pfleiderer, A. Rosch, A. Neubauer, R. Georgii, and P. Boeni, "Skyrmion Lattice in a Chiral Magnet," *Sciece*, vol. 323, pp. 915–919, FEB 13 2009.

[68] X. Z. Yu, Y. Onose, N. Kanazawa, J. H. Park, J. H. Han, Y. Matsui, N. Nagaosa, and Y. Tokura, "Real-space observation of a two-dimensional skyrmion crystal," *Nature*, vol. 465, pp. 901–904, JUN 17 2010.

[69] W. Munzer, A. Neubauer, T. Adams, S. Muhlbauer, C. Franz, F. Jonietz, R. Georgii, P. Boni, B. Pedersen, M. Schmidt, A. Rosch, and C. Pfleiderer, "Skyrmion lattice in the doped semiconductor $Fe_{1-x}Co_xSi$," *Phys. Rev. B*, vol. 81, p. 041203, Jan 2010.

[70] X. Z. Yu, N. Kanazawa, Y. Onose, K. Kimoto, W. Z. Zhang, S. Ishiwata, Y. Matsui, and Y. Tokura, "Near room-temperature formation of a skyrmion crystal in thin-films of the helimagnet FeGe," *Nature Materials*, vol. 10, pp. 106–109, FEB 2011.

[71] S. L. Sondhi, A. Karlhede, S. A. Kivelson, and E. H. Rezayi, "Skyrmions and the crossover from the integer to fractional quantum hall effect at small zeeman energies," *Phys. Rev. B*, vol. 47, pp. 16419–16426, Jun 1993.

[72] D. C. Wright and N. D. Mermin, "Crystalline liquids: the blue phases," *Rev. Mod. Phys.*, vol. 61, pp. 385–432, Apr 1989.

[73] T.-L. Ho, "Spinor bose condensates in optical traps," *Phys. Rev. Lett.*, vol. 81, pp. 742–745, Jul 1998.

[74] A. Fert, V. Cros, and J. Sampaio, "Skyrmions on the track," *Nature Nanotechnology*, vol. 8, pp. 152–156, MAR 2013.

[75] C. Pfleiderer, "Magnetic order: Surfaces get hairy," *Nature Physics*, vol. 7, pp. 673–674, SEP 2011.

[76] J. S. White, I. Levatic, A. A. Omrani, N. Egetenmeyer, K. Prsa, I. Zivkovic, J. L. Gavilano, J. Kohlbrecher, M. Bartkowiak, H. Berger, and H. M. Ronnow, "Electric field control of the skyrmion lattice in Cu_2OSeO_3," *Journal of Physics-Condensed Matter*, vol. 24, OCT 31 2012.

[77] S.-Z. Lin, C. D. Batista, C. Reichhardt, and A. Saxena, "ac current generation in chiral magnetic insulators and skyrmion motion induced by the spin seebeck effect," *Phys. Rev. Lett.*, vol. 112, p. 187203, May 2014.

[78] L. Kong and J. Zang, "Dynamics of an insulating skyrmion under a temperature gradient," *Phys. Rev. Lett.*, vol. 111, p. 067203, Aug 2013.

[79] P. Milde, D. Koehler, J. Seidel, L. M. Eng, A. Bauer, A. Chacon, J. Kindervater, S. Muehlbauer, C. Pfleiderer, S. Buhrandt, C. Schuette, and A. Rosch, "Unwinding of a Skyrmion Lattice by Magnetic Monopoles," *Science*, vol. 340, pp. 1076–1080, MAY 31 2013.

[80] T. Jungk, k. Hoffmann, M. Fiebig, and E. Soergel, "Electrostatic topology of ferroelectric domains in $YMnO_3$," *Applied Physics Letters*, vol. 97, no. 1, p. 012904, 2010.

[81] R. Gevers, H. Blank, and S. Amelinckx, "Extension of the howie-whelan equations for electron diffraction to non-centro symmetrical crystals," *physica status solidi (b)*, vol. 13, no. 2, pp. 449–465, 1966.

[82] M. Tanaka and G. Honjo, "Electron optical studies of barium titanate single crystal films," *Journal of the Physical Society of Japan*, vol. 19, no. 6, pp. 954–970, 1964.

[83] W. Wang, Y. Geng, and W. Wu, "Background-free piezoresponse force microscopy for quantitative measurements," *Applied Physics Letters*, vol. 104, no. 7, p. 072905, 2014.

[84] T. Jungk, k. Hoffmann, and E. Soergel, "Quantitative analysis of ferroelectric domain imaging with piezoresponse force microscopy," *Applied Physics Letters*, vol. 89, no. 16, p. 163507, 2006.

[85] Y. Geng and W. Wu, "Magnetoelectric force microscopy based on magnetic force microscopy with modulated electric field," *Rev. Sci. Instrum*, vol. 85, p. 053901, MAY 2014.

[86] Y. Geng, N. Lee, Y. J. Choi, S.-W. Cheong, and W. Wu, "Collective magnetism at multiferroic vortex domain walls," *Nano Letters*, vol. 12, no. 12, pp. 6055–6059, 2012.

[87] D. Meier, J. Seidel, A. Cano, K. Delaney, Y. Kumagai, M. Mostovoy, N. A. Spaldin, R. Ramesh, and M. Fiebig, "Anisotropic conductance at improper ferroelectric domain walls," *Nature Materials*, vol. 11, pp. 284–288, APR 2012.

[88] Y. Geng, H. Das, A. L. Wysocki, X. Wang, S.-W. Cheong, M. Mostovoy, C. J. Fennie, and W. Wu, "Direct visualization of magnetoelectric domains," *Nature Materials*, vol. 13, pp. 163–167, FEB 2014.

[89] C. Fan, Z. Y. Zhao, J. D. Song, J. C. Wu, F. B. Zhang, and X. F. Sun, "Single crystal growth of the hexagonal manganites $RMnO_3$(R = rare earth) by the optical floating-zone method," *Journal of Crystal Growth*, vol. 388, pp. 54–60, FEB 2015.

[90] Z. Yan, D. Meier, J. Schaab, R. Ramesh, E. Samulon, and E. Bourret, "Growth of high-quality hexagonal $ErMnO_3$ single crystals by the pressurized floating-zone method," *Journal of Crystal Growth*, vol. 409, pp. 75–79, JAN 1 2015.

[91] S. C. Chae, N. Lee, Y. Horibe, M. Tanimura, S. Mori, B. Gao, S. Carr, and S.-W.

Cheong, "Direct observation of the proliferation of ferroelectric loop domains and vortex-antivortex pairs," *Phys. Rev. Lett.*, vol. 108, p. 167603, Apr 2012.

[92] Y. Aikawa, T. Katsufuji, T. Arima, and K. Kato, "Effect of mn trimerization on the magnetic and dielectric properties of hexagonal $ymno_3$," *Phys. Rev. B*, vol. 71, p. 184418, May 2005.

[93] T. Katsufuji, M. Masaki, A. Machida, M. Moritomo, K. Kato, E. Nishibori, M. Takata, M. Sakata, K. Ohoyama, K. Kitazawa, and H. Takagi, "Crystal structure and magnetic properties of hexagonal $R\mathrm{MnO}_3 (R = \mathrm{Y}$, Lu, and Sc) and the effect of doping," *Phys. Rev. B*, vol. 66, p. 134434, Oct 2002.

[94] T. Lonkai, D. G. Tomuta, U. Amann, J. Ihringer, R. W. A. Hendrikx, D. M. Többens, and J. A. Mydosh, "Development of the high-temperature phase of hexagonal manganites," *Phys. Rev. B*, vol. 69, p. 134108, Apr 2004.

[95] K. ukaszewicz and J. Karut-Kaliciska, "X-Ray investigations of the crystal structure and phase transitions of YMnO_3," *Ferroelectrics*, vol. 7, no. 1, pp. 81–82, 1974.

[96] T. Katsufuji, S. Mori, M. Masaki, Y. Moritomo, N. Yamamoto, and H. Takagi, "Dielectric and magnetic anomalies and spin frustration in hexagonal RMnO_3 (R=Y, Yb, and Lu)," *Phys. Rev. B*, vol. 64, p. 104419, Aug 2001.

[97] C. J. Fennie and K. M. Rabe, "Ferroelectric transition in YMnO_3 from first principles," *Phys. Rev. B*, vol. 72, p. 100103, Sep 2005.

[98] W. Wu, Y. Horibe, N. Lee, S.-W. Cheong, and J. R. Guest, "Conduction of topologically protected charged ferroelectric domain walls," *Phys. Rev. Lett.*, vol. 108, p. 077203, Feb 2012.

[99] Y. Yu, X. Zhang, Y. G. Zhao, N. Jiang, R. Yu, J. W. Wang, C. Fan, X. F. Sun, and J. Zhu, "Atomic-scale study of topological vortex-like domain pattern in multiferroic hexagonal manganites," *Applied Physics Letters*, vol. 103, p. 032901, JUL 2013.

[100] Q. H. Zhang, L. J. Wang, X. K. Wei, R. C. Yu, L. Gu, A. Hirata, M. W. Chen, C. Q. Jin, Y. Yao, Y. G. Wang, and X. F. Duan, "Direct observation of interlocked domain walls in hexagonal $RMnO_3$ (R=Tm, Lu)," *Phys. Rev. B*, vol. 85, p. 020102, Jan 2012.

[101] S. Artyukhin, K. T. Delaney, N. A. Spaldin, and M. Mostovoy, "Landau theory of topological defects in multiferroic hexagonal manganites," *Nature Materials*, vol. 13, pp. 42–49, JAN 2014.

[102] S. M. Griffin, M. Lilienblum, K. T. Delaney, Y. Kumagai, M. Fiebig, and N. A. Spaldin, "Scaling behavior and beyond equilibrium in the hexagonal manganites," *Phys. Rev. X*, vol. 2, p. 041022, Dec 2012.

[103] S. C. Chae, Y. Horibe, D. Y. Jeong, S. Rodan, N. Lee, and S. W. Cheong, "Self-organization, condensation, and annihilation of topological vortices and antivortices in a multiferroic," *Proceedings of the National Academy of Science of The United States of America*, vol. 107, pp. 21366–21370, DEC 14 2010.

[104] S. C. Chae, Y. Horibe, D. Y. Jeong, N. Lee, K. Iida, M. Tanimura, and S.-W. Cheong, "Evolution of the domain topology in a ferroelectric," *Phys. Rev. Lett.*, vol. 110, p. 167601, Apr 2013.

[105] D. Muller, N. Nakagawa, A. Ohtomo, J. Grazul, and H. Hwang, "Atomic-scale imaging of nanoengineered oxygen vacancy profiles in $SrTiO_3$," *Nature*, vol. 430, pp. 657–661, AUG 5 2004.

[106] K. Szot, W. Speier, G. Bihlmayer, and R. Waser, "Switching the electrical resistance of individual dislocations in single-crystalline $SrTiO_3$," *Nature Materials*, vol. 5, pp. 312–320, APR 2006.

[107] L. HUANG and N. JAEGER, "Discussion of Domain Inversion in $LiNbO_3$," *Applied Physics Letters*, vol. 65, pp. 1763–1765, OCT 3 1994.

[108] M. Schroeder, A. Haussmann, A. Thiessen, E. Soergel, T. Woike, and L. M. Eng, "Conducting Domain Walls in Lithium Niobate Single Crystals," *Advanced Fuctional Materials*, vol. 22, pp. 3936–3944, SEP 25 2012.

[109] V. Gopalan, T. Mitchell, Y. Furukawa, and K. Kitamura, "The role of nonstoichiometry in 180 degrees domain switching of $LiNbO_3$ crystals," *Applied Physics Letters*, vol. 72, pp. 1981–1983, APR 20 1998.

[110] R. V. Wang, D. D. Fong, F. Jiang, M. J. Highland, P. H. Fuoss, C. Thompson, A. M. Kolpak, J. A. Eastman, S. K. Streiffer, A. M. Rappe, and G. B. Stephenson, "Reversible chemical switching of a ferroelectric film," *Phys. Rev. Lett.*, vol. 102, p. 047601, Jan 2009.

[111] J. R. Sahu, A. Ghosh, A. Sundaresan, and C. N. R. Rao, "Multiferroic properties of $ErMnO_3$," *Materials Research Bulletin*, vol. 44, pp. 2123–2126, NOV 2009.

[112] S. Strogatz, "Exploring complex networks," *Nature*, vol. 410, pp. 268–276, MAR 8 2001.

[113] R. Albert and A.-L. Barabási, "Statistical mechanics of complex networks," *Rev. Mod. Phys.*, vol. 74, pp. 47–97, Jan 2002.

[114] M. Newman, "The structure and function of complex networks," *SIAM Review*, vol. 45, pp. 167–256, JUN 2003.

[115] R. Cohen and S. Havlin, "Scale-free networks are ultrasmall," *Phys. Rev. Lett.*, vol. 90, p. 058701, Feb 2003.

[116] S. N. Dorogovtsev, A. V. Goltsev, and J. F. F. Mendes, "Critical phenomena in complex networks," *Rev. Mod. Phys.*, vol. 80, pp. 1275–1335, Oct 2008.

[117] L. Amaral, A. Scala, M. Barthelemy, and H. Stanley, "Classes of small-world networks," *Proceedings of the National Academy of Science of The United States of America*, vol. 97, pp. 11149–11152, OCT 10 2000.

[118] R. Albert, I. Albert, and G. L. Nakarado, "Structural vulnerability of the north american power grid," *Phys. Rev. E*, vol. 69, p. 025103, Feb 2004.

[119] K.-I. Goh, D.-S. Lee, B. Kahng, and D. Kim, "Sandpile on scale-free networks," *Phys. Rev. Lett.*, vol. 91, p. 148701, Oct 2003.

[120] L. Chen, "Phase-field models for microstructure evolution," *Annual Review of Materials Research*, vol. 32, pp. 113–140, 2002.

[121] B. Mettout, P. Toledano, M. Lilienblum, and M. Fiebig, "Combinatorial model for the ferroelectric domain-network formation in hexagonal manganites," *Phys. Rev. B*, vol. 89, p. 024103, JAN 13 2014.

[122] Y. Yu, X. Zhang, Y. G. Zhao, N. Jiang, R. Yu, J. W. Wang, C. Fan, X. F. Sun, and J. Zhu, "Atomic-scale study of topological vortex-like domain pattern in multiferroic hexagonal manganites," *Applied Physics Letters*, vol. 103, p. 032901, JUL 15 2013.

[123] Q.-H. Zhang, G.-T. Tan, L. Gu, Y. Yao, C.-Q. Jin, Y.-G. Wang, X.-F. Duan, and R.-C. Yu, "Topology breaking of the vortex in multiferroic $Y_{0.67}Lu_{0.33}MnO_3$," *Applied Physics Letters*, vol. 105, p. 012902, JUL 7 2014.

[124] Y. Du, X. Wang, D. Chen, Y. Yu, W. Hao, Z. Cheng, and S. X. Dou, "Manipulation of domain wall mobility by oxygen vacancy ordering in multiferroic $YMnO_3$," *Physical Chemistry Chemical Physics*, vol. 15, no. 46, pp. 20010–20015, 2013.

[125] Y. Kumagai and N. A. Spaldin, "Structural domain walls in polar hexagonal manganites," *Nature Communications*, vol. 4, p. 1540, FEB 2013.

[126] N. D. Mermin, "The topological theory of defects in ordered media," *Rev. Mod. Phys.*, vol. 51, pp. 591–648, Jul 1979.

[127] J. Bardeen and M. J. Stephen, "Theory of the motion of vortices in superconductors," *Phys. Rev.*, vol. 140, pp. A1197–A1207, Nov 1965.

[128] S.-Z. Lin, C. Reichhardt, C. D. Batista, and A. Saxena, "Particle model for skyrmions in metallic chiral magnets: Dynamics, pinning, and creep," *Phys. Rev. B*, vol. 87, p. 214419, Jun 2013.

[129] J. Iwasaki, M. Mochizuki, and N. Nagaosa, "Universal current-velocity relation of skyrmion motion in chiral magnets," *Nature Communications*, vol. 4, FEB 2013.

[130] E. B. Sonin, "Magnus force in superfluids and superconductors," *Phys. Rev. B*, vol. 55, pp. 485–501, Jan 1997.

[131] A. S. Logginov, A. V. Meshkov, G. A.and Nikolaev, E. P. Nikolaeva, A. P. Pyatakov, and A. K. Zvezdin, "Roomtemperature magnetoelectric control of micromagnetic structure in iron garnet films," *Applied Physics Letters*, vol. 93, p. 182510, NOV 3 2008.

[132] M.-G. Han, Y. Zhu, L. Wu, T. Aoki, V. Volkov, X. Wang, S. C. Chae, Y. S. Oh, and S.-W. Cheong, "Ferroelectric Switching Dynamics of Topological Vortex Domains in a Hexagonal Manganite," *Advanced Materials*, vol. 25, pp. 2415–2421, MAY 7 2013.

[133] G. Catalan, J. Seidel, R. Ramesh, and J. F. Scott, "Domain wall nanoelectronics," *Rev. Mod. Phys.*, vol. 84, pp. 119–156, Feb 2012.

[134] A. P. Levanyuk, S. A. Minyukov, and A. Cano, "Universal mechanism of discontinuity of commensurate-incommensurate transitions in three-dimensional solids: Strain dependence of soliton self-energy," *Phys. Rev. B*, vol. 66, p. 014111, Jul 2002.

[135] A. Cano, A. P. Levanyuk, and S. A. Minyukov, "Elasticity-driven interaction between vortices in type-ii superconductors," *Phys. Rev. B*, vol. 68, p. 144515, Oct 2003.

[136] P. Miranović, L. Dobrosavljević-Grujić, and V. G. Kogan, "Ginzburg-landau theory of vortex lattice structure in deformable anisotropic superconductors," *Phys. Rev. B*, vol. 52, pp. 12852–12857, Nov 1995.

[137] L. D. Landau and E. M. Lifshitz, *Theory of Elasticity.* Pergamon, Oxford, 1986.

[138] T. Kibble, "Phase-transition dynamics in the lab and the universe," *Physics Today*, vol. 60, pp. 47–52, SEP 2007.

[139] W. Zurek, "Cosmological experiments in superfluid-helium," *Nature*, vol. 317, no. 6037, pp. 505–508, 1985.

[140] A. del Campo and W. H. Zurek, "Universality of phase transition dynamics: Topological defects from symmetry breaking," *International Journal of Modern Physics A*, vol. 29, MAR 30 2014.

[141] M. Campostrini, M. Hasenbusch, A. Pelissetto, P. Rossi, and E. Vicari, "Critical behavior of the three-dimensional XY universality class," *Phys. Rev. B*, vol. 63, p. 214503, May 2001.

[142] P. C. Hohenberg and B. I. Halperin, "Theory of dynamic critical phenomena," *Rev. Mod. Phys.*, vol. 49, pp. 435–479, Jul 1977.

[143] D. Blankschtein, M. Ma, A. N. Berker, G. S. Grest, and C. M. Soukoulis, "Orderings of a stacked frustrated triangular system in three dimensions," *Phys. Rev. B*, vol. 29, pp. 5250–5252, May 1984.

[144] M. Oshikawa, "Ordered phase and scaling in Z_n models and the three-state antiferromagnetic potts model in three dimensions," *Phys. Rev. B*, vol. 61, pp. 3430–3434, Feb 2000.

[145] H.-B. Braun, "Topological effects in nanomagnetism: from superparamagnetism to chiral quantum solitons," *Advances in Physics*, vol. 61, no. 1, pp. 1–116, 2012.

[146] W. H. Zurek, "Topological relics of symmetry breaking: winding numbers and scaling tilts from random vortex-antivortex pairs," *Journal of Physics-Condensed Matter*, vol. 25, OCT 9 2013.

[147] S. R. Shenoy and B. Chattopadhyay, "Anisotropic three-dimensional XY model and vortex-loop scaling," *Phys. Rev. B*, vol. 51, pp. 9129–9147, Apr 1995.

[148] D. Dominguez, N. Grnbech-Jensen, A. R. Bishop, and S. R. Shenoy, "Transformer configuration in three dimensional josephson lattices at zero magnetic field," *Phys. Rev. Lett.*, vol. 75, pp. 717–720, Jul 1995.

[149] M. Kiometzis, H. Kleinert, and A. M. J. Schakel, "Critical exponents of the superconducting phase transition," *Phys. Rev. Lett.*, vol. 73, pp. 1975–1977, Oct 1994.

[150] A. K. Nguyen and A. Sudb, "Onsager loop transition and first-order flux-line lattice melting in high-T_c superconductors," *Phys. Rev. B*, vol. 57, pp. 3123–3143, Feb 1998.

[151] S. Ryu and D. Stroud, "Nature of the low-field transition in the mixed state of high-temperature superconductors," *Phys. Rev. B*, vol. 57, pp. 14476–14497, Jun 1998.

[152] D. Golubchik, E. Polturak, and G. Koren, "Evidence for Long-Range Correlations within Arrays of Spontaneously Created Magnetic Vortices in a Nb Thin-Film Superconductor," *Phys. Rev. Lett.*, vol. 104, p. 247002, Jun 2010.

[153] R. Feynman, *Progress in Low Temperature Physics Vol. I.* North-Holland, 1955.

[154] L. Onsager, "The two fluid model for helium II," *Il Nuovo Cimento Series 9*, vol. 6, pp. 249–250, Sep 1949.

[155] H. Kleinert, *Gauge Fields in Condensed Matter.* World Scientific Publishing, Singapore, 1989.

[156] H. Kleinert, "From Landau's Order Parameter to Modern Disorder Fields," in *Sun, The stars, The universe, and General Relativity* (Ruffini, R and Vereshchagin, G, ed.), vol. 1205 of *AIP Conference Proceedings*, pp. 103–107, Belarusian State Univ; Cent European Initiat; Int Ctr Relativist Astrophys Network; Int Ctr Theoret Phys, 2010. International Meeting on the Sun, the Stars, the Universe, and General Relativity held in Honor of Ya B Zeldovich's 95th Anniversary, Minsk, BYELARUS, APR 20-23, 2009.

[157] M. Kiometzis, H. Kleinert, and A. Schakel, "Dual description of the superconducting phase transition," *Fortschritte Der Physik-Progress of Physics*, vol. 43, no. 8, pp. 697–732, 1995.

[158] I. Chuang, R. Durrer, N. Turok, and B. Yurke, "Cosmology in the laboratory - Defect dynamics in liquid-crystals," *Science*, vol. 251, pp. 1336–1342, MAR 15 1991.

[159] V. Ruutu, V. Eltsov, A. Gill, T. Kibble, M. Krusius, Y. Makhlin, B. Placais, G. Volovik, and W. Xu, "Vortex formation in neutron-irradiated superfluid He-3 as an analogue of cosmological defect formation," *Nature*, vol. 382, pp. 334–336, JUL 25 1996.

[160] C. Bauerle, Y. Bunkov, S. Fisher, H. Godfrin, and G. Pickett, "Laboratory simulation of cosmic string formation in the early Universe using superfluid He-3," *Nature*, vol. 382, pp. 332–334, JUL 25 1996.

[161] L. E. Sadler, J. M. Higbie, S. R. Leslie, M. Vengalattore, and D. M. Stamper-Kurn, "Spontaneous symmetry breaking in a quenched ferromagnetic spinor Bose-Einstein condensate," *Nature*, vol. 443, pp. 312–315, SEP 21 2006.

[162] C. N. Weiler, T. W. Neely, D. R. Scherer, A. S. Bradley, M. J. Davis, and B. P. Anderson, "Spontaneous vortices in the formation of Bose-Einstein condensates," *Nature*, vol. 455, pp. 948–U37, OCT 16 2008.

[163] S. Ulm, J. Rossnagel, G. Jacob, C. Deguenther, S. T. Dawkins, U. G. Poschinger, R. Nigmatullin, A. Retzker, M. B. Plenio, F. Schmidt-Kaler, and K. Singer, "Observation of the Kibble-Zurek scaling law for defect formation in ion crystals," *Nature Communication*, vol. 4, AUG 2013.

[164] K. Pyka, J. Keller, H. L. Partner, R. Nigmatullin, T. Burgermeister, D. M. Meier, K. Kuhlmann, A. Retzker, M. B. Plenio, W. H. Zurek, A. del Campo, and T. E. Mehlstaeubler, "Topological defect formation and spontaneous symmetry breaking in ion Coulomb crystals," *Nature Communication*, vol. 4, AUG 2013.

[165] G. Lamporesi, S. Donadello, S. Serafini, F. Dalfovo, and G. Ferrari, "Spontaneous creation of Kibble-Zurek solitons in a Bose-Einstein condensate," *Nature Physics*, vol. 9, pp. 655–659, OCT 2013.

[166] N. Navon, A. L. Gaunt, R. P. Smith, and Z. Hadzibabic, "Critical dynamics of spontaneous symmetry breaking in a homogeneous Bose gas," *Science*, vol. 347, pp. 167–170, JAN 9 2015.

[167] J. Hove and A. Sudbø, "Anomalous scaling dimensions and stable charged fixed point of type-ii superconductors," *Phys. Rev. Lett.*, vol. 84, pp. 3426–3429, Apr 2000.

[168] D. M. Giaquinta, *Synthesis and Characterization of New Layered Main Group-Transition Metal Oxide*. Ph.D. Thesis, Massachusetts Institute of Technology, 1994.

[169] S. Abrahams, "Ferroelectricity and structure in the $YMnO_3$ family," *Acta Crystallographica Section B-Structural Science*, vol. 57, pp. 485–490, AUG 2001.

[170] C. R. Serrao, S. B. Krupanidhi, J. Bhattacharjee, U. V. Waghmare, A. K. Kundu, and C. N. R. Rao, "$InMnO_3$: A biferroic," *Journal of Applied Physics*, vol. 100, OCT 1 2006.

[171] B. Van Aken, T. Palstra, A. Filippetti, and N. Spaldin, "The origin of ferroelectricity in magnetoelectric $YMnO_3$," *Nature Materials*, vol. 3, pp. 164–170, MAR 2004.

[172] M.-A. Oak, J.-H. Lee, H. M. Jang, J. S. Goh, H. J. Choi, and J. F. Scott, "4d-5p orbital mixing and asymmetric in 4d - O 2p hybridization in $inmno_3$: A new bonding mechanism for hexagonal ferroelectricity," *Phys. Rev. Lett.*, vol. 106, p. 047601, Jan 2011.

[173] A. A. Belik, S. Kamba, M. Savinov, D. Nuzhnyy, M. Tachibana, E. Takayama-Muromachi, and V. Goian, "Magnetic and dielectric properties of hexagonal $inmno_3$," *Phys. Rev. B*, vol. 79, p. 054411, Feb 2009.

[174] Y. Kumagai, A. A. Belik, M. Lilienblum, N. Leo, M. Fiebig, and N. A. Spaldin, "Observation of persistent centrosymmetricity in the hexagonal manganite family," *Phys. Rev. B*, vol. 85, p. 174422, May 2012.

[175] F.-T. Huang, X. Wang, Y. S. Oh, K. Kurushima, S. Mori, Y. Horibe, and S.-W. Cheong, "Delicate balance between ferroelectricity and antiferroelectricity in hexagonal $inmno_3$," *Phys. Rev. B*, vol. 87, p. 184109, May 2013.

[176] M. Mekata, "Antiferro-ferrimagnatic transition in triangular ising lattice," *Journal of the Physical Society of Japan*, vol. 42, no. 1, pp. 76–82, 1977.

[177] F.-T. Huang, X. Wang, M. Griffin, Sinead Y. Kumagai, O. Gindele, M.-W. Chu, Y. Horibe, A. Spaldin, Nicola and S.-W. Cheong, "Duality of topological defects in hexagonal manganites," *Phys. Rev. Lett.*, vol. 113, p. 267602, Dec 2014.

[178] X. Wang, F.-T. Huang, R. Hu, F. Fan, and S.-W. Cheong, "Self-poling with oxygen off-stoichiometry in ferroelectric hexagonal manganites," *APL Materials*, vol. 3, no. 4, pp. –, 2015.

[179] X. Wang, M. Mostovoy, G. Han, M. Y. Horibe, T. Aoki, Y. Zhu, and S.-W. Cheong, "Unfolding of vortices into topological stripes in a multiferroic material," *Phys. Rev. Lett.*, vol. 112, p. 247601, Jun 2014.

[180] M. E. Dodd, P. C. Hendry, N. S. Lawson, P. V. E. McClintock, and C. D. H. Williams, "Nonappearance of vortices in fast mechanical expansions of liquid ^{4}He through the lambda transition," *Phys. Rev. Lett.*, vol. 81, pp. 3703–3706, Oct 1998.

[181] T. Yu, P. Gao, T. Wu, T. A. Tyson, and R. Lalancette, "Ferroelectricity in single crystal $InMnO_3$," *Applied Physics Letters*, vol. 102, APR 29 2013.

[182] P. Halasyamani and K. Poeppelmeier, "Noncentrosymmetric oxides," *Chemistry of Materials*, vol. 10, pp. 2753–2769, OCT 1998.